Doctoral Dissertation

博士論文

Neutrino oscillations deep inside core-collapse supernovae and their impact on νp-process nucleosynthesis

(重力崩壊型超新星の最深部で起こる
ニュートリノ振動とν p 元素合成過程への影響)

A Dissertation Submitted for the Degree of Doctor of Philosophy

December 2019

令和 元年 12 月 博士 (理学) 申請

Department of Astronomy, Graduate School of Science,

The University of Tokyo

東京大学大学院理学系研究科 天文学専攻

Hirokazu Sasaki

佐々木 宏和

Abstract

Large numbers of neutrinos are emitted in core-collapse supernova explosion. Supernova neutrinos are effective tools to understand phenomenology of supernova explosion and properties of neutrinos in extreme environment of core-collapse supernovae. Supernova neutrinos are first discovered in SN1987A, but the number of neutrino event is not enough for detection of neutrino oscillations inside core-collapse supernovae. It is considered that supernova neutrinos are affected by peculiar neutrino oscillations inside medium. Especially, coherent forward scatterings of neutrinos with themselves induce non-linear flavor conversions called "Collective neutrino oscillations" around $100 - 1000$ km from the center. Collective neutrino oscillations change neutrino and antineutrino spectra dramatically and increases high energy ν_e and $\bar{\nu}_e$ through the spectral swap. It is expected that such increased e-flavor neutrinos have influence on observable quantities such as neutrino signals in neutrino detectors and nuclear abundances of heavy nuclei in core-collapse supernovae. In this thesis, we carry out numerical simulation of collective neutrino oscillations in core-collapse supernovae. Then, we study how collective neutrino oscillations affect neutrino events in neutrino detectors and supernova nucleosynthesis.

First, we perform the three flavor multiangle simulations for precise collective neutrino oscillations by using simulation data of an electron capture supernova whose progenitor mass is $8.8M_{\odot}$. Collective neutrino oscillations are not prevented by the multiangle matter suppression because of the dilute envelop of the progenitor. In inverted mass hierarchy, $e - y$ conversions are dominant in collective neutrino oscillations as represented in previous studies. However, we find dominant $e - x$ conversions in normal mass hierarchy which are totally negligible in previous works. The $e - x$

conversions are sensitive to the baryon density outside the proto-neutron star. Therefore, such $e-x$ conversions would be characteristic behaviors of light mass progenitor such as electron capture supernovae. Furthermore, we discuss the detectability of collective neutrino oscillations in future neutrino detectors such as Hyper-Kamiokande (HK), JUNO and DUNE. We estimate spectra of ν_e and $\bar{\nu}_e$ on the earth. In inverted neutrino mass hierarchy, the spectrum of $\bar{\nu}_e$ on the earth becomes soft owing to the combination of collective neutrino oscillations and MSW H-resonances, so that the value of hardness ratio $R_{\rm H/L}$ is reduced. Such softening feature is suitable to reveal contributions of collective neutrino oscillations. HK can distinguish this effect within the 1σ Poisson error if the supernova occurs at 15 kpc from the earth. On the other hand, in normal mass hierarchy, the spectrum of ν_e becomes soft. DUNE can probe such softened ν_e spectrum within 4 kpc, but the significant reduction of hardness ratio around 100 ms can be detected even if the supernova occurs at the center of our galaxy ($\sim$ 10 kpc). The behavior of hardness ratio is opposite depending on neutrino mass hierarchies and neutrino species. Therefore, the combination of HK and DUNE is an intriguing opportunity to test the existence of collective neutrino oscillations.

In the second study, we simulate the effect of collective neutrino oscillations on the νp-process nucleosynthesis in proton rich neutrino driven winds. The number flux of energetic $\bar{\nu}_e$ is raised by collective neutrino oscillations in a 1D explosion model of a $40M_\odot$ progenitor. In the later wind trajectory at 1.1 s post bounce, abundances of p-nuclei are enhanced remarkably by $\sim 10-10^4$ times in normal mass hierarchy and p-nuclei are synthesized up to ^{124,126}Xe and ^{130}Ba. On the other hand, in the early wind model at 0.6 s, collective neutrino oscillations are prominent in inverted mass hierarchy irrespective of the reverse shock. Thus the νp-process nucleosynthesis is enhanced in inverted mass hierarchy. We simulate both cases with and without the reverse shock in the early wind model. Outside the reverse shock, the wind temperature becomes nearly constant in the temperature region for the νp-process ($T \sim 1.5-3.0\times10^9$K), which multiplies oscillation effects and results in more abundant p-nuclei. The averaged overproduction factor of p-nuclei is dominant in the later wind model if we remove the reverse shock in the early wind model. However, the contribution of the early wind model becomes large if we take into

account the reverse shock. Especially, the averaged overproduction factors of p-nuclei in the range of $A = 84 - 108$ are enhanced in inverted mass hierarchy owing to the reverse shock effect. Our result demonstrates that collective neutrino oscillations can strongly influence on the νp-process, which indicates that they should be included in nuclear network calculations in order to obtain precise abundances of p-nuclei. Our finding would help understand the origin of solar-system isotopic abundances of p-nuclei such as ^{92,94}Mo and ^{96,98}Ru.

Acknowledgments

I sincerely thank my supervisor Toshitaka Kajino for his kind and warm personality. I can continue my work for five years owing to his generous and patient encouragement. He gave me precious opportunity to collaborate with many researchers who help my research considerably. He also recommend me to talk in international conferences and study abroad together with his collaborators. Such experiences remove a barrier to foreigners and enrich my outlook not only on science but also on people and their communities. Thanks to his generous support, I was able to enjoy my Ph.D. course.

I appreciate Tomoya Takiwaki for precious collaboration. I can promote my study safely owing to fruitful discussions with him. I was able to obtain main results of this thesis thanks to his great cooperation. He kindly helped and advised me in many aspects.

I would like to thank many collaborators in my research: Pehlivan Yamac, Baha Balantekin, Takehito Hayakawa, Myung-Ki Cheoun, Motohiko Kusakabe, Ko Heamin, Shunsaku Horiuchi, Shio Kawagoe, Koji Ishidoshiro for useful discussions about the mechanism of collective neutrino oscillations, νp-process nucleosynthesis, the origin of p-nuclei, Nonstandard Interaction and the detection of neutrinos. Their constructive suggestions deepen my understanding and inspire me to proceed the next step.

I am grateful to members of Kajino group: Jun Hidaka, Tomoyuki Maruyama, Toshio Suzuki, Michael Famiano, Grant Mathews, Cemsinan Deliduman, Shota Shibagaki, Yutaka Hirai, Kanji Mori, Luo Yudong, Yuta Yamazaki and Stern Yao for scientific discussions and good relationship. I also thank all of the staffs of Division of Science in NAOJ for kind supports for five years.

Finally, I deeply thank my family and friends for helping me warmly and continuously.

Contents

Chapter 1

Introduction

In our universe, there are many sources of neutrinos such as solar neutrinos [1–5], atmospheric neutrinos [6–8], geoneutrinos [9, 10], supernova neutrino burst [11–13] and neutrinos from blazars [14]. From the observation of such neutrino fluxes, we can investigate fundamental properties of neutrinos such as neutrino oscillations [2–8, 15–20], an upper limit of neutrino mass [21] and bounds on magnetic moment of electron neutrino [22]. In addition, neutrinos interact with particles through weak interactions, so that neutrinos produced explosive astrophysical sites carry away information of deep inside the core where we can not explore by using optical observations. Therefore, neutrino astronomy plays important role for development of both particle physics and astrophysics.

Among many neutrino sources, supernova neutrino is one of the most attractive subjects. In the end of massive star ($M > 8M_{\odot}$), gravitational core-collapse occurs at the center. After the core bounce, the shock wave propagates outwards heating the falling material in outer region. The shock heating creates large amount of neutrinos at the center. Such produced neutrinos carry away about 99% of released gravitational energy of the inner core $\sim 10^{53}$ erg. Emitted neutrinos can be detected in neutrino observatories if a core-collapse supernova occurs near our galaxy. The frequency of core-collapse supernovae in a galaxy is 1-2 events per one century [24]. Historically, several supernovae are observed nearby our galaxy. The Club Nebula

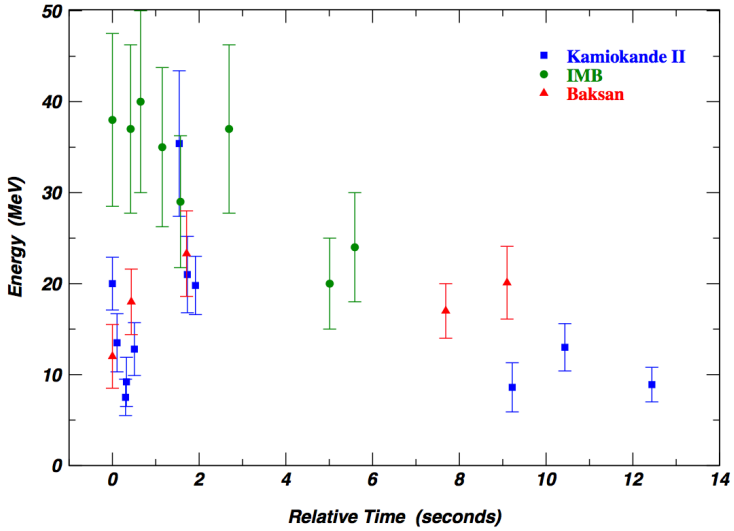

Figure 1.1: Neutrino signals of SN1987A observed in Kamiokande II, IMB and Baksan [23]. The vertical axis shows the energy of electron/positron produced inside the detector. The time in the horizontal axis is relative to the first event.

and Cassiopeia A (Cas A) are remnant of SN1054 and SN1604 in our galaxy, respectively. On 24 February 1987, a core-collapse supernova SN1987A was discovered in the Large Magellanic Cloud whose distance is ~ 50 kpc from the earth. The supernova neutrino was observed for the first time in Kamiokande II [11], IMB [12] and Baksan [13]. The detected events are shown in Fig.1.1. Kamiokande II and IMB are water Cherenkov detectors and Baksan is a liquid scintillator detector. The dominant process of neutrino detection is the inverse beta decay: $\bar{\nu}_e + p \to e^+ + n$ in both types of neutrino detectors even though about 10% of total event comes from neutrino-electron scatterings: $\nu + e^- \to \nu + e^-$ in water Cherenkov detector. Cherenkov lights radiated by charged particles are observed in water Cherenkov detector. In the liquid scintillator detector, free neutrons produced via inverse beta decay are captured by protons through $p + n \to d + \gamma$. The emitted photon becomes a scintillation signal. As shown in Fig.1.1, the neutrino emission continues during 10 s, which suggests the neutrino trapping deep inside the inner core. Furthermore, the averaged energy of neutrinos is estimated by ~ 10 MeV and the total neutrino luminosity is obtained by $\sim 10^{53}$ erg. Values of these quantities are consistent with theoretical prediction in delayed explosion mechanism [25, 26]. The neutrino detection in SN1987A opens

the era of neutrino astronomy but we need more neutrino events in order to study the detail of explosion mechanism and properties of neutrinos deep inside of the core. Currently, large volume neutrino detectors such as Super-Kamiokande (SK) [27, 28], KamLAND [29], Borexino [30], LVD [31], Daya bay [32] and IceCube [33] are ongoing. Larger neutrino event is expected in these current neutrino detectors for coming supernova explosion nearby our galaxy. For example, the total neutrino event in SK would be $\sim 10^4$ if core-collapse supernova occurs at the center of our galaxy (~ 10 kpc) [27]. The SuperNova Early Warning System (SNEWS) [34, 35] is a network of several neutrino observatories to alert the detection of supernova neutrino signal. Emergence of electromagnetic wave is delayed for a few hours or even days after the detection of neutrino signal because photons are easily trapped inside supernova material through electromagnetic interactions. Thus, an early warning of SNEWS can help subsequent optical observations. In addition, the next generation of neutrino detectors such as Hyper-Kamiokande (HK) [36], JUNO [37] and DUNE [38] will run within 10 years. Especially, DUNE is a liquid argon detectors which has sensitivity to ν_e through ${}^{40}\mathrm{Ar}(\nu_e, e^-){}^{40}\mathrm{K}^*$. These next generation neutrino detectors enable more abundant supernova neutrino detection and distinguish event numbers of different neutrino species.

Neutrino oscillations are macroscopic quantum phenomena caused by interference of two different quantum states proposed by Pontecorvo [39, 40] in analogy with $K^0 - \bar{K}^0$ oscillations. Neutrinos produced inside astrophysical sites are always affected by neutrino oscillations. Within the standard model, neutrinos and their antiparticle have three different quantum numbers called "flavors" such as $\{\nu_\alpha, \bar{\nu}_\alpha\}_{\alpha=e,\mu,\tau}$. Neutrino oscillation is the mixing of flavors during the propagation of neutrinos and antineutrinos. The number of detected neutrinos is affected by such quantum phenomenon. In our nature, neutrino oscillations are actually confirmed in atmospheric neutrinos [6–8] and solar neutrinos [1–5]. Then, values of neutrino mixing parameters which characterize neutrino oscillations are estimated in such observations. Neutrino experiments using reactors and accelerators can also determine or constrain neutrino mixing parameters which are not sensitive to flavor conversions in atmospheric and solar neutrinos [15–20]. Neutrino oscillations inside medium are different from that

in vacuum. Neutrino coherent forward scatterings with background particles change the dispersion relation in vacuum, which results in refractive effects in flavor space during the neutrino propagation. For example, neutrino coherent forward scatterings with background electrons give rise to the Mikheyev-Smirnov-Wolfenstein (MSW) resonances [41, 42], which solves missing ν_e flux in the sun ("Solar neutrino problem") [1, 5]. Among the refractive effects, coherent forward scatterings with neutrino themselves induce a non-linear potential in flavor space [43–55]. It is theoretically predicted that such non-linear potential appears in explosive astrophysical sites such as early universe, core-collapse supernovae, neutron star mergers and gamma ray bursts where large amount of neutrinos are produced.

It is considered that there are two types of neutrino oscillations inside core-collapse supernovae. The first one is the MSW matter effect caused by coherent forward scatterings of $\nu_e(\bar{\nu}_e) - e^-$ in outer layers ($\sim \mathcal{O}(1000)$ km) where the baryon density is $\sim 10^4 \mathrm{g/cm}^3$. Such matter effect induces a significant flavor mixing depending on neutrino mass hierarchy. The flavor conversions through MSW resonances also have influence on ν-process nucleosynthesis in outer layers, which produces several rare isotopes such as ^{7}Li, ^{11}B, ^{19}F, ^{98}Tc, ^{138}La and ^{180}Ta [56, 57]. The second flavor conversion is a non-linear flavor transition called "Collective neutrino oscillation" [58–84], which is caused by neutrino self interactions around $\mathcal{O}(100)$ km from the center before the MSW resonances. Collective neutrino oscillations induce remarkable spectral swaps [58,61] in both neutrino and antineutrino spectra. Such spectral swap increases amounts of energetic ν_e and $\bar{\nu}_e$, which would have significant influence on observational signal of neutrinos. In addition, collective neutrino oscillations occur inside neutrino driven winds where heavy nuclei beyond iron are actively produced through weak r-process in neutron rich outflows [85] and νp-process nucleosynthesis [86–88] in proton rich outflows. Neutrino spectra are crucial for such nucleosynthesis inside neutrino driven winds. The balance between spectra of ν_e and $\bar{\nu}_e$ determines the value of electron fraction inside neutrino driven winds. The free neutrons produced through $p(\bar{\nu}_e, e^+)n$ triggers off the νp-process nucleosynthesis. These things imply that collective neutrino oscillations have influence on nucleosynthesis inside neutrino driven winds, which would have impact on solar abundances of nuclei. Above rich

phenomena of collective neutrino oscillations are important for both neutrino physics and the still unknown origin of solar isotopic abundances.

In this thesis, we show numerical results of collective neutrino oscillations in core-collapse supernovae. Then, we discuss how collective neutrino oscillations can affect observable quantities such as event rates in neutrino detectors and abundances of nuclei inside core-collapse supernovae. Currently, there is no observational signal of non-linear flavor transitions caused by neutrino self interactions even though vacuum oscillations and MSW matter effects are confirmed in previous neutrino experiments, e.g. Refs. [5, 6]. Precise numerical simulation results are helpful to abstract the evidence of collective neutrino oscillations from observational data of a next core-collapse supernova nearby our galaxy.

The content of this thesis is as follows. Chapter 2 and 3 are review parts. The main parts of this thesis are Chapter 4 and 5. Finally, the conclusion of this thesis is shown in Chapter 6. In Chapter 2, we review how to calculate neutrino oscillations. We introduce Liuville-von Neumann equation for density matrices of neutrinos. This is an equation of motion of neutrino oscillations. Then, we derive vacuum Hamiltonian, MSW matter potential and non-linear potential of neutrino self interactions following a strategy of Refs. [45, 53]. In two flavor neutrinos (ν_e,ν_x), vacuum neutrino oscillations and MSW matter effects are explained in the language of density matrices. Here, general form of non-linear potential is obtained. In order to solve non-linear flavor conversions numerically, we need some model of neutrino emission reflecting geometry of astrophysical sites. In Chapter 3, the mechanism of core-collapse supernova is reviewed. Then, equation of motion of neutrino oscillations inside supernova is derived by employing the bulb model. We show numerical results of collective neutrino oscillations in two flavor neutrinos under the single angle approximation. This is a simple demonstration but we can see fundamental properties of collective neutrino oscillations which help understand behaviors of more complex non-linear phenomena in three flavor multiangle simulations used in next chapters. We show that the single spectral split of neutrino spectra is regarded as level crossing in a special frame called "co-rotating frame" as mentioned in Refs. [58, 62, 63]. In Chapter 4, we show

numerical results of three flavor multiangle simulations by using simulation data of an electron capture supernova. This is more sophisticated numerical treatment than two flavor single angle calculations in Chapter 3 because of the consideration of neutrino scattering angle and the realistic number of neutrino flavors. We discuss how collective neutrino oscillations can be distinguished in future neutrino detectors such as HK, JUNO and DUNE. The content of this chapter is shown in Ref. [84]. Originally, both supernova hydrodynamic simulations and post process three flavor multiangle simulations are carried out in Ref. [84], but, in this thesis, we mainly focus on my contribution, i.e. numerical simulation of neutrino oscillations and analysis of neutrino events in neutrino observatories. In Chapter 5, we show how collective neutrino oscillations can enhance the νp-process nucleosynthesis inside neutrino driven winds. We first review the basics of nucleosynthesis inside core-collapse supernovae and introduce the content of our previous work [82]. Furthermore, we also add the contribution of reverse shock which is not taken into account in Ref. [82]. In this thesis, we use the natural unit: $\hbar = c = k_{\rm B} = 1$.

Chapter 2

Neutrino oscillations

In this chapter, we derive equations of motion of neutrino oscillations in vacuum, electron background and neutrino background. Then, we review phenomelogy of vacuum neutrino oscillations and electron matter effect. Neutrino oscillation is governed by Liuville-von Neumann equation of a neutrino density matrix which is equivalent to Schrödinger equation in neutrino flavor space. Flavor eigenstates of neutrinos are not energy eigenstates in vacuum, so that vacuum Hamiltonian has non-diagonal components in flavor space. Such non-diagonal terms are origin of flavor transitions. Neutrino oscillations are sensitive to background medium. Neutrinos produced inside dense matter change their momentum through weak interactions with background particles. Outside such dense region, neutrino emission can be regarded as free streaming and only coherent forward scatterings become dominant. Coherent forward scatterings change a dispersion relation in the neutrino flavor space. Such refractive effect has influence on dynamics of flavor transitions. Charged current reactions between electron (anti)neutrinos with background electrons make a linear potential in neutrino Hamiltonian which is the origin of MSW resonances in flavor space. Such linear flavor transition has clue to interpret more complex non-linear oscillations caused by neutrino self interactions.

2.1 Liuville-von Neumann equation

Neutrino oscillations are quantum phenomena caused by interference among different neutrino spicies. Therefore, neutrino oscillations are described by quantum mechanical treatment. A time evolution of a quantum state is described by a Schrödinger equation:

$$i\frac{\mathrm{d}}{\mathrm{dt}}\left|\psi(t)\right\rangle = \hat{H}\left|\psi(t)\right\rangle, \tag{2.1}$$

where $|\psi(t)\rangle$ represents a quantum state vector at time t and $\hat{H}$ is Hamiltonian of the system. By using both Eq.(2.1) and its Hermite conjugate, we can easily derive the Liuville-von Neumann equation:

$$i\frac{\mathrm{d}}{\mathrm{dt}}\hat{\rho}(t) = [\hat{H}, \hat{\rho}(t)], \tag{2.2}$$

where $\hat{\rho}(t) = |\psi(t)\rangle\langle\psi(t)|$ and $[A, B] = AB - BA$. The density operator $\hat{\rho}(t)$ represents information of the quantum system. Here, the trace of the density operator is normalized by unity:

$$\mathrm{Tr}\hat{\rho}(t) = \sum_i \left\langle i\right|\hat{\rho}(t)\left|i\right\rangle = \sum_i \rho_{ii}(t) = 1. \tag{2.3}$$

The diagonal component $\rho_{ii}(t)$ shows a ratio of the quantum state i. In the context of neutrino oscillations, the diagonal terms of a density operator are interpreted as survival probability or number density of neutrinos. The non-diagonal component $\rho_{ij}(t) = \left\langle i\right|\hat{\rho}(t)\left|j\right\rangle$ $(i \neq j)$ represents the amplitude of quantum interference between i and j. Such non-diagonal components do not arise in the classical mechanics. Neutrino oscillations are maintained owing to finite value of the non-diagonal components. Flavor transitions do not suffer decoherence even in macroscopic time scale because weak interactions with background medium make only small disturbance in neutrino flavor space. In our derivation, the system is assumed to be a pure state, but Eq.(2.2) is also applied to a general mix state such as $\hat{\rho}(t) = \sum_i q_i \left|\psi_i(t)\right\rangle\left\langle\psi_i(t)\right|$. In some textbooks [89,90], neutrino oscillations in vacuum or in matter are explained by using Schrödinger equation (Eq.(2.1)). In below discussion, however, we try to study neutrino oscillations based on the Liuville-von Neumann equation (Eq.(2.2))

because we need to extend our discussion up to collective neutrino oscillations caused by neutrino self interactions. The Liuville-von Neumann equation is more convenient to simulate non-linear collective flavor transitions.

2.2 Theory of vacuum neutrino oscillations

Neutrinos are always produced through weak interactions so that there is no flavor transition if the flavor eigenstates $\{\nu_\alpha\}_{\alpha=e,\mu,\tau..}$ which are observed by experiments correspond to the mass eigenstates $\{\nu_i\}_{i=1,2,3..}$ which are energy eigenstates in vacuum. The vacuum Hamiltonian of neutrinos is diagonalized by the mass eigenstate whose energy is E_i:

$$\hat{H}_0 = \int \frac{\mathrm{d^3p}}{(2\pi)^3}\ E_i\ \hat{a}_i^\dagger(p)\hat{a}_i(p), \tag{2.4}$$

$$E_i = \sqrt{p^2 + m_i^2} \tag{2.5}$$

where p is the momentum and m_i is the mass of ν_i. Here, we introduce annihilation and creation operators of ν_i which satisfy below anticommutation relation:

$$\{\hat{a}_i(q), \hat{a}_j^\dagger(p)\} = (2\pi)^3\delta^3(p-q)\delta_{ij}, \tag{2.6}$$

where $\{A, B\} = AB + BA$. Here, the degree of freedom in neutrino spin is not taken into account in both $\hat{a}$ and $\hat{a}^\dagger$. In the relativistic limit ($p >> m_i$), wrong helicity (anti)neutrinos are highly suppressed by $O(m_i/E_i)$ [53]. Therefore, we can assume that neutrino (antineutrino) has one negative (positive) helicity and the spin structure can be ignored. Supernova neutrinos are regarded as relativistic particles because energy scale of supernova neutrino (∼MeV) is much larger than the total neutrino mass constrained in the cosmic microwave background (CMB) radiation: $\sum m_\nu \leq 0.17$ eV [91]. In the relativistic neutrinos, energy eigenvale in Eq.(2.5) is decomposed by

$$E_i \sim p + \frac{m_i^2}{2p}, \tag{2.7}$$

then, the Hamiltonian is also divided by two parts:

$$\hat{H}_0 = \hat{H}_{\rm kin} + \hat{\Omega}, \tag{2.8}$$

$$\hat{H}_{\rm kin} = \int \frac{{\rm d}^3{\rm p}}{(2\pi)^3}\ p\ \hat{a}_i^\dagger(p)\hat{a}_i(p), \tag{2.9}$$

$$\hat{\Omega} = \int \frac{{\rm d}^3{\rm p}}{(2\pi)^3}\ \frac{m_i^2}{2p}\hat{a}_i^\dagger(p)\hat{a}_i(p). \tag{2.10}$$

The neutrino kinetic term (Eq.(2.9)) which is proportional to identity in mass and flavor bases does not have any influence on neutrino oscillations. Therefore, we ignore Eq.(2.9) and focus on Eq.(2.10). In order to discuss neutrino oscillations, we introduce an unitary transformation U which connects operators of mass eigenstates $\{\nu_i\}_{i=1,2,3..}$ with that of flavor eigenstates $\{\nu_\alpha\}_{\alpha=e,\mu,\tau..}$:

$$\hat{a}_i = U^*_{\alpha i}\hat{a}_\alpha, \tag{2.11}$$

$$\hat{a}_i^\dagger = U_{\alpha i}\hat{a}_\alpha^\dagger, \tag{2.12}$$

where anticommutation relation in Eq.(2.6) is also held in flavor eigenstates:

$$\{\hat{a}_\alpha(q), \hat{a}_\beta^\dagger(p)\} = (2\pi)^3\delta^3(p-q)\delta_{\alpha\beta}. \tag{2.13}$$

By using Eqs.(2.11) and (2.12), the vacuum Hamiltonian is described by flavor eigenstates [45, 48, 51, 53]:

$$\hat{\Omega} = \int \frac{{\rm d}^3{\rm p}}{(2\pi)^3}\ \hat{a}_\alpha^\dagger(p)\Omega_{\alpha\beta}(p)\hat{a}_\beta(p), \tag{2.14}$$

$$\Omega_{\alpha\beta}(p) = U_{\alpha i}\frac{m_i^2}{2p}U^*_{\beta i}, \tag{2.15}$$

where the non-diagonal component $\Omega_{\alpha\beta}(p)(\alpha \neq \beta)$ is the origin of neutrino oscillations between ν_α and ν_β. Here, we introduce an one-body neutrino density matrix $\rho_{\alpha\beta}(t,p)$ [45, 53] which is defined by an ensemble average of a neutrino number operator:

$$\langle\hat{a}_\beta^\dagger(q)\hat{a}_\alpha(p)\rangle = {\rm Tr}[\hat{a}_\beta^\dagger(q)\hat{a}_\alpha(p)\hat{\rho}(t)] = (2\pi)^3\delta^3(p-q)\rho_{\alpha\beta}(t,p), \tag{2.16}$$

$$n_{\nu_\alpha}(t) = \int \frac{{\rm d}^3{\rm p}}{(2\pi)^3}\ \rho_{\alpha\alpha}(t,p), \tag{2.17}$$

where $n_{\nu_\alpha}(t)$ [cm^{-3}] is the number density of ν_α at time t. The time evolution of the ensemble average of the number operator is calculated by using Eqs.(2.2), (2.14) and (2.16):

$$\begin{aligned} i\frac{\mathrm{d}}{\mathrm{dt}}\langle\hat{a}^\dagger_\beta(q)\hat{a}_\alpha(p)\rangle &= \mathrm{Tr}\{\hat{a}^\dagger_\beta(q)\hat{a}_\alpha(p)[\hat{\Omega},\hat{\rho}(t)]\} \\ &= \mathrm{Tr}\{\hat{a}^\dagger_\beta(q)\hat{a}_\alpha(p)\hat{\Omega}\hat{\rho}(t)\} - \mathrm{Tr}\{\hat{a}^\dagger_\beta(q)\hat{a}_\alpha(p)\hat{\rho}(t)\hat{\Omega}\} \\ &= \mathrm{Tr}\{\hat{a}^\dagger_\beta(q)\hat{a}_\alpha(p)\hat{\Omega}\hat{\rho}(t)\} - \mathrm{Tr}\{\hat{\Omega}\hat{a}^\dagger_\beta(q)\hat{a}_\alpha(p)\hat{\rho}(t)\} \\ &= \langle[\hat{a}^\dagger_\beta(q)\hat{a}_\alpha(p),\hat{\Omega}]\rangle \\ &= \Omega_{\alpha k}(p)\langle\hat{a}^\dagger_\beta(q)\hat{a}_k(p)\rangle - \langle\hat{a}^\dagger_k(q)\hat{a}_\alpha(p)\rangle\Omega_{k\beta}(q). \end{aligned} \tag{2.18}$$

Then, Liuville-von Neumann equation of the one-body neutrino density matrix is derived:

$$i\frac{\mathrm{d}}{\mathrm{dt}}\rho_{\alpha\beta}(t,p) = [\Omega(p),\rho(t,p)]_{\alpha\beta}. \tag{2.19}$$

We solve Eq.(2.19) to study vacuum neutrino oscillations. The diagonal component $\rho_{\alpha\alpha}(t,p)$ shows the number of ν_α whose momentum is p at time t. The non-diagonal component $\rho_{\alpha\beta}(t,p)$ ($\alpha \neq \beta$) represents strength of quantum interference between ν_α and ν_β. All of neutrinos are produced in weak interactions, so that initial neutrino density matrix is always diagonal in flavor basis: $\rho_{\alpha\beta}(t=0,p) \propto \delta_{\alpha\beta}$. Furthermore, two diagonal matrices A and B commute with each other: $[A,B]=0$. Therefore, the right hand side of Eq.(2.19) becomes zero and any flavor transitions would not appear if the vacuum Hamiltonian was always diagonal in flavor basis.

Finally, let's discuss the difference between Dirac and Majorana neutrinos. The N flavor unitary transformation of Eqs.(2.11) and (2.12) is composed of two unitary matrices [90]:

$$U = U^D D^M, \tag{2.20}$$

$$D^M = \mathrm{diag}\left(1, e^{i\lambda_2}, ..., e^{i\lambda_N}\right), \tag{2.21}$$

where U^D includes $\frac{(N-1)(N-2)}{2}$ dirac phases and $\frac{N(N-1)}{2}$ mixing angles. The difference between Dirac and Majorana neutrinos is existence of Majorana phases $\{\lambda_i\}_{i=2...N}$.

However, such Majorana phases are canceled in Eq.(2.15). Therefore we can not distinguish Dirac and Majorana neutrinos from vacuum neutrino oscillations.

2.3 Two flavor neutrino oscillations in vacuum

We show the behavior of vacuum neutrino oscillations in two flavor neutrinos. The unitary matrix U_2 between flavor basis (ν_e, ν_x) and mass basis (ν_1, ν_2) is characterized by a mixing angle θ:

$$\begin{pmatrix} \nu_e \\ \nu_x \end{pmatrix} = U_2 \begin{pmatrix} \nu_1 \\ \nu_2 \end{pmatrix}, \tag{2.22}$$

$$U_2 = \begin{pmatrix} \cos\theta & \sin\theta \\ -\sin\theta & \cos\theta \end{pmatrix}. \tag{2.23}$$

The vacuum Hamiltonian Eq.(2.15) in two flavor neutrinos is described by

$$\Omega(E) = \frac{m_1^2 + m_2^2}{4E} \begin{pmatrix} 1 & 0 \\ 0 & 1 \end{pmatrix} + \frac{\Delta m^2}{4E} \begin{pmatrix} -\cos 2\theta & \sin 2\theta \\ \sin 2\theta & \cos 2\theta \end{pmatrix} \tag{2.24}$$

where $\Delta m^2 = m_2^2 - m_1^2$ is the mass difference and $E = |p|$ is the neutrino energy. The first term of the right hand side in Eq.(2.24) is diagonal matrix in flavor basis, so that we can ignore this term in neutrino oscillations. We set only electron type neutrino at initial time:

$$\rho(0, E) = \begin{pmatrix} 1 & 0 \\ 0 & 0 \end{pmatrix}, \tag{2.25}$$

where the number of neutrinos are normalized by unity. Then, the equation of motion of the neutrino density matrix in Eq.(2.19) can be solved analytically like below:

$$\rho(t, E) = e^{-i\Omega(E)t}\ \rho(0, E)\ e^{i\Omega(E)t}, \tag{2.26}$$

where

$$e^{i\Omega(E)t} = \cos\frac{\Delta m^2}{4E}t \begin{pmatrix} 1 & 0 \\ 0 & 1 \end{pmatrix} + i \sin\frac{\Delta m^2}{4E}t \begin{pmatrix} -\cos 2\theta & \sin 2\theta \\ \sin 2\theta & \cos 2\theta \end{pmatrix}. \tag{2.27}$$

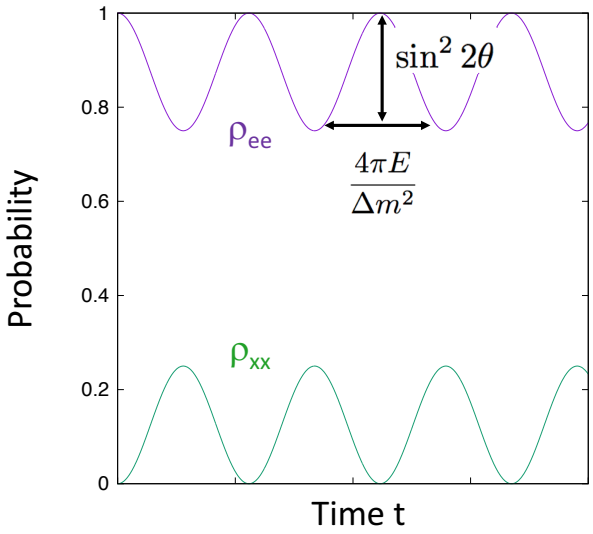

Figure 2.1: Schematic picture of two flavor vacuum neutrino oscillations. We show the survival probability (Eq.(2.28)) and the transition probability (Eq.(2.29)) of an electron type neutrino.

From Eqs. (2.25), (2.26) and (2.27), the diagonal components are derived:

$$\rho_{ee}(t,E) = 1 - \sin^2 2\theta \sin^2 \frac{\Delta m^2}{4E} t, \tag{2.28}$$

$$\rho_{xx}(t,E) = \sin^2 2\theta \sin^2 \frac{\Delta m^2}{4E} t, \tag{2.29}$$

where Eq.(2.28) represents the survival probability of $\nu_e \to \nu_e$ and Eq.(2.29) corresponds to the transition probability of $\nu_e \to \nu_x$. Behaviors of such diagonal components are shown in Fig.2.1. A finite mixing angle θ and a finite neutrino mass difference Δm^2 induce neutrino oscillations, which is equivalent to the existence of finite non-diagonal terms in $\Omega(E)$. We can consider flavor transitions of emitting neutrinos if we impose a traveling distance $L = ct$ ($c = 1$, Light velocity). The amplitude of flavor transition is determined by $\sin^2 2\theta$. Furthermore, neutrino mass difference

Table 2.1: Typical values of neutrino energy, the distance from the source and the sensitive neutrino mass difference [92].

Source	E [MeV]	L [km]	Sensitive Δm^2 [eV^2]
Short baseline Reactor	~ 1	~ 1	$\sim 10^{-3}$
Long baseline Reactor	~ 1	$\sim 10^2$	$\sim 10^{-5}$
Accelerator	$\sim 10^3$	$\sim 10^3$	$\sim 10^{-3}$
Atmospheric	$\sim 10^3$	$\sim 10^4$	$\sim 10^{-4}$
Solar	~ 1	$\sim 10^8$	$\sim 10^{-11}$

characterizes a periodic oscillation length l_{osc}:

$$l_{osc} = \frac{4\pi E}{\Delta m^2} = 2.47 \frac{E[\mathrm{GeV}]}{\Delta m^2[\mathrm{eV}^2]} \text{ km}. \tag{2.30}$$

Flavor transitions are not measured if the observer is close to the neutrino source: $L << l_{osc}$. On the other hand, neutrino oscillation have washed out and Eqs.(2.28),(2.29) are time averaged if the traveling distance is much larger than the oscillation length: $L >> l_{osc}$. Therefore, the value of Δm^2 can be probed only if $L \sim l_{osc}$. Table.2.1 summarizes the sensitivity of Δm^2 in various neutrino sources.

2.4 Neutrino mixing parameters in active three flavor neutrinos

Three active neutrinos $(\nu_e, \nu_\mu, \nu_\tau)$ and corresponding antineutrinos $(\bar{\nu}_e, \bar{\nu}_\mu, \bar{\nu}_\tau)$ are confirmed in our nature. The three flavor unitray matrix U_3 is called "Pontecorvo-Maki-Nakagawa-Sakata (PMNS) matrix" [93]:

$$U_3 = \begin{pmatrix} 1 & 0 & 0 \\ 0 & \cos\theta_{23} & \sin\theta_{23} \\ 0 & -\sin\theta_{23} & \cos\theta_{23} \end{pmatrix} \begin{pmatrix} \cos\theta_{13} & 0 & \sin\theta_{13} e^{-i\delta_{CP}} \\ 0 & 1 & 0 \\ -\sin\theta_{13} e^{i\delta_{CP}} & 0 & \cos\theta_{13} \end{pmatrix} \begin{pmatrix} \cos\theta_{12} & \sin\theta_{12} & 0 \\ -\sin\theta_{12} & \cos\theta_{12} & 0 \\ 0 & 0 & 1 \end{pmatrix} \tag{2.31}$$

where θ_{12}, θ_{13} and θ_{23} are mixing angles and δ_{CP} is the CP phase. As discussed in previous two flavor case, the finite values of mixing angles are necessary to induce flavor transitions. By using Eqs.(2.15) and (2.31), the vacuum Hamiltonian of three

Table 2.2: Values of neutrino mixing parameters in the present day [92].

Neutrino mixing parameters	
$\sin^2\theta_{12}$	0.307 ± 0.013
Δm^2_{21}	$(7.53 \pm 0.18) \times 10^{-5}$ eV^2
$\sin^2\theta_{23}$	$0.536^{+0.023}_{-0.028}$ (Inverted) $0.512^{+0.019}_{-0.022}$ (Normal, $\theta_{23} < \pi/4$) $0.542^{+0.019}_{-0.022}$ (Normal, $\theta_{23} > \pi/4$)
Δm^2_{32}	$(-2.55 \pm 0.04) \times 10^{-3}$ eV^2 (Inverted) $(2.444 \pm 0.034) \times 10^{-3}$ eV^2 (Normal)
$\sin^2\theta_{13}$	$(2.18 \pm 0.07) \times 10^{-2}$
δ_{CP}	$1.37^{+0.18}_{-0.16}\pi$ rad

flavor neutrinos is obtained

$$\Omega(E) = \frac{\sum_{i=1}^{3} m_i^2}{6E} \begin{pmatrix} 1 & 0 & 0 \\ 0 & 1 & 0 \\ 0 & 0 & 1 \end{pmatrix} + \frac{\Delta m^2_{21}}{6E} U_3 \begin{pmatrix} -2 & 0 & 0 \\ 0 & 1 & 0 \\ 0 & 0 & 1 \end{pmatrix} U_3^\dagger + \frac{\Delta m^2_{32}}{6E} U_3 \begin{pmatrix} -1 & 0 & 0 \\ 0 & -1 & 0 \\ 0 & 0 & 2 \end{pmatrix} U_3^\dagger, \tag{2.32}$$

where $\Delta m^2_{21} = m_2^2 - m_1^2$ and $\Delta m^2_{32} = m_3^2 - m_2^2$. The first term of the right hand side in Eq.(2.32) does not contribute to neutrino oscillations. Historically, neutrino mixing angles θ_{ij}, neutrino mass differences Δm^2_{ij} and CP phase δ_{CP} were estimated by various neutrino experiments and observations such as solar neutrino [2–5], atmospheric neutrino [6–8], accelerator neutrino experiments [18–20] and reactor neutrino experiments [15–17]. Table 2.2 represents up-to-date values of these neutrino mixing parameters.

Currently, the sign of $\Delta m^2_{32} = m_3^2 - m_2^2$ is still unknown. The positive (negative) sign case is called normal (inverted) mass hierarchy, respectively. Neutrino oscillations inside electron or neutrino backgrounds are highly sensitive to the neutrino mass hierarchy because the sign of vacuum Hamiltonian determines the condition of level

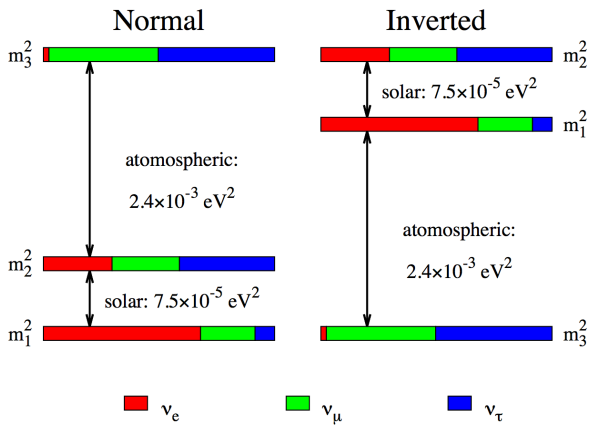

Figure 2.2: Two different orders of neutrino mass [37]. The positive (negative) $\Delta m^2_{32} = m^2_3 - m^2_2$ represents normal (inverted) mass hierarchy, respectively.

crossings in flavor transitions. Even though the inverted mass hierarchy is disfavored at the 93% C.L. [20], more robust conclusion should be drawn in future long base line experiments such as NoνA, T2K and reactor experiments at JUNO [37], RENO50 [94] and atmospheric neutrino experiments in Hyper-Kamoikande [36], INO [95], ORCA [96] and PINGU [97].

2.5 The derivation of MSW matter potential

Neutrino oscillations are sensitive to coherent forward scattering with back ground particles because such forward scattering induces flavor dependent refractive potential in the neutrino Hamiltonian [42]. This is an analogy with the refractive effect on the electromagnetic waves inside medium. Neutrino scatterings are divided by neutral and charged current reactions depending on the exchanging weak bosons ($W^{\pm}, Z^0$) through the interactions. Neutral current scatterings with background nucleons and electrons produce the same refractive potentials in all flavors of neutrinos. Such refractive effect does not contribute to neutrino oscillations. In the energy scale of supernova neutrinos ($\sim$ 10 MeV), charged current reactions with background medium only occur in electron type neutrinos because the neutrino energy is smaller than the mass of $\mu^{\pm}$(106 MeV) and that of $\tau^{\pm}$(1.78 GeV). Especially, charged current reactions

of e-flavor neutrino scatterings with background electrons:

$$\nu_e + e^{\pm} \to e^{\pm} + \nu_e, \tag{2.33}$$

$$\bar{\nu}_e + e^{\pm} \to e^{\pm} + \bar{\nu}_e, \tag{2.34}$$

produce a flavor dependent refractive potential which induces the Mikheyev-Smirnov-Wolfenstein (MSW) resonance [41, 42]. In this section, we focus on the derivation of such MSW matter potential. The momentum transfer of $W^{\pm}$ bosons is almost ignored if neutrino energy is much smaller than the mass of $W^{\pm}$ boson ($\sim$ 80 GeV). Then, the effective Hamiltonian of Eqs.(2.33) and (2.34) become a 4-Fermi interaction:

$$\hat{H}_{CC} = \frac{G_F}{\sqrt{2}} \int \mathrm{d}^3x \ \bar{\nu}_e(x)\gamma^{\mu}(1-\gamma_5)e(x) \ \bar{e}(x)\gamma_{\mu}(1-\gamma_5)\nu_e(x), \tag{2.35}$$

where G_F is the Fermi's coupling constant. Eq.(2.35) includes above four different weak interactions. Among them, first, we pick up the electron neutrino scattering with an background electron: $\nu_e + e^- \to e^- + \nu_e$ which is described by the second quantized Hamiltonian below:

$$\hat{V}_{\nu e} = \int \frac{\mathrm{d}^3\mathrm{p}}{(2\pi)^3}\frac{\mathrm{d}^3\mathrm{q}}{(2\pi)^3}\frac{\mathrm{d}^3\mathrm{p}'}{(2\pi)^3}\frac{\mathrm{d}^3\mathrm{q}'}{(2\pi)^3} \ V_{\nu e}(p,q;p',q')_{\beta_1;\alpha_1}\hat{a}^{\dagger}_{\beta_1}(p)\hat{c}^{\dagger}(q)\hat{c}(q')\hat{a}_{\alpha_1}(p'), \tag{2.36}$$

where $\hat{c}$ and $\hat{c}^{\dagger}$ are annihilation and creation operators of electrons. The coefficient $V_{\nu e}(p,q;p',q')_{\beta_1;\alpha_1}$ is derived by the Fourier expansion of Eq.(2.35) in momentum space. We set the Hilbert space of the neutrino many-body system: $\mathcal{H}_S$ and that of the environment: $\mathcal{H}_B$. The Liuville-von Neumann equation (Eq.(2.2)) represents the time evolution of the density operator in the total Hilbert space: $\mathcal{H} = \mathcal{H}_S \otimes \mathcal{H}_B$. In general, the density operator of open quantum system S is obtained by a trace over the environment B:

$$\hat{\rho}_S = \mathrm{Tr}_{\mathrm{B}}[\hat{\rho}]. \tag{2.37}$$

$\hat{\rho}_S$ is called a "reduced density matrix". Then, the time evolution of $\hat{\rho}_S$ is derived from Eqs.(2.2), (2.36) and (2.37):

$$i\frac{\mathrm{d}}{\mathrm{dt}}\hat{\rho}_S = [\hat{\Omega}, \hat{\rho}_S] + \mathrm{Tr}_{\mathrm{B}}[\hat{\mathrm{V}}_{\nu\mathrm{e}}, \hat{\rho}], \tag{2.38}$$

where $\hat{\Omega}$ represents the vacuum Hamiltonian in Eq.(2.14). If the interaction between S and B is weak, the density operator becomes the product of reduced density operators in each system:

$$\hat{\rho} \sim \hat{\rho}_S \otimes \hat{\rho}_B. \tag{2.39}$$

This is known as the Born approximation [98] which ignores an entanglement between S and B. Therefore, the second term of the right hand side in Eq.(2.38) induces effective one-body Hamiltonian:

$$\mathrm{Tr_B}[\hat{\mathrm{V}}_{\nu\mathrm{e}}, \hat{\rho}] = [\hat{\tilde{\mathrm{V}}}_{\nu\mathrm{e}}, \hat{\rho}_{\mathrm{S}}], \tag{2.40}$$

$$\hat{\tilde{V}}_{\nu e} = \mathrm{Tr_B}\{\hat{\rho}_{\mathrm{B}}\hat{\mathrm{V}}_{\nu\mathrm{e}}\}. \tag{2.41}$$

Here, we introduce ensemble average of background electrons:

$$\langle \hat{c}^\dagger(q)\hat{c}(q')\rangle = \mathrm{Tr}[\hat{c}^\dagger(q)\hat{c}(q')\hat{\rho}_B] = (2\pi)^3\delta^3(q-q')f_{e^-}(q), \tag{2.42}$$

$$n_{e^-} = \int \frac{\mathrm{d^3q}}{(2\pi)^3} f_{e^-}(q), \tag{2.43}$$

where n_{e^-} [cm^{-3}] is the number density of background electron. Then, we can obtain more concrete formula of Eq.(2.41):

$$\begin{aligned}
\hat{\tilde{V}}_{\nu e} &= \int \frac{\mathrm{d^3p}}{(2\pi)^3}\frac{\mathrm{d^3q}}{(2\pi)^3}\frac{\mathrm{d^3p'}}{(2\pi)^3}\frac{\mathrm{d^3q'}}{(2\pi)^3}\ V_{\nu e}(p,q;p',q')_{\beta_1;\alpha_1}\hat{a}^\dagger_{\beta_1}(p)\langle\hat{c}^\dagger(q)\hat{c}(q')\rangle\hat{a}_{\alpha_1}(p') \\
&= \int \frac{\mathrm{d^3p}}{(2\pi)^3}\int \frac{\mathrm{d^3q}}{(2\pi)^3}\int \frac{\mathrm{d^3p'}}{(2\pi)^3} V_{\nu e}(p,q;p',q)_{\beta_1;\alpha_1} f_{e^-}(q)\ \hat{a}^\dagger_{\beta_1}(p)\hat{a}_{\alpha_1}(p') \\
&= \sqrt{2}G_F n_{e^-}\ \delta_{e\beta_1}\delta_{e\alpha_1}\int \frac{\mathrm{d^3p}}{(2\pi)^3}\hat{a}^\dagger_{\beta_1}(p)\hat{a}_{\alpha_1}(p),
\end{aligned} \tag{2.44}$$

where unpolarized background electrons are assumed. The coefficient $V_{\nu e}(p,q;p',q)_{\beta_1;\alpha_1} \propto \delta^3(p-p')\delta_{e\beta_1}\delta_{e\alpha_1}$ in the second line of Eq.(2.44) represents the amplitude of forward elastic scattering. The Kronecker delta $\delta_{e\beta_1}\delta_{e\alpha_1}$ reflects the flavor dependence in the charged current reaction in electron sector. The contribution from $\nu_e + e^+ \to e^+ + \nu_e$ is easily added to Eq.(2.44) by replacing electron number density n_{e^-} to net electron number density $n_e = n_{e^-} - n_{e^+}$ where the negative sign $-n_{e^+}$ comes from an

anticommutation of positron operators in the Hamiltonian. Then, the time evolution of neutrino one-body density matrix inside electron background is derived from Eqs.(2.38) and (2.44) in the same way as Eq.(2.19):

$$i\frac{\mathrm{d}}{\mathrm{dt}}\rho(t,p) = [\Omega(p) + V_{\mathrm{MSW}}, \rho(t,p)], \tag{2.45}$$

$$V_{\mathrm{MSW}} = \sqrt{2}G_F n_e \begin{pmatrix} 1 & 0 & 0 & .. \\ 0 & 0 & 0 & .. \\ 0 & 0 & 0 & .. \end{pmatrix}, \tag{2.46}$$

where V_{MSW} is the MSW matter potential in flavor space which triggers MSW resonances. Refractive potentials created by neutral current scatterings with background electrons, nucleons and nuclei ($\nu_\alpha + f \to \nu_\alpha + f$) are removed from neutrino flavor space because the matrix of effective Hamiltonian is always diagonal. We remark that (anti) neutrino scattering with themselves are only exception in neutral current reactions. Neutrino self interactions make a non-linear potential in neutrino flavor space as discussed in §2.8.

2.6 The Equation of motion of antineutrino oscillations

Let's introduce the annihilation and creation operators of antineutrinos which satisfy an anticommutation relation like below:

$$\{\hat{b}_\alpha(q), \hat{b}^\dagger_\beta(p)\} = (2\pi)^3\delta^3(p-q)\delta_{\alpha\beta}. \tag{2.47}$$

The flavor eigenstate and mass eigenstate of neutrinos are connected with unitary matrix U defined in Eqs.(2.11) and (2.12). On the other hand, flavor basis of antineutrinos are connected with their mass basis through U^*. Then, the vacuum Hamiltonian of antineutrinos is described by

$$\hat{\bar{\Omega}} = \int \frac{\mathrm{d}^3\mathrm{p}}{(2\pi)^3}\ \hat{b}^\dagger_\beta(p)\Omega^*_{\beta\alpha}(p)\hat{b}_\alpha(p) = \int \frac{\mathrm{d}^3\mathrm{p}}{(2\pi)^3}\ \hat{b}^\dagger_\beta(p)\Omega_{\alpha\beta}(p)\hat{b}_\alpha(p), \tag{2.48}$$

where $\Omega_{\alpha\beta}$ is given by Eq.(2.15). The effective one-body operator of Eq.(2.34) is obtained by the same calculation as Eq.(2.44):

$$\hat{\bar{V}}_{\rm MSW} = -\int \frac{{\rm d}^3{\rm p}}{(2\pi)^3}\hat{b}^\dagger_\beta(p)(V_{\rm MSW})_{\alpha\beta}\hat{b}_\alpha(p), \tag{2.49}$$

$$(V_{\rm MSW})_{\alpha\beta} = \sqrt{2}G_F n_e\ \delta_{e\beta}\delta_{e\alpha}, \tag{2.50}$$

where the negative sign reflects a replacement: $n_{e^-} - n_{e^+} \longmapsto n_{e^+} - n_{e^-}$. The antineutrino density operator $\hat{\bar{\rho}}_S$ follows the similar equation of motion as Eq.(2.38):

$$i\frac{\rm d}{{\rm dt}}\hat{\bar{\rho}}_S = [\hat{\bar{\Omega}}, \hat{\bar{\rho}}_S] + [\hat{\bar{V}}_{\rm MSW}, \hat{\bar{\rho}}_S]. \tag{2.51}$$

We introduce the one-body density matrix of antineutrino [45]:

$$\langle\hat{b}^\dagger_\beta(q)\hat{b}_\alpha(p)\rangle = {\rm Tr}[\hat{b}^\dagger_\beta(q)\hat{b}_\alpha(p)\hat{\rho}(t)] = (2\pi)^3\delta^3(p-q)\bar{\rho}_{\beta\alpha}(t,p), \tag{2.52}$$

$$n_{\bar{\nu}_\alpha}(t) = \int \frac{{\rm d}^3{\rm p}}{(2\pi)^3}\ \bar{\rho}_{\alpha\alpha}(t,p), \tag{2.53}$$

where $n_{\bar{\nu}_\alpha}(t)$ [cm^{-3}] is the number density of $\bar{\nu}_\alpha$. The order of flavor indices in Eq.(2.52) is reversed compared with that in Eq.(2.16). This treatment enables the same arbitrary unitary transformation in both neutrino and antineutrino sectors. The time evolution of the ensemble average of a density operator is calculated like below:

$$\begin{aligned} i\frac{\rm d}{{\rm dt}}\langle\hat{b}^\dagger_\beta(q)\hat{b}_\alpha(p)\rangle &= {\rm Tr}\{\hat{b}^\dagger_\beta(q)\hat{b}_\alpha(p)[\hat{\bar{\Omega}}, \hat{\bar{\rho}}_S] + [\hat{\bar{V}}_{\rm MSW}, \hat{\bar{\rho}}_S]\} \\ &= \langle\hat{b}^\dagger_\beta(q)\hat{b}_k(p)\rangle(\Omega(p) - V_{\rm MSW})_{k\alpha} - (\Omega(p) - V_{\rm MSW})_{\beta k}(q)\langle\hat{b}^\dagger_k(q)\hat{b}_\alpha(p)\rangle. \end{aligned} \tag{2.54}$$

From Eqs.(2.52) and (2.54), the time evolution of one-body density matrix of antineutrino is derived by

$$i\frac{\rm d}{{\rm dt}}\bar{\rho}(t,p) = [-\Omega(p) + V_{\rm MSW}, \bar{\rho}(t,p)]. \tag{2.55}$$

Let's compare time evolution of antineutrino in Eq.(2.55) with that of neutrino in Eq.(2.45). In antineutrino flavor transitions, the negative sign appears in front of the vacuum term without changing the matter potential. Such sign difference is crucial for the MSW resonance because the resonance condition is sensitive to the relative sign between $\Omega(p)$ and $V_{\rm MSW}$.

In above discussion, we only show the time evolution of antineutrinos considering the effective Hamiltonian of Eq.(2.35). However, our discussion can be extended to other effective one-body Hamiltonian $\hat{V}_{\rm eff}$ which is described by

$$\hat{V}_{\rm eff} = \int \frac{{\rm d}^3{\rm p}}{(2\pi)^3} \left\{ \hat{a}^\dagger_\beta(p) V_{\rm eff}(t,p)_{\beta\alpha} \hat{a}_\alpha(p) - \hat{b}^\dagger_\beta(p) V_{\rm eff}(t,p)_{\alpha\beta} \hat{b}_\alpha(p) \right\}. \tag{2.56}$$

In this general case, the time evolutions of (anti) neutrino density matrices are easily obtained by replacing $V_{\rm MSW}$ with $V_{\rm eff}(t,p)$ in Eqs.(2.45) and (2.55):

$$i\frac{\rm d}{{\rm dt}}\rho(t,p) = [\Omega(p) + V_{\rm eff}(t,p), \rho(t,p)], \tag{2.57}$$

$$i\frac{\rm d}{{\rm dt}}\bar{\rho}(t,p) = [-\Omega(p) + V_{\rm eff}(t,p), \bar{\rho}(t,p)]. \tag{2.58}$$

These equations are general equation of motion of (anti)neutrino oscillations without Boltzmann collisions [45, 53].

2.7 Two flavor neutrino oscillations inside an electron background

We focus on a property of the MSW resonance in two flavor neutrino oscillations. Neutrinos produced at the center of a star are propagating outwards. Number density of background electrons naturally decreases toward the surface of the star. During flights of neutrinos, significant flavor transitions occur if the background electron density passes the critical density of MSW resonance. Observed neutrino spectra are affected by such matter effect. Actually, the solar neutrino problem [1, 5], i.e. smaller solar ν_e events than the theoretical prediction, had been solved by such MSW resonances. As discussed in §2.3, flavor transitions of traveling neutrinos can be studied from the equation of motion in Eq.(2.45) by replacing the time t with the radius r. The total Hamiltonian in two flavor neutrinos is given by

$$\Omega(E) + V_{\rm MSW} = \frac{\Delta m^2}{4E} \begin{pmatrix} -\cos 2\theta & \sin 2\theta \\ \sin 2\theta & \cos 2\theta \end{pmatrix} + \frac{\sqrt{2}}{2} G_F n_e(r) \begin{pmatrix} 1 & 0 \\ 0 & -1 \end{pmatrix}, \tag{2.59}$$

where $n_e(r)$ is the net electron number density at the radius r and the matrix which is proportional to identity $I_{2\times2} = \mathrm{diag}(1,1)$ is removed. In general, we can not solve Eq.(2.45) analytically because of the radial dependence in $n_e(r)$. However, behaviors of flavor transitions are explained analytically if the electron density decreases much slower than the oscillation time scale. The total Hamiltonian in Eq.(2.59) is diagonalized by some unitary matrix U_M:

$$\Omega(E) + V_{\mathrm{MSW}} = \frac{\Delta m^2_M}{4E} \begin{pmatrix} -\cos 2\theta_M & \sin 2\theta_M \\ \sin 2\theta_M & \cos 2\theta_M \end{pmatrix} = U_M \Omega'(t,E) U_M^\dagger, \tag{2.60}$$

$$\Omega'(r,E) = \frac{-\Delta m^2_M}{4E} \begin{pmatrix} 1 & 0 \\ 0 & -1 \end{pmatrix}, \tag{2.61}$$

where the effective mass difference Δm^2_M and the mixing angle $\theta_M \in [0,\pi]$ is defined by

$$U_M = \begin{pmatrix} \cos\theta_M & \sin\theta_M \\ -\sin\theta_M & \cos\theta_M \end{pmatrix}, \tag{2.62}$$

$$\tan 2\theta_M = \frac{\Delta m^2 \sin 2\theta}{\Delta m^2 \cos 2\theta - 2\sqrt{2} G_F n_e(r) E}, \tag{2.63}$$

$$\Delta m^2_M = \mathrm{sgn}(\Delta m^2) \sqrt{\left(-\Delta m^2 \cos 2\theta + 2\sqrt{2} G_F n_e(r) E\right)^2 + (\Delta m^2 \sin 2\theta)^2}, \tag{2.64}$$

where $\mathrm{sgn}(x)$ is the sign of x. The mixing angle θ_M connects flavor eigenstate with the energy eigenstate inside electron background:

$$\begin{pmatrix} \nu_e \\ \nu_x \end{pmatrix} = U_M \begin{pmatrix} \nu'_1 \\ \nu'_2 \end{pmatrix}, \tag{2.65}$$

where (ν'_1) ν'_2 has energy eigenvalue $(-)\Delta m^2_M/4E$. The effective mixing angle θ_M is sensitive to the background electron density $n_e(r)$, so that the value of θ_M depends on the radius r. This is a level crossing phenomenon of a two-level system in quantum mechanics [99–101]. The left panel of Fig.2.3 shows the value of effective neutrino

mass square inside an electron background:

$$m^2_{M,1} = \frac{m^2_1 + m^2_2 + 2\sqrt{2}G_F n_e E}{2} - \frac{\Delta m^2_M}{2}, \tag{2.66}$$

$$m^2_{M,2} = \frac{m^2_1 + m^2_2 + 2\sqrt{2}G_F n_e E}{2} + \frac{\Delta m^2_M}{2}. \tag{2.67}$$

where the first terms of Eqs.(2.66) and (2.67) are components of the Hamiltonian which are proportional to $I_{2\times2}$. The level crossing (resonance) occurs when the diagonal components of Eq.(2.59) disappears:

$$\frac{\Delta m^2}{2E}\cos 2\theta = \sqrt{2}G_F n_e(r), \tag{2.68}$$

where the flavor mixing becomes maximum $\theta_M = \pi/4$ (see the right panel of Fig.2.3). This level crossing phenomenon is called MSW effect [41, 42]. The critical electron density of MSW resonance is given by

$$n_{e,cr} = \frac{\Delta m^2 \cos 2\theta}{2\sqrt{2}G_F E}. \tag{2.69}$$

For dense electron background $n_e(r) >> n_{e,cr}$, flavor eigenstates $\{\nu_\alpha\}_{\alpha=e,x}$ are energy eigenstates because of $\theta_M \sim \pi/2$. On the other hand, vacuum mass eigenstates $\{\nu_i\}_{i=1,2,3..}$ correspond to energy eigenstate for $n_e(r) << n_{e,cr}$. The adiabatic theorem [102, 103] states that if the non-degenerate Hamiltonian changes gradually, the nth energy eigenstate of initial Hamiltonian H^i is transformed to nth energy eigenstate of final Hamiltonian H^f. Therefore, an electron type neutrino $\nu_e \sim \nu'_2(n_e >> n_{e,cr})$ produced deep inside a star is transformed into $\nu'_2(n_e = 0) = \nu_2$ during the neutrino propagation if the time-dependent matrix in Eq.(2.62) evolves much slower than the time scale of flavor transitions:

$$\left|\frac{\mathrm{d}\theta_\mathrm{M}}{\mathrm{dr}}\right|^{-1} >> \left(\frac{\Delta m^2_M}{4E}\right)^{-1}, \tag{2.70}$$

which is equivalent to the condition of the gamma factor [89]:

$$\gamma_{\mathrm{matter}} >> 1, \tag{2.71}$$

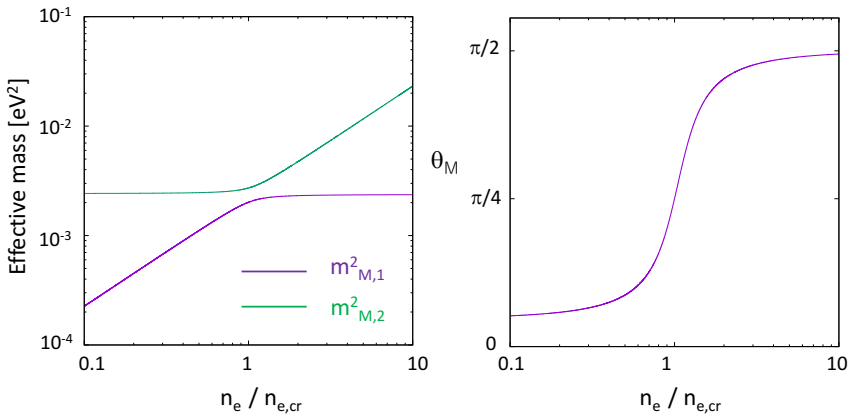

Figure 2.3: The left panel represents Eqs.(2.66) and (2.67) with electron number density n_e. Here, we set $m_1^2 = 0$, $m_2^2 = \Delta m^2 = 2.4 \times 10^{-3}$ eV^2, $\theta = 0.15$ rad and $E = 30$ MeV. The level crossing occurs at $n_e = n_{e,cr}$. The right panel shows the value of effective mixing angle defined in Eq.(2.63).

$$\gamma_{\rm matter} = \frac{\Delta m^2 \sin^2 2\theta \ n_e}{2E \cos 2\theta |{\rm dn_e/dr}|}. \tag{2.72}$$

Let's derive a survival probability of ν_e affected by the MSW resonance for $\Delta m^2 > 0$. We carry out an unitary transformation in a neutrino density matrix: $\rho(r, E) \mapsto U_M \rho'(r, E) U_M^\dagger$. Then, the time evolution of Eq.(2.45) is described by

$$i\frac{\rm d}{\rm dr}\rho'(r,E) = [\Omega'(r,E) - iU_M^\dagger \frac{{\rm dU_M}}{\rm dr}, \rho'(r,E)], \tag{2.73}$$

$$-iU_M^\dagger \frac{{\rm dU_M}}{\rm dr} = \frac{{\rm d}\theta_{\rm M}}{\rm dr}\begin{pmatrix} 0 & -i \\ i & 0 \end{pmatrix}. \tag{2.74}$$

The non-diagonal term in Eq.(2.74) is ignored if the condition of Eq.(2.70) is satisfied.

In this adiabatic limit, we can solve Eq.(2.73) analytically:

$$\rho'(r,E) \sim \begin{pmatrix} e^{i\int_0^r \mathrm{ds}\ \frac{\Delta \mathrm{m}^2_{\mathrm{M}}}{4\mathrm{E}}\mathrm{s}} & 0 \\ 0 & e^{-i\int_0^r \mathrm{ds}\ \frac{\Delta \mathrm{m}^2_{\mathrm{M}}}{4\mathrm{E}}\mathrm{s}} \end{pmatrix} \rho'(0,E) \begin{pmatrix} e^{-i\int_0^r \mathrm{ds}\ \frac{\Delta \mathrm{m}^2_{\mathrm{M}}}{4\mathrm{E}}\mathrm{s}} & 0 \\ 0 & e^{i\int_0^r \mathrm{ds}\ \frac{\Delta \mathrm{m}^2_{\mathrm{M}}}{4\mathrm{E}}\mathrm{s}} \end{pmatrix}. \tag{2.75}$$

We remark that neutrinos keep staying energy eigenstates: $\rho'(r,E) \sim \rho'(0,E)$ if the initial condition is given by the energy eigenstates. Flavor eigenstates are nearly energy eigenstates in a dense electron background. Here, we impose Eq.(2.25) as the initial condition. In addition, we assume that $n_e >> n_{e,cr} (\leftrightarrow \theta_M \sim \pi/2)$ is satisfied at $r = 0$. Then, Eq.(2.75) after the MSW resonance is given by

$$\begin{pmatrix} \rho_{11}(r,E) & \rho_{12}(r,E) \\ \rho_{21}(r,E) & \rho_{22}(r,E) \end{pmatrix} \sim \begin{pmatrix} 0 & 1 \\ 1 & 0 \end{pmatrix} \begin{pmatrix} \rho_{ee}(0,E) & \rho_{ex}(0,E) \\ \rho_{xe}(0,E) & \rho_{xx}(0,E) \end{pmatrix} \begin{pmatrix} 0 & 1 \\ 1 & 0 \end{pmatrix} = \begin{pmatrix} 0 & 0 \\ 0 & 1 \end{pmatrix}. \tag{2.76}$$

The ν_e inside the star ($n_e >> n_{e,cr}$) is completely transformed to ν_2 in vacuum ($n_e << n_{e,cr}$). Such adiabatic flavor transition follows the evolution of ν_2' in the left panel of Fig.2.3 (the green line). The vacuum mass eigenstate ν_2 is mixing of flavor eigenstates: $\nu_2 = \nu_e \sin\theta + \nu_x \cos\theta$. Then, the survival probability of ν_e is obtained by

$$P(\nu_e \to \nu_e) = \sin^2\theta, \tag{2.77}$$

which is negligible for small mixing angle. Therefore, significant flavor transitions are caused by MSW effect in a small mixing angle.

As shown in Eq.(2.68), the resonance condition is sensitive to the sign of Δm^2. For $\Delta m^2 < 0$, there is no MSW resonance and the effective mixing angle θ_M in Eq.(2.63) becomes zero in a dense electron background, so that ν_e is nearly corresponding to ν_1' for $n_e >> n_{e,cr}$. If flavor transitions occur adiabatically, ν_e produced in dense matter is completely converted into $\nu_1 = \nu_e \cos\theta - \nu_x \sin\theta$ in vacuum. The survival probability of ν_e is

$$P(\nu_e \to \nu_e) = \cos^2\theta, \tag{2.78}$$

which is nearly unity for a small mixing angle. The matter potential does not contribute to flavor transitions in a small mixing angle for $\Delta m^2 < 0$. In general, neutrino

oscillations inside medium such as electron and neutrino backgrounds are sensitive to the sign of Δm^2 which reflects the neutrino mass hierarchy in Fig.2.2. Supernova neutrinos detected in neutrino observatories also depend on the neutrino mass hierarchy.

Until now, we only focus on matter effect in the neutrino sector. How about in the antineutrino sector? The extra negative sign is multiplied by the vacuum Hamiltonian Ω in the antineutrino sector as shown in Eq (2.58). Therefore, the above discussion in the neutrino sector is totally reversed in the antineutrino sector. The MSW resonance occurs in antineutrinos for $\Delta m^2 < 0$. Then, the survival probabilities of Eqs.(2.77) and (2.78) have opposite relations in the antineutrino sector:

$$P(\bar{\nu}_e \to \bar{\nu}_e) = \begin{cases} \cos^2\theta & (\Delta m^2 > 0) \\ \sin^2\theta & (\Delta m^2 < 0). \end{cases} \tag{2.79}$$

2.8 The origin of non-linear potential caused by neutrino self interactions

Both vacuum neutrino oscillations and MSW effects have already been confirmed in various neutrino experiments. However, neutrino oscillations have still unknown phenomenology in our nature. It is implied that another type of flavor transition exists inside explosive astrophysical sites where large number of neutrinos are produced [43, 44]. Coherent forward scatterings with background electrons induce a matter potential in neutrino flavor space as shown in § 2.5. Such refractive potential can be also derived from neutrino self interactions such as

$$\nu_\alpha + \nu_\beta \to \nu_\alpha + \nu_\beta, \tag{2.80}$$

$$\nu_\alpha + \bar{\nu}_\beta \to \nu_\alpha + \bar{\nu}_\beta, \tag{2.81}$$

$$\nu_\alpha + \bar{\nu}_\alpha \to \nu_\beta + \bar{\nu}_\beta, \tag{2.82}$$

$$\bar{\nu}_\alpha + \bar{\nu}_\beta \to \bar{\nu}_\alpha + \bar{\nu}_\beta, \tag{2.83}$$

where $\alpha, \beta = e, \mu, \tau...$ Eqs.(2.80), (2.81) and (2.83) are (anti)neutrino scattering processes themselves. Eq.(2.82) represents neutrino-antineutrino pair processes. These interactions are neutral current reactions exchanging Z^0 boson. If neutrino energy is much smaller than the mass of Z^0 boson ($\sim$ 90 GeV), the effective Hamiltonian of neutrino self interactions is described by

$$\hat{H}_{NC} = \frac{G_F}{4\sqrt{2}} \int \mathrm{d}^3x \ \bar{\nu}_\alpha(x)\gamma^\mu(1-\gamma_5)\bar{\nu}_\alpha(x) \ \bar{\nu}_\beta(x)\gamma_\mu(1-\gamma_5)\bar{\nu}_\beta(x) = \hat{V}_{12}^{\nu\nu} + \hat{V}_{12}^{\nu\bar{\nu}} + \hat{V}_{12}^{\bar{\nu}\bar{\nu}}, \tag{2.84}$$

where

$$\hat{V}_{12}^{\nu\nu} = \frac{1}{2} \int \frac{\mathrm{d}^3\mathrm{p}}{(2\pi)^3} \frac{\mathrm{d}^3\mathrm{q}}{(2\pi)^3} \frac{\mathrm{d}^3\mathrm{p}'}{(2\pi)^3} \frac{\mathrm{d}^3\mathrm{q}'}{(2\pi)^3} \ V_{12}^{\nu\nu}(p,q;p',q')_{\beta_1\beta_2;\alpha_1\alpha_2} \ \hat{a}^\dagger_{\beta_1}(p)\hat{a}^\dagger_{\beta_2}(q)\hat{a}_{\alpha_2}(q')\hat{a}_{\alpha_1}(p'), \tag{2.85}$$

$$\hat{V}_{12}^{\nu\bar{\nu}} = \int \frac{\mathrm{d}^3\mathrm{p}}{(2\pi)^3} \frac{\mathrm{d}^3\mathrm{q}}{(2\pi)^3} \frac{\mathrm{d}^3\mathrm{p}'}{(2\pi)^3} \frac{\mathrm{d}^3\mathrm{q}'}{(2\pi)^3} \ V_{12}^{\nu\bar{\nu}}(p,q;p',q')_{\beta_1\beta_2;\alpha_1\alpha_2} \ \hat{a}^\dagger_{\beta_1}(p)\hat{b}^\dagger_{\beta_2}(q)\hat{b}_{\alpha_2}(q')\hat{a}_{\alpha_1}(p'), \tag{2.86}$$

$$\hat{V}_{12}^{\bar{\nu}\bar{\nu}} = \frac{1}{2} \int \frac{\mathrm{d}^3\mathrm{p}}{(2\pi)^3} \frac{\mathrm{d}^3\mathrm{q}}{(2\pi)^3} \frac{\mathrm{d}^3\mathrm{p}'}{(2\pi)^3} \frac{\mathrm{d}^3\mathrm{q}'}{(2\pi)^3} \ V_{12}^{\bar{\nu}\bar{\nu}}(p,q;p',q')_{\beta_1\beta_2;\alpha_1\alpha_2} \ \hat{b}^\dagger_{\beta_1}(p)\hat{b}^\dagger_{\beta_2}(q)\hat{b}_{\alpha_2}(q')\hat{b}_{\alpha_1}(p'), \tag{2.87}$$

where $\hat{V}_{12}^{\nu\nu}$, $\hat{V}_{12}^{\nu\bar{\nu}}$ and $\hat{V}_{12}^{\bar{\nu}\bar{\nu}}$ are corresponding to the second quantized Hamiltonians of $\nu\nu$ scatterings, $\nu\bar{\nu}$ interactions and $\bar{\nu}\bar{\nu}$ scatterings, respectively.

Here, we derive an effective potential of neutrino self interactions in neutrino sector. The same effective potential is obtained in the antineutrino sector by considering Eq.(2.87) instead of Eq.(2.85). The antineutrino system $\bar{S}$ is regarded as the background for the neutrino system S. In analogy with Eq.(2.38), the time evolution of the reduced density operator of S is obtained by a trace over $\bar{S}$:

$$i\frac{\mathrm{d}}{\mathrm{dt}}\hat{\rho}_S = [\hat{\Omega}, \hat{\rho}_S] + [\hat{V}_{12}^{\nu\nu}, \hat{\rho}_S] + \mathrm{Tr}_{\bar{\mathrm{S}}}[\hat{\mathrm{V}}_{12}^{\nu\bar{\nu}}, \hat{\rho}], \tag{2.88}$$

$$\hat{\rho}_S = \mathrm{Tr}_{\bar{\mathrm{S}}}[\hat{\rho}]. \tag{2.89}$$

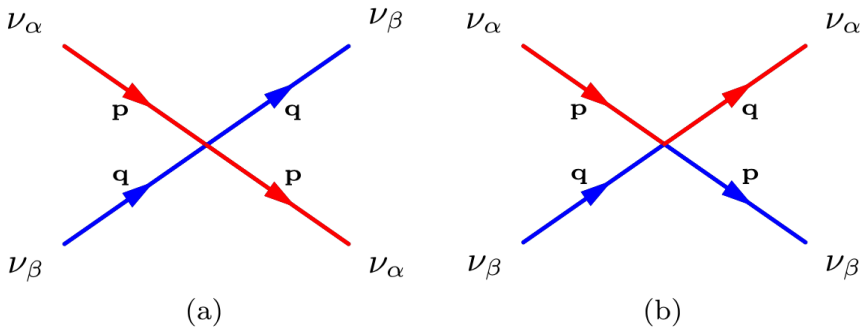

Figure 2.4: (a) forward and (b) momentum exchange diagrams of $\nu_\alpha + \nu_\beta \to \nu_\alpha + \nu_\beta$ [104].

Within the Born approximation, the density operator of total system $\hat{\rho}$ becomes a product of reduced density operator of neutrino system $\hat{\rho}_S$ and that of antineutrino system $\hat{\rho}_{\bar{S}}$:

$$\hat{\rho} \sim \hat{\rho}_S \otimes \hat{\rho}_{\bar{S}}. \tag{2.90}$$

Owing to the Born approximation, Eq.(2.88) becomes

$$i\frac{\mathrm{d}}{\mathrm{dt}}\hat{\rho}_S = [\hat{\Omega} + \hat{\bar{V}}_{12}^{\nu\bar{\nu}}, \hat{\rho}_S] + [\hat{V}_{12}^{\nu\nu}, \hat{\rho}_S], \tag{2.91}$$

$$\hat{\bar{V}}_{12}^{\nu\bar{\nu}} = \mathrm{Tr}_{\bar{S}}\{\hat{V}_{12}^{\nu\bar{\nu}}\hat{\rho}_{\bar{S}}\}, \tag{2.92}$$

where $\hat{\bar{V}}_{12}^{\nu\bar{\nu}}$ is an effective one-body Hamiltonian induced by the antineutrino background. Then, the time evolution of one-body ensemble average $\langle \hat{a}^\dagger_{\beta_1}(p)\hat{a}_{\alpha_1}(p')\rangle$ is described by

$$\begin{aligned} i\frac{\mathrm{d}}{\mathrm{dt}}\langle \hat{a}^\dagger_{\beta_1}(p)\hat{a}_{\alpha_1}(p')\rangle = &\left(\Omega(p) + \tilde{V}_{12}^{\nu\bar{\nu}}(t,p)\right)_{\alpha_1 k}\langle \hat{a}^\dagger_{\beta_1}(p)\hat{a}_k(p')\rangle - \langle \hat{a}^\dagger_k(p)\hat{a}_{\alpha_1}(p')\rangle\left(\Omega(p) + \tilde{V}_{12}^{\nu\bar{\nu}}(t,p)\right)_{k\beta_1} \\ &+ \langle [\hat{a}^\dagger_{\beta_1}(p)\hat{a}_{\alpha_1}(p'), \hat{V}_{12}^{\nu\nu}]\rangle, \end{aligned} \tag{2.93}$$

where the second line of Eq.(2.93) includes ensemble average of two-body operator such as $\langle \hat{a}^\dagger_{\beta_1}(p)\hat{a}^\dagger_{\beta_2}(q)\hat{a}_{\alpha_2}(q')\hat{a}_{\alpha_1}(p')\rangle$ because $\hat{V}_{12}^{\nu\nu}$ is the two-body operator in the neutrino many-body system. In order to solve Eq.(2.93), we also need the equation of motion of two-body ensemble average which includes contribution from three-body

ensemble averages. In general, the equation of motion of N-body ensemble average $\langle \hat{a}_1^\dagger \hat{a}_2^\dagger .. \hat{a}_N^\dagger \hat{a}_N .. \hat{a}_2 \hat{a}_1 \rangle$ has a higher order contribution from $N+1$-body ensemble average $\langle \hat{a}_1^\dagger \hat{a}_2^\dagger .. \hat{a}_N^\dagger \hat{a}_{N+1}^\dagger \hat{a}_{N+1} \hat{a}_N .. \hat{a}_2 \hat{a}_1 \rangle$, so that the equation is not closed. This is called the Bogoliubov-Born-Green-Kirkwood-Yvon (BBGKY) hierarchy [105–108]. In order to close equation of motion of $N-$body ensemble average, we should replace the $N+1-$body ensemble average with $M-$body ones ($M = 1, 2, .., N$). Within the mean-field approximation [45, 48, 51, 53], the ensemble average of two-body operator is described by a product of one-body ensemble averages:

$$\langle \hat{a}_{\beta_1}^\dagger(p) \hat{a}_{\beta_2}^\dagger(q) \hat{a}_{\alpha_2}(q') \hat{a}_{\alpha_1}(p') \rangle = \langle \hat{a}_{\beta_1}^\dagger(p) \hat{a}_{\alpha_1}(p') \rangle \langle \hat{a}_{\beta_2}^\dagger(q) \hat{a}_{\alpha_2}(q') \rangle - \langle \hat{a}_{\beta_1}^\dagger(p) \hat{a}_{\alpha_2}(q') \rangle \langle \hat{a}_{\beta_2}^\dagger(q) \hat{a}_{\alpha_1}(p') \rangle, \tag{2.94}$$

where the negative sign of the second term accounts for spin statistics of fermions. Such decomposition of two-body ensemble average induces a mean-field potential $\tilde{V}_{12}^{\nu\nu}$:

$$\langle [\hat{a}_{\beta_1}^\dagger(p) \hat{a}_{\alpha_1}(p'), \hat{V}_{12}^{\nu\nu}] \rangle = \tilde{V}_{12}^{\nu\nu}(t,p)_{\alpha_1 k} \langle \hat{a}_{\beta_1}^\dagger(p) \hat{a}_k(p') \rangle - \langle \hat{a}_k^\dagger(p) \hat{a}_{\alpha_1}(p') \rangle \tilde{V}_{12}^{\nu\nu}(t,p)_{k\beta_1}, \tag{2.95}$$

$$\tilde{V}_{12}^{\nu\nu}(t,p)_{\beta\alpha} = \sqrt{2} G_F \int \frac{\mathrm{d}^3 q}{(2\pi)^3} (1 - \cos\theta_{pq}) \left\{ \mathrm{tr_F}[\rho(\mathrm{t,q})] \delta_{\beta\alpha} + \rho(\mathrm{t,q})_{\beta\alpha} \right\}, \tag{2.96}$$

where $\mathrm{tr_F}[\rho(\mathrm{t,q})] = \sum_\alpha \rho_{\alpha\alpha}(\mathrm{t,q})$ and θ_{pq} represents the scattering angle between momentum p and momentum q. The first term of the right hand side of Eq.(2.96) comes from the forward coherent scattering in Fig.2.4(a) which does not contribute to any flavor transitions. On the other hand the second term of Eq.(2.96) represents a refractive effect from a momentum exchanging diagram in Fig.2.4(b) which has influence on flavor transitions. The non-linear potential of neutrino self interactions is obtained in the time evolution of neutrino one-body density matrix [45]:

$$V_{\mathrm{self}}(t,p) = \sqrt{2} G_F \int \frac{\mathrm{d}^3 q}{(2\pi)^3} (1 - \cos\theta_{pq}) \left\{ \rho(t,q) - \bar{\rho}(t,q) \right\}, \tag{2.97}$$

where the integrand of Eq.(2.97) includes neutrino and antineutrino matrices, so that we should solve flavor transitions of different momentum (anti)neutrinos simultaneously together with the non-linear potential. Non-diagonal components of Eq.(2.97) grow up dynamically once non-diagonal components appear in $\rho(t,q)$ and $\bar{\rho}(t,q)$,

which triggers significant flavor transitions in neutrino fluxes. Neutrino self interactions are negligible if vacuum Hamiltonian is much larger than the non-linear potential: $\Omega(p) >> V_{\rm self}(t,p)$. Therefore, the non-linear flavor conversions do not appear except for explosive astrophysical sites where large number of neutrinos exist. Numerical simulations of neutrino oscillations considering neutrino self interactions are carried out in core-collapse supernovae [58–84], early universe [109–112], neutron star mergers [113–115] and long gamma-ray bursts [116]. Non-linear flavor transitions are sensitive to neutrino distribution in the phase space, so that we should assume some model of neutrino emissions depending on astrophysical sites. In the next chapter, we show numerical results of non-linear flavor transitions by using the bulb-model [58] which is well employed as neutrino emission geometry in core-collapse supernova.

2.9 The relation between neutrino oscillations and Boltzmann collisions

The refractive potential in neutrino flavor space is caused by coherent forward scatterings between neutrinos with background medium. There is no momentum loss or gain through neutrino oscillations, so that the number of each momentum neutrino is always conserved: $\mathrm{tr}_F[\rho(t,p)] = \sum_\alpha \rho_{\alpha\alpha}(t,p) = \text{const.}$. The contributions from absorption, creation and non-forward scatterings of emitting neutrinos are taken into account in the neutrino transport as Boltzmann collisions $C(t,p)$ [52,54]. Momentum transfer is possible owing to the Boltzmann collision, which increases the entropy of neutrino many-body system. Furthermore, $\mathrm{tr}_F[\rho(t,p)]$ is no longer conserved quantity because of $\mathrm{tr}_F[\dot{\rho}(t,p)] = \mathrm{tr}_F[C(t,p)]$. Therefore, the Boltzmann collision would give rise to dissipation and damping of neutrino oscillations. A refractive potential in neutrino flavor space belongs to the first order of G_F but the Boltzmann collision comes from second order terms $\propto G_F^2$ in the perturbation expansion [45, 53]. For example, let's consider charged current reaction $\nu_e + e^- \to e^- + \nu_e$. The perturbation

expansion of Eq.(2.38) is described by

$$i\frac{\mathrm{d}}{\mathrm{dt}}\hat{\rho}_S \sim [\hat{\Omega}, \hat{\rho}_S] + [\hat{\tilde{V}}_{\nu e}, \hat{\rho}_S] - i\int_{-\infty}^{\infty} \mathrm{dt}'\ \frac{1}{2}\left\{ \mathrm{Tr_B}[\hat{\mathrm{V}}_{\nu\mathrm{e}}(\mathrm{t}'), [\hat{\mathrm{V}}_{\nu\mathrm{e}}, \hat{\rho}_{\mathrm{S}}\hat{\rho}_{\mathrm{B}}]\ ] - [\hat{\tilde{\mathrm{V}}}_{\nu\mathrm{e}}(\mathrm{t}'), [\hat{\tilde{\mathrm{V}}}_{\nu\mathrm{e}}, \hat{\rho}_{\mathrm{S}}]\ ] \right\}, \tag{2.98}$$

where the second term of the right hand side represents the refractive potential which is proportional to G_F. On the other hand, the third term of Eq.(2.98) shows the contribution from non-forward scatterings up to the second order of G_F by assuming molecular chaos (or Markov approximation) [45, 98]. This third term is the origin of the Boltzmann collision $C(t, p)$ which is ignored under the Born approximation in Eq.(2.39). Here, we focus on one weak reaction, but the kinetic equation considering flavor mixing and other Boltzmann collisions are obtained in previous works [45–47, 49, 50, 52, 54]. Such derived equations corresponds to a Lindblad master equation [98] in neutirno many-body system. The combination of refractive potential and Boltzmann collisions are especially important for neutrino decoupling from the thermal bath in the early universe [112].

Chapter 3

Supernova mechanism and properties of collective neutrino oscillations

In this chapter, the standard scenario of core-collapse supernova explosion is reviewed. We introduce mechanism how large numbers of neutrinos are produced deep inside of the core. Then, we show numerical results of collective neutrino oscillations outside a neutrino sphere by employing two flavor single angle calculation. This simple model enables us to abstract fundamental properties of collective neutrino oscillations which are caused by neutrino self interactions. Especially, neutrino spectral swap in energetic (anti)neutrinos has important role for the detection of collective neutrino oscillations and the nucleosynthesis inside neutrino driven winds. Non-linear phenomena confirmed in this simple treatment are helpful to understand more complex behavior of non-linear flavor transitions in more realistic numerical scheme used in next chapters.

3.1 Stellar evolution

Stars are composed of large numbers of gas particles. The mass of star is huge ($> 10^{33}$g) and the quasi-static state of the system is realized by the balance between

self gravity and the inner pressure. Nuclear energy produced through nuclear fusion reactions inside the star maintains the temperature of the star and contributes to the thermal pressure competing with the self gravity. Such energy is transferred outwards through radiation and convection. Then, the star is shining through thermal radiation from the stellar surface. The energy loss of the star, for example, the thermal radiation induces reduction of gravitational energy Ω and increase of the internal energy U. This is clearly explained by using the Virial theorem of ideal gas:

$$\Omega + 3(\Gamma - 1)U = 0, \tag{3.1}$$

where Γ is the adiabatic index defined by

$$\Gamma = \left(\frac{\partial \ln P}{\partial \ln \rho} \right)_s, \tag{3.2}$$

where P, ρ and s are pressure, density and entropy per nucleon. The total energy of a star E is written as

$$E = \Omega + U = -(3\Gamma - 4)U. \tag{3.3}$$

The adiabatic index Γ should be larger than $4/3$ for a stable gravitationally bound state ($E < 0$). The energy loss $\mathrm{d}E < 0$ represents release of gravitational energy ($\mathrm{d}\Omega < 0$) and temperature increase ($\mathrm{d}U > 0$). The specific heat of stars is negative, which stabilizes stellar evolution. The core shrinks and the gravitational energy is reduced when the self gravity overcomes the central pressure. In such case, released gravitational energy raises up the central temperature because of the negative specific heat. Such increased temperature is helpful to support the self gravity of the core and maintain the high temperature through ignition of next nuclear burning.

Nuclear fusion reactions are sensitive to density and temperature of stars. Increased temperature during the stellar evolution enables the production of many isotopes from light to heavy elements through nuclear fusion reactions because high temperature is necessary for productions of heavy elements. Large Coulomb barriers of heavy elements prevent the penetration of low energy incident particles in nuclear fusion reactions, so that high temperature is required for high energy incident particles. Stars are mainly made of Hydrogen and helium at the initial burning stage.

When the temperature is larger than $\sim 10^7$ K, H-burning occurs and He core is formed at the center. Stars stay almost their lives in this H-burning stage. As the stellar evolution proceeds, produced helium accumulates at the center and fuel hydrogen for H-burning is exhausted. Then, the core shrinks and releases the gravitational energy, which increases the central temperature. He-burning ignites and produces carbon and oxygen at the center once the central temperature exceeds the threshold of He-burning ($\sim 10^8$ K). In the same way, heavy elements such as Ne, Mg and Si can be synthesized as the central density and temperature continue to increase during the stellar evolution. The termination of nuclear fusion reactions is at iron-group elements because nuclear binding energy per nucleon is maximum in such isotopes. However nuclear fusion reactions have finished before the creation of Fe core if the core is supported by degenerate pressure of electrons. In general, degenerate pressure of fermions is finite even if the temperature is zero. The core does not have to shrink in order to produce the thermal pressure when the degenerate pressure is comparable with the self gravity.

The stellar evolution is sensitive to the mass of stars. Fig.3.1 shows schematic evolution tracks of single stars of different masses in the central density-temperature (ρ_c-T_c) plane. In case of light mass stars ($M < 8M_\odot$), nuclear burning have finished up to He-burning because sufficient degenerate pressure prevents the contraction of the core. The evolution track of such a light star does not reach any instability region for dynamical equilibrium as shown, for example, by the track of $5M_\odot$ in Fig.3.1. Degenerate pressure at the center is produced by non-relativistic electrons during the stellar evolution, so that the adiabatic index becomes $\Gamma = 5/3 > 4/3$ which implies a stable core. In the end of the stellar evolution, outer layer of the star is stripped off and the core becomes a white dwarf (WD).

3.2 Stellar core-collapse

On the other hand, core-collapse occurs in more massive stars ($M > 8M_\odot$). There is a maximum mass of astrophysical objects which are supported by degenerate pressure

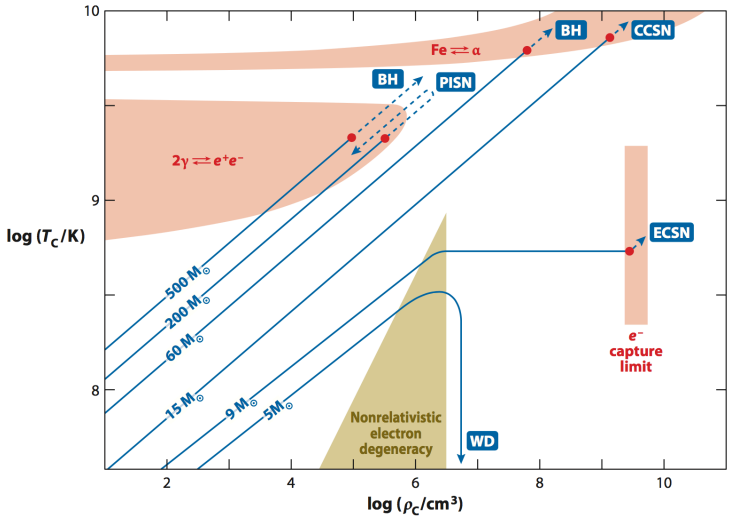

Figure 3.1: Schematic tracks of stellar evolution of various single star mass in the ρ_c-T_c plane [117]. The brown area shows nonrelativistic electron degeneracy inside the star, which implies no gravitational core-collapse. The light red areas represent the regions of instability for the core-collapse.

of electrons:

$$M_{\rm Ch} = 1.46 M_\odot \left(\frac{Y_e}{0.5}\right)^2, \tag{3.4}$$

where Y_e is an electron fraction. This is called "Chandrasekhar mass". In massive stars, electron degenerate pressure no longer supports the inner core once the mass of the inner core reaches some critical value near $M_{\rm Ch}$. This is the beginning of gravitational core-collapse of stars. There are three instabilities to induce core-collapse (light red region in Fig.3.1).

3.2.1 Electron capture supernovae

The evolution track of $9M_\odot$ in Fig.3.1 reaches the instability region of electron capture reactions. Electron capture reactions reduce degenerate pressure of electrons, which triggers the contraction of the inner core and results in an electron capture supernova (ECSN) [118–121]. The mass range of the progenitor for ECSN is very narrow $8 - 10M_\odot$ and sensitive to the metalicity [122, 123]. The oxygen-neon-magnesium (ONeMg) core is formed through C-burning inside the progenitor. Electron captures

on Mg and Na induce the core-collapse and subsequent ECSN [118, 119, 124]. Several candidates of ECSN are found in observations [125–127]. For example, the Crab pulsar SN1054 may be also a promissing one [128, 129]. The ratio of ECSN among all core-collapse supernovae is estimated by less than few percents [122, 123, 130].

3.2.2 Iron core-collpase supernovae

Let's focus on the stellar evolution to standard core-collapse supernovae (CCSN). The evolution tracks of $15M_\odot$ and $60M_\odot$ in Fig.3.1 pass an unstable region of photodisintegrations:

$$^{56}\mathrm{Fe} + \gamma \rightarrow 13\,^4\mathrm{He} + 4n - 124.4\mathrm{MeV}, \tag{3.5}$$

$$^4\mathrm{He} + \gamma \rightarrow 2p + 2n - 28.3\mathrm{MeV}. \tag{3.6}$$

At the center of massive stars, the iron core is formed through Ne-burning. The abundances of nuclear species follow the nuclear statistical equilibrium (NSE) states because of high temperature at the center ($T_c > 5 \sim 10^9$ K). Once the central temperature reaches $\sim 10^{10}$ K, photodisintegrations in Eqs.(3.5) and (3.6) are favored because the free energy of the system becomes minimum owing to increased entropy through these decompositions. These reactions reduce the temperature of the iron core, which decreases the adiabatic index Γ. The gravitational collapse of the iron core continues until the core becomes stiff because of repulsive short-range nuclear forces. Then, shock waves are produced and propagate outwards from the center. The evolution track of $15M_\odot$ represents the case where the shock waves can reach the surface of the star and the supernova explosion is successful. In this case, the inner core becomes a proto-neutron star. On the other hand, the supernova explosion is failed and a black hole (BH) is produced at the center in case of more massive progenitor as shown in the $60M_\odot$ track. The high mass accretion of outer material in massive progenitor prevents the penetration of the shock waves. BH is formed when the outer material continues to accumulate on the surface of the proto-neutron star. The overview of this standard explosion scenario is mentioned in the next section.

3.2.3 Pair-instability supernovae

The most massive star ($M > 100M_\odot$) may create pair-unstable oxygen cores after the C-burning at $T_c \sim 10^9$ K and $\rho_c < 10^6 \mathrm{g/cm}^3$. The gravitational instability is caused by the pair creation of an electron and a positron:

$$2\gamma \to e^- + e^+, \tag{3.7}$$

which converts thermal energy of photons to rest-mass energy of e^-e^+. This reaction reduces thermal pressure of photons and also decreases the value of adiabatic index Γ below 4/3. In the mass range of $100M_\odot < M < 140M_\odot$, an iron core is formed and core-collapse occurs subsequently after pulsation of the progenitor and large amount of mass ejection and mass loss. On the other hand, oxygen ignites explosively and the core-collapse has stopped in the mass range $140M_\odot < M < 260M_\odot$. Then, the thermonuclear explosion induces complete disruption of the star. Such supernova explosion is called pair-instability supernova (PISN) [131, 132]. The evolution track of $200M_\odot$ in Fig.3.1 corresponds to the PISN. Some observational counterparts of PISN have already been discovered [133–136]. The frequency of PISN is estimated by 0.01-1% of standard core-collapse supernova [137]. PISN is also one of the candidates for superluminous supernova (SLSN) whose explosion energy is 10 times or more higher than the typical explosion energy. The O-burning is not enough to stop the core-collapse for more massive star ($M > 260M_\odot$), which expects to create BH as shown by the evolution track of $500M_\odot$ in Fig.3.1.

3.3 Standard scenario of core-collapse supernovae

In previous section, we show three types of supernova caused by gravitational core-collapse. In the next chapters, we discuss behaviors of neutrino oscillations in iron core-collapse model and electron capture supernova (ECSN). Here, we only review the standard explosion scenario of iron core-collapse supernovae. After the core-collapse, the evolution of ECSN is similar to that of iron core-collapse.

3.3.1 Neutrino trapping

The iron core of the progenitor whose radius is around 1000 km is supported by degenerate pressure of electrons. Electrons inside the iron core are degenerate because of the high baryon density $\rho > 10^9 \mathrm{g/cm^3}$. The chemical potential (Fermi energy) of such electrons is given by

$$\mu_e = 3.9 \text{ MeV} \left(\frac{\rho}{10^{10} \mathrm{g/cm^3}} \frac{Y_e}{0.46} \right)^{\frac{1}{3}}, \tag{3.8}$$

where $Y_e \sim 26/46 = 0.46$ is an electron mass fraction inside the iron core. Gravitational collapse of the iron core is induced by the photodisintegrations of Fe and He. After the core-collapse, the central density increases, which promotes electron capture reactions on nuclei. For example, an electron capture reaction

$$^{56}\mathrm{Fe} + e^- \rightarrow {}^{56}\mathrm{Mn} + \nu_e, \tag{3.9}$$

occurs when the chemical potential of electorn μ_e in Eq.(3.8) exceeds the mass difference of nuclei: $m_{\mathrm{Mn}} - m_{\mathrm{Fe}} = 3.7$ MeV. The core-collapse of iron core is also accelerated by such electron capture reactions because degenerate pressure of electrons is reduced. Owing to this cycle, the central density and temperature increase and the value of Y_e decreases continuously during the core-collapse. The reduction of Y_e has stopped once produced ν_e is trapped inside the core. This is called "neutrino trapping" and helpful to successful supernova explosion. Neutrinos can escape freely at the beginning of the core-collapse but neutrinos are gradually trapped inside the core as the central density increases. A neutrino scattering with a nucleus A:

$$\nu + A \rightarrow \nu + A, \tag{3.10}$$

plays important role to prevent free streaming of neutrino emission in the dense core. The optical depth of neutrino at a radius r is defined by

$$\tau_\nu = \int_r^\infty \frac{\mathrm{d}r}{l_{\mathrm{mfp}}}, \tag{3.11}$$

where $l_{\rm mfp}$ is the mean free path of Eq.(3.10). The value of such optical depth becomes a criterion of neutrino interactions. The surface of neutrino sphere can be defined by the radius where $\tau_\nu \sim 1$ is satisfied. Neutrinos are well trapped deep inside the neutrino sphere ($\tau_\nu >> 1$). On the other hand, the neutrino emission can be regarded as a free streaming outside the neutrino sphere ($\tau_\nu << 1$). In dense core ($\rho > 10^{11}{\rm g/cm^3}$), random walks occur during the neutrino propagation because of $\tau_\nu > 1$. The neutrino propagation can be regarded as diffusion phenomenon at the large optical depth. The time scale of neutrino diffusion is estimated by

$$T_{\rm diffusion} \sim 7.3 \times 10^{-3}\ {\rm s} \left(\frac{\rho}{3 \times 10^{10}{\rm g/cm^3}}\right) \left(\frac{Y_e}{0.46}\right)^2 \left(\frac{A}{56}\right), \tag{3.12}$$

where A is the mass number of nuclei [138]. The time scale of core-collapse corresponds to the free fall time scale:

$$T_{\rm freefall} \sim \sqrt{\frac{3}{4\pi G\rho}} \sim 6.0 \times 10^{-3} \left(\frac{\rho}{10^{11}{\rm g/cm^3}}\right)^{-\frac{1}{2}}, \tag{3.13}$$

In dense region ($\rho > 10^{11}{\rm g/cm^3}$), $T_{\rm freefall}$ becomes smaller than $T_{\rm diffusion}$. Therefore, neutrinos can not escape from the core. Electron capture reactions have reached β-equilibrium owing to the neutrino trapping:

$$\mu_p + \mu_e = \mu_n + \mu_{\nu_e}, \tag{3.14}$$

Both electrons and neutrinos are degenerate inside the core. After the neutrino trapping, core-collapse proceeds adiabatically satisfying thermal equilibrium states which are characterized by the entropy per baryon $S \sim 1k_B$ and the lepton fraction $Y_L = Y_e + Y_{\nu_e} \sim 0.3 - 0.4$ [139,140]. Large value of Y_L increases the mass of the inner core, which helps the propagation of the shock waves.

3.3.2 Core-bounce and shock waves

As the core-collapse proceeds, the iron core is divided by the subsonic inner core and supersonic outer part. Fig.3.2 shows an example of the velocity profiles after the core-collapse. The double structure of the iron core is confirmed at the stages (1-4).

The inner core is supported by the degenerate pressure of leptons. The inner core becomes homologous and the velocity is proportional to the radius ($v \propto r$). On the other hand, the drop of the outer core is regarded as the free fall ($v \propto r^{-\frac{1}{2}}$). The collapse of the inner core stops suddenly at the center when the central density reaches the nuclear density ($\rho_{\rm nuc} \sim 3 \times 10^{14}{\rm g/cm^3}$). The nuclear repulsive force becomes effective in such dense matter and prevents the shrink of the inner core. The dynamical stability of the inner core is recovered and the value of adiabatic index is enhanced by up to $\Gamma \geq 2.8$ depending on the Equation of State (EoS) of nuclear matter [141]. The overshooting inner core rebounds owing to the stiff nuclear matter. After such core bounce, the sound wave is formed (5) at the center and propagates outwards (6-9). The information of the core bounce does not reach the outer core because of the supersonic fluid velocity. A shock wave is formed on the boundary between the inner core and the free falling outer core (10). The expanding inner core pushes the shock wave.The positive velocity peak begins to grow and the shock wave propagates outwards (11-14). The supernova explosion is successful if the shock wave reaches the surface of the star. This simple scenario is called "prompt explosion" [142]. Outer layers of the progenitor such as ONeMg and C layers are not obstacles to the shock propagation because the typical energy of supernova explosion ($\sim 10^{51}$ erg) is much larger than the gravitational energy of outer layers ($\sim 10^{50}$ erg). Therefore, supernova explosion is successful when the shock wave can pass through the outer core of the iron core.

The explosion energy depends on the mass and radius of the inner core. The size of the inner core is similar to that of the bounce core, which results in $M_{\rm bounce} \sim M_{\rm inner} = 0.5\text{-}0.8 M_\odot$. The initial energy of the shock wave is roughly given by the released gravitational energy of the inner core:

$$E^{(i)}_{\rm shock} \sim \frac{G M^2_{\rm bounce}}{R_{\rm bounce}} = 1.5 \times 10^{52}{\rm erg} \left(\frac{M_{\rm bounce}}{0.7 M_\odot}\right)^2 \left(\frac{R_{\rm bounce}}{100{\rm km}}\right)^{-1}, \tag{3.15}$$

where $R_{\rm bounce}$ is the radius of the bounce core. The inner mass is described as the Chandrasekhar mass of the leptons $M_{\rm inner} \propto Y_L^2$, so that the large lepton fraction caused by the neutrino trapping is favorable for the supernova explosion. The value

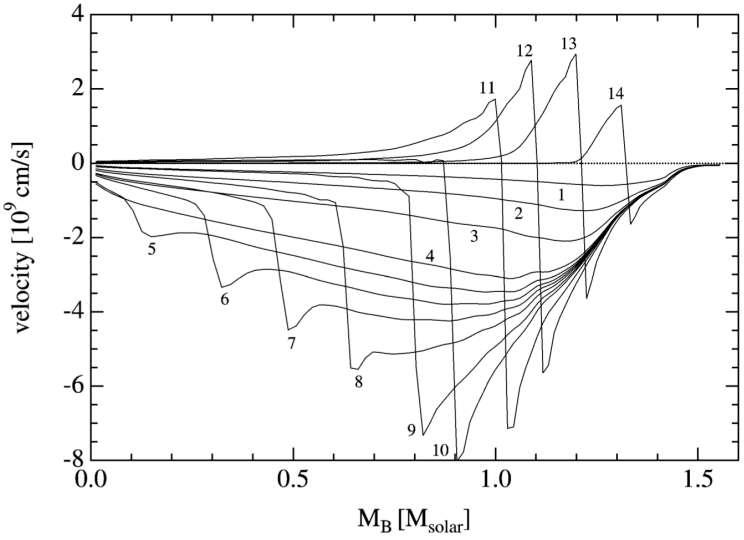

Figure 3.2: Velocity profiles of an iron core after the core-collapse labeled by different selected times [141]. The horizontal axis represents the baryon mass.

of $R_{\rm bounce}$ is sensitive to the EoS of nuclear matter. Soft EoSs are preferable for the small bounce radius. The value of Eq.(3.15) is one order larger than typical explosion energy $\sim 10^{51}$ erg but such explosion energy is reduced during the shock propagation. The Fe photo disintegration in Eq.(3.5) loses much kinetic energy of the shock wave. The amount of consumed energy to dissociate all of Fe in the outer core is estimated by

$$E_{\rm loss} \sim 1.1 \times 10^{52}{\rm erg} \left(\frac{M_{\rm Fe} - M_{\rm bounce}}{0.7 M_\odot} \right), \tag{3.16}$$

where $M_{\rm Fe} \sim 1.4 M_\odot$ is the mass of the initial iron core. Almost all of the initial explosion energy in Eq.(3.15) is used by the Fe photo disintegration. The Ram pressure of the falling outer core also decelerates the shock propagation. Furthermore, electron and positron capture reactions such as

$$e^- + p \to \nu_e + n, \tag{3.17}$$

$$e^+ + n \to \bar{\nu}_e + p, \tag{3.18}$$

and their following neutrino cooling also lose the thermal energy of the shock. These negative effects weaken the energy of the shock wave. Finally, the shock wave has

stopped before the surface of the iron core, which means a failure of the supernova explosion. This is a main problem for prompt explosion [26]. In order to revive the shock wave, other missing contribution should be taken into account.

3.3.3 Revival of stalled shock waves

The clarification of the mechanism to revive the stalled shock wave is one of the main subjects of supernova numerical studies. The neutrino heating mechanism certainly contributes to the revival of the shock. The gravitational energy of the iron core $\sim 10^{53}$ erg is released after the core-collapse. Only 1% of such gravitational energy is used to the supernova explosion energy. The remaining 99% of the gravitational energy is carried away by the diffusion of large numbers of neutrinos during 10 s. Such neutrinos are produced in the high temperature region after the shock wave propagation (see §3.3.4). The neutrino emission reduces the temperature of material near the proto-neutron star. On the other hand, in outer region, parts of emitted neutrinos can interact with material, which proceeds the revival of the stalled shock wave. Especially, charged current reactions:

$$\nu_e + n \to e^- + p, \tag{3.19}$$

$$\bar{\nu}_e + p \to e^+ + n, \tag{3.20}$$

can deposit much energy to the matter behind the shock wave. This shock revival mechanism is crucial for the balance between neutrino heating and cooling processes. The heating rate per nucleon Q^+[MeV/s/N] is given by

$$Q^+ \sim \frac{L_\nu}{4\pi r^2}\sigma_{\rm abs} \propto r^{-2}, \tag{3.21}$$

where L_ν and $\sigma_{\rm abs}$ are neutrino luminosity and a cross section of neutrino absorption such as Eqs.(3.19) and (3.20). The cooling rate per nucleon Q^-[MeV/s/N] is written as

$$Q^- \sim a\sigma_{\rm cap}T^4 \propto r^{-6}, \tag{3.22}$$

where a is the radiation constant and $\sigma_{\rm cap}$ is a cross section of a capture reaction such as Eqs.(3.17) and (3.18). Here, the gas temperature T is proportional to inverse radius r^{-1} [143]. The radial dependence of above heating and cooling rates implies that the neutrino cooling becomes dominant near the surface of the proto-neutron star and the neutrino heating occurs actively in outer region. The radius where both neutrino cooling and heating are balanced is the gain radius R_g. The typical value of R_g is 100 km [144]. The shock wave should exceed this radius in order to gain the neutrino energy. The neutrino heating occurs more effectively if the shock stays in outer region ($r > R_g$) for a long time. Fig.3.3 shows an example of the revival of the shock wave. Solid lines represent the evolutions of mass points. After the core bounce ($t = 0$ s), the shock wave (upper dash line) propagates outwards but the shock wave has stopped around 2×10^7 cm at $t = 0.2 - 0.5$ s. However, the stagnated shock wave is revived by neutrino heating in the later explosion phase ($t > 0.5$ s) and the supernova explosion is successful. The time scale of the explosion is delayed compared with that of the prompt explosion because some heating time of neutrino absorptions is required to increase the temperature behind the shock. Such behavior is called the "delayed explosion" [26].

The importance of neutrino heating for the supernova explosion is shown in Ref. [25, 26]. However, more developed numerical studies [140, 145] reveal that the shock revival does not occur in a spherical symmetric 1D explosion model. Neutrino heating is not enough for the shock revival of massive progenitor even though the 1D explosion is successful in the electron capture supernovae (ECSN) [120]. Multidimensional effects such as convection and standing accretion shock instability (SASI) [146] can increase the neutrino heating time outside the gain radius, which helps the shock revival. In current numerical resources, the 3D explosion simulation is possible [147, 148]. The propagations of the shock radius in different spacial dimensions are also surveyed [149, 150]. In addition to neutrino heating mechanism, the rotation and magnetic field also contribute to the supernova explosion [151–153]. Especially, the magnetohydrodynamical (MHD) explosion [152, 153] is regarded as the possible sites for r-process nucleosynthesis (see §5.1.2) because the ejecta of MHD explosion is not powered by the neutrino absorption in Eq.(3.19) which increases the value of Y_e.

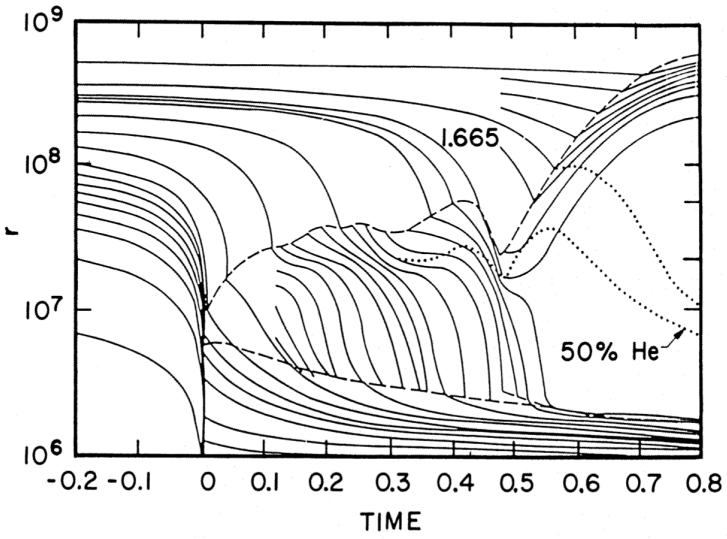

Figure 3.3: The example of the delayed explosion [25]. The solid lines correspond to trajectories of mass points. The upper (lower) dash line shows the position of the shock wave (neutrino sphere), respectively.

3.3.4 Neutrino spectra in core-collapse supernovae

We focus on mechanism of neutrino production in core-collapse supernovae step by step. After the core bounce, electron type neutrinos are created through electron capture reactions on nuclei such as Eq.(3.9). Such ν_e is trapped and degenerate inside the inner core as discussed in §3.3.1. The chemical potential of electron antineutrinos is given by $\mu_{\bar{\nu}_e} = -\mu_{\nu_e} < 0$, so that the creation of $\bar{\nu}_e$ is highly suppressed as long as ν_e is degenerate. After the core bounce, the shock wave can heat the accreting outer material. The shock heating induces photodisintegration of iron core and produces free nucleons, which enhances the production of ν_e through electron capture reactions because the cross section of Eq.(3.17) is larger than that of electron capture reactions on heavy nuclei [154]. Once the shock wave passes the neutrino sphere, large number of trapped electron type neutrinos are emitted outwards as the neutronization burst. The peak luminosity of ν_e around $t = 0.05$ s in the upper panel of Fig.3.4 corresponds to the neutronization burst. The luminosity of such ν_e burst is high $\sim 10^{53}$ erg/s but the duration of the burst is short ~ 0.01 s. The most of the released gravitational energy $\sim 10^{53}$ erg is carried away by neutrino emissions in more later explosion phase.

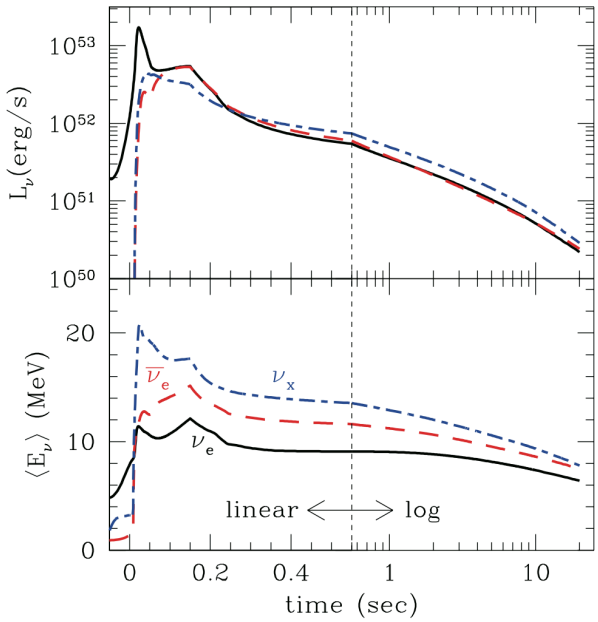

Figure 3.4: Evolutions of luminosities and mean energies of different species of neutrinos after the core-collapse [155]. The core bounce occurs at $t = 0$ s.

The emission of ν_e breaks the β-equilibrium in Eq.(3.14) and enhances electron capture reactions. The proto-neutron star finally settles down to a neutron star which satisfies a β-equilibrium without neutrinos: $\mu_p + \mu_e = \mu_n$.

The shock heating enables the creation of $\bar{\nu}_e$ and other flavor of neutrinos $\nu_X = (\nu_\mu, \nu_\tau, \bar{\nu}_\mu, \bar{\nu}_\tau)$. Electrons in the shock heated region are no longer degenerate. Such shock heating increases the temperature of material. In addition, the baryon density decreases as the shock waves propagates. These conditions are favorable for non-degenerate electrons and following electron-positron pair creation through Eq.(3.7). The positron capture reactions such as Eq.(3.18) produces electron antineutrinos. Furthermore, electron-positron pair annihilation can induce pairs of all flavors of neutrinos:

$$e^- + e^+ \to \nu_\alpha + \bar{\nu}_\alpha, \tag{3.23}$$

where $\alpha = e, \mu, \tau$. The bremsstrahlung of nucleons N also has a contribution to the neutrino pair creation:

$$N + N \to N + N + \nu_\alpha + \bar{\nu}_\alpha. \tag{3.24}$$

These pair reactions are main source of $\nu_X = (\nu_\mu, \nu_\tau, \bar{\nu}_\mu, \bar{\nu}_\tau)$ in core-collapse supernovae. Charged current reactions of μ and τ types are higly suppressed in core-collapse supernovae because chemical potential of electron should at least exceed the mass of muon (106 MeV) in order to create heavy charged leptons. Neutrino luminosities and mean energies are sensitive to environment around neutrino spheres. In the upper panel of Fig.3.4, luminosities of ν_e and $\bar{\nu}_e$ are increasing at $t = 0.05 - 0.15$ s, which reflects the released gravitational energy of the mass accretion [156]. The lower panel of Fig.3.4 shows the time evolution of neutrino mean energies. In case of the nondigenerate Fermi-Dirac distributions, the temperature of the neutrino sphere is estimated by $\langle E_\nu \rangle \sim 3T$ where T is the temperature of the neutrino sphere. We can confirm a energy hierarchy $\langle E_{\nu_e} \rangle < \langle E_{\bar{\nu}_e} \rangle < \langle E_{\nu_X} \rangle$, which indicates different temperatures of neutrino spheres depending on neutrino species. The radius of neutrino sphere is determined by the value of optical depth as discussed in §3.3.1. The μ and τ types neutrinos and their corresponding antineutrinos only interact through neutral current reactions. Therefore, the neutrino sphere of ν_X exists in highest temperature among all neutrino species. On the other hand, electron type neutrinos are trapped easily through the charged current reaction in Eq.(3.19) because of abundant free neutrons ($Y_e < 0.5$) near the proto-neutron star, which results in lowest temperature of the neutrino sphere. In the cooling phase ($t > 1$ s), neutrino luminosities and mean energies are decreasing during 10 s because of the contraction of the proto-neutron star and the neutrino cooling carrying large amount of gravitational energy of the iron core.

3.4 Neutrino oscillations inside core-collapse supernovae

In core-collapse supernovae, inelastic scatterings and absorption of neutrinos play important role for the explosion mechanism because neutrinos can deposit their energy to background matter and heat stalled shock waves. Inside the dense core, neutrinos are trapped and neutrino transport can be regarded as diffusion phenomenon (see §3.3.1). Reaction rates of neutrino scatterings and absorptions decrease gradually as neutrinos propagate outwards. Finally, neutrino emission becomes free-streaming outside the neutrino sphere where Boltzmann collisions, for example, the third term

on the right hand side of Eq.(2.98), become negligible in neutrino transport. The radius of neutrino sphere is well characterized by the radius which satisfies $\tau_\nu \sim 1$ in Eq.(3.11). In current supernova simulation, hydrodynamics and neutrino radiation including Boltzmann collisions are solved simultaneously. However, any quantum effects of neutrino oscillations are not taken into account in such neutrino transport because of limitation of numerical resources. Therefore, numerical simulation of supernova neutrino oscillations are usually implemented outside the neutrino sphere as a post process. In this thesis, we show the results of flavor transitions outside a neutrino sphere following usual treatment. However, consideration of Boltzmann collisions in neutrino oscillations is one of the active topics in the research field of supernova neutrino oscillations [157–162].

Neutrinos emitted from the neutrino sphere first experience collective neutrino oscillations where evolution of flavor becomes non-linear, so that significant flavor conversion occurs simultaneously irrespective of neutrino energy and species. Collective neutrino oscillations typically appear around $100 - 1000$ km from the center [58–84] where the strength of neutrino self interactions in Eq.(2.97) which is proportinal to neutrino number density is comparable with that of vacuum Hamiltonian in flavor space. In general, dramatic flavor conversion happens inside medium when the refractive potential caused by background particles couples with the neutrino vacuum Hamiltonian. This is also true for MSW matter resonance as shown in the resonance condition in Eq.(2.68). Numerical studies of collective neutrino oscillations in core-collapse supernovae have been undertaken in the last decade. The bulb model [58] is widely employed in the 1D explosion model. We also use this neutrino emission model. Numerical method of collective neutrino oscillations can be characterized by the number of neutrino flavors and the consideration of neutrino scattering angle. Three flavor multiangle simulation [70, 72, 73, 80, 82–84] is a common numerical treatment to study collective neutrino oscillations in 1D explosion model. Numerical results discussed in Chapter 4 and 5 are obtained by this calculation method. We remark that neutrino self interactions are sensitive to neutrino distributions in phase space, so that significant flavor conversions might be possible if we relax the geometrical symmetry of the bulb model in multi dimensional models of supernova explosion.

In recent studies, multi-azimuthal-angle (MAA) instability [77–79, 163, 164] and "fast flavor conversions" [165–170] are proposed as flavor instabilities caused by the relaxation of neutrino angular dependence. The linear stability analysis of fast flavor conversions is one of the hot topics in current oscillation studies [171–178]. Another interesting subject is the contribution of Nonstandard Interaction (NSI) on supernova neutrino oscillations [179–181], which has possibility to show traces of new physics beyond the standard model. It is expected that next galactic supernova neutrinos will deepen our understanding of neutrino self interactions in core-collapse supernovae.

After collective neutrino oscillations ($\sim \mathcal{O}(1000)$ km), MSW matter effects have influence on neutrino spectra at the critical electron number density in Eq.(2.68). In three flavor neutrinos, there are two MSW resonances reflecting two vacuum frequencies: $\omega_{\rm solar} = \Delta m^2_{21}/2E$ and $\omega_{\rm atm} = |\Delta m^2_{32}|/2E$ in Eq.(2.32). The dependence of neutrino mass hierarchy on matter effects is included in H resonance as shown in Fig.4.9. The steep density gradient of matter profiles or the shock front prevents adiabatic flavor transitions at MSW resonances [182–185]. Neutrino spectra observed on the earth are sensitive to both collective neutrino oscillations and MSW matter effects after the core bounce. On the other hand, the presupernova neutrinos before the supernova explosion are affected by only MSW matter resonances, which can potentially distinguish the neutrino mass hierarchy [29, 186–188]. The detail of MSW matter effects on observational neutrino fluxes is discussed in §4.2.5.

3.5 The bulb model in collective neutrino oscillations

Some neutrino emission model is necessary to simulate non-linear flavor transitions. The bulb model [58] is frequently used in numerical simulation in core-collapse supernovae. All species of neutrinos are emitted isotropically from the same neutrino sphere. Neutrino transport is assumed to be a free streaming and steady state outside the neutrino sphere. Fig.3.5 represents the schematic picture of the bulb model. From the geometry of neutrino beam, we obtain

$$r \sin\theta_R = R_\nu \sin\theta, \tag{3.25}$$

$$\cos\theta = \sqrt{1 - \left(\frac{r}{R_\nu}\right)^2 \sin^2\theta_R}, \tag{3.26}$$

which indicates that the scattering angle θ is connecting with emission angle θ_R one by one if the radius r is given. Here, we consider the spherical symmetric and steady state, so that the time derivative of flavor transition of the free streaming neutrino only depends on a radius r and a scattering angle θ [61]:

$$\frac{\mathrm{d}}{\mathrm{dt}} = \cos\theta \frac{\partial}{\partial r}. \tag{3.27}$$

In the numerical simulation, we solve the time evolution of neutrino density matrices which are characterized by r, $\theta(\theta_R)$ and energy E. Here, we ignore the absorption and inelastic scattering of neutrinos during flavor transitions, so that the number of each momentum neutrino is conserved. For convenience, we separate number density of neutrinos from neutrino density matrices in Eqs.(2.16) and (2.52). Then, the traces of neutrino density matrices are normalized by unity:

$$\mathrm{tr_F}[\rho(\mathrm{r,E},\theta)] = \mathrm{tr_F}[\bar{\rho}(\mathrm{r,E},\theta)] = 1. \tag{3.28}$$

Owing to this normalization, the number density of neutrinos inside the non-linear potential in Eq.(2.97) is described by luminosity L_{ν_α} [erg/s], mean energy $\langle E_{\nu_\alpha}\rangle$ [MeV] and the normalized spectra f_{ν_α} of ν_α on the surface of neutrino sphere [58, 61]. Then, the self interaction acting on $\rho(r, E, \theta_p)$ is given by

$$\begin{aligned} V_{\mathrm{self}}(r,\theta_p) = \frac{\sqrt{2}G_F}{2\pi R_\nu^2} \int \mathrm{d}q\ \mathrm{d}(\cos\theta_q)\ (1 - \cos\theta_p \cos\theta_q) \\ \times \sum_{\alpha=\mathrm{all\ \ flavor}} \left\{ \frac{L_{\nu_\alpha}}{\langle E_{\nu_\alpha}\rangle} f_{\nu_\alpha}(q)\rho(r,q,\theta_q) - \frac{L_{\bar{\nu}_\alpha}}{\langle E_{\bar{\nu}_\alpha}\rangle} f_{\bar{\nu}_\alpha}(q)\bar{\rho}(r,q,\theta_q) \right\}, \end{aligned} \tag{3.29}$$

where $\cos\theta_q \in [\cos\theta_{\max}, 1]$ and the azimuthal angle ϕ_q is integrated. The maximum scattering angle $\theta_{\max}$ is obtained when the emission angle becomes maximum: $\theta_R = \pi/2$. The strength of neutrino self interaction decreases as the neutrino propagates outwards because of the radial dependence in $\cos\theta_{\max} = \sqrt{1 - (R_\nu/r)^2}$. Finally, we got the equation of motion of neutrino oscillations considering both matter effects

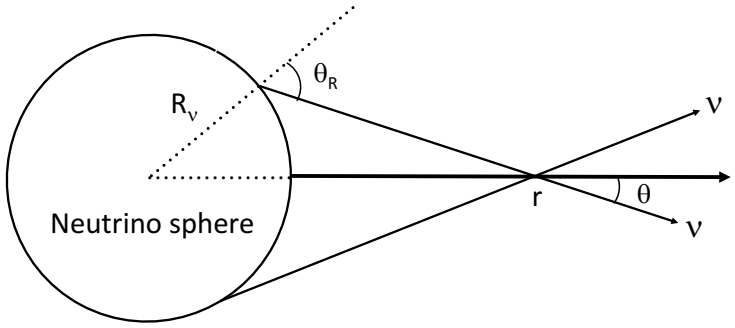

Figure 3.5: The geometry of neutrino emission in the bulb model [58]. The radius of neutrino sphere R_ν is independent of neutrino species. The scattering angle θ at radius r is related to the emission angle θ_R on the surface of neutrino sphere.

and neutrino self interactions:

$$\cos\theta_p \frac{\partial}{\partial r}\rho(r, E, \theta_p) = -i\left[\Omega(E) + V_{\rm MSW}(r) + V_{\rm self}(r, \theta_p),\ \rho(r, E, \theta_p)\right], \tag{3.30}$$

$$\cos\theta_p \frac{\partial}{\partial r}\bar{\rho}(r, E, \theta_p) = -i\left[-\Omega(E) + V_{\rm MSW}(r) + V_{\rm self}(r, \theta_p),\ \bar{\rho}(r, E, \theta_p)\right], \tag{3.31}$$

where $\Omega(E)$ is the vacuum Hamiltonian in Eq.(2.15) whose energy is E and $V_{\rm MSW}(r)$ represents the matter potential in Eq.(2.46) which is proportional to radial profile of electron number density $n_e(r)$. The scattering angle θ_p is included in Eqs.(3.30) and (3.31). In current status, neutrino transport considering such angular dependence is one of up-to-date treatments of non-linear flavor transitions. This calculation method is called the "multi-angle simulation" [58,61,64,70,72,73,80,82–84]. Numerical results shown in the next chapters are based on the three flavor multiangle simulations.

3.6 Demonstration of two flavor collective neutrino oscillations under the single angle approximation

To calculate neutrino oscillations precisely, Eqs.(3.30) and (3.31) should be solved in three flavors (ν_e, ν_μ, ν_τ). However, it is highly difficult to interpret phenomenology of such three flavor multiangle simulations. In this section, we discuss two flavor (ν_e, ν_x) collective neutrino oscillations under the single angle approximation [58,60,61] which eliminates the angular dependence in the bulb model. From this simple demonstration, we can abstract fundamental property of collective neutrino oscillations which is also confirmed in more complex three flavor multiangle simulations.

3.6.1 The single angle approximation

The equations of motion of neutrino oscillations in Eqs.(3.30) and (3.31) depend on the scattering angle θ_p (or emission angle $\theta_R(\theta_p, r)$). In the single angle approximation [58, 60, 61], the value of θ_p is fixed. Here, we impose $\theta_p = 0$ and remove the angular dependence in neutrino density matrices: $\rho(r, E, \theta_p) \mapsto \rho(r, E)$. Owing to this approximation, an angular integration is possible in Eq.(3.29), then the radial dependence apparently appears in the neutrino self interactions:

$$V_{\rm self}(r) = \frac{\sqrt{2}G_F}{2\pi R_\nu^2} D(R_\nu/r) \int {\rm d}q \sum_{\alpha={\rm all\ flavor}} \left\{ \frac{L_{\nu_\alpha}}{\langle E_{\nu_\alpha}\rangle} f_{\nu_\alpha}(q)\rho(r,q) - \frac{L_{\bar\nu_\alpha}}{\langle E_{\bar\nu_\alpha}\rangle} f_{\bar\nu_\alpha}(q)\bar\rho(r,q) \right\}, \tag{3.32}$$

$$D(x) = \frac{1}{2}\left(1 - \sqrt{1-x^2}\right)^2 \propto x^4 \ (x << 1). \tag{3.33}$$

The value of $D(R_\nu/r)$ changes from 1 ($r = R_\nu$) to 0 ($r = \infty$) during the neutrino propagation. The strength of neutrino self interactions decreases rapidly as r^{-4} for large radius. Therefore, in the cooling phase of the proto-neutron star, collective neutrino oscillations occur at $\sim O(100)$ km before the MSW resonances at $\sim O(1000)$ km.

3.6.2 Numerical setup

We set the radius of neutrino sphere as $R_\nu = 10$ km in the bulb model. We assume that energy distribution on the surface of neutrino sphere is Fermi-Dirac distribution without chemical potential. As shown in Ref. [61], the normalized neutrino spectra on the surface of the neutrino sphere are parameterized by neutrino temperature $T_i (i = \nu_e, \bar{\nu}_e, \nu_x)$:

$$f_i(E) = \frac{2\beta_i}{3\zeta_3} \frac{\beta_i E}{e^{\beta_i E} + 1}, \tag{3.34}$$

$$\int \mathrm{d}E \; f_i(E) = 1, \tag{3.35}$$

where $\zeta_3 \sim 1.202$ and $\beta_i = T_i^{-1}$. The mean energy is given by $\langle E_i \rangle = 3.15 \; T_i$. Table.3.1 displays the neutrino temperature, luminosity and mean energy we employ. Values of these parameters are typical ones in the cooling phase of the proto-neutron star. We assume that the spectra of ν_x and $\bar{\nu}_x$ are degenerate because neutrino energy is much smaller than the mass of $\mu^\pm$ and $\tau^\pm$ which are energy threshold of charged current reaction in flavors μ and τ. Initial neutrino spectra which are proportional to $L_i / \langle E_i \rangle f_i(E)$ are shown in Fig.3.6. On the surface of neutrino sphere, we ignore non-diagonal components in neutrino density matrices. Then, the initial condition of neutrino density matrices are given by below mixed states:

$$\rho_{ee}(R, E) = 1 - \rho_{xx}(R, E) = \frac{L_{\nu_e} \langle E_{\nu_e} \rangle f_{\nu_e}(E)}{L_{\nu_e} / \langle E_{\nu_e} \rangle f_{\nu_e}(E) + L_{\nu_x} / \langle E_{\nu_x} \rangle f_{\nu_x}(E)}, \tag{3.36}$$

$$\bar{\rho}_{ee}(R, E) = 1 - \bar{\rho}_{xx}(R, E) = \frac{L_{\bar{\nu}_e} \langle E_{\bar{\nu}_e} \rangle f_{\bar{\nu}_e}(E)}{L_{\bar{\nu}_e} / \langle E_{\bar{\nu}_e} \rangle f_{\bar{\nu}_e}(E) + L_{\nu_x} / \langle E_{\nu_x} \rangle f_{\nu_x}(E)}, \tag{3.37}$$

$$\rho_{ex}(R, E) = \rho_{xe}(R, E) = \bar{\rho}_{ex}(R, E) = \bar{\rho}_{xe}(R, E) = 0. \tag{3.38}$$

As neutrino mixing parameters in two flavor oscillations, we choose the neutrino mass difference $|\Delta m^2| = 2.4 \times 10^{-3} \mathrm{eV}^2 \sim |\Delta \mathrm{m}^2_{32}|$ and neutrino mixing angle $\theta = 0.15$ rad $\sim \theta_{13}$ which characterize the MSW H resonance in three flavor neutrino oscillations [71]. The sign of Δm^2 reflects the neutrino mass hierarchy in Fig.2.2. In general, neutrino oscillations inside medium are sensitive to the neutrino mass hierarchy. This statement is also true when neutrinos themselves are background. We mainly analyze the inverted mass hierarchy case ($\Delta m^2 < 0$) because fundamental

Table 3.1: The parameter set for initial neutrino distributions.

Species	$L_i(\times 10^{51}\mathrm{erg/s})$	$T_i(\mathrm{MeV})$	$\langle E_i \rangle(\mathrm{MeV})$
ν_e	1	3	9.5
$\bar{\nu}_e$	1	4	12.6
ν_x,$\bar{\nu}_x$	1	5	15.8

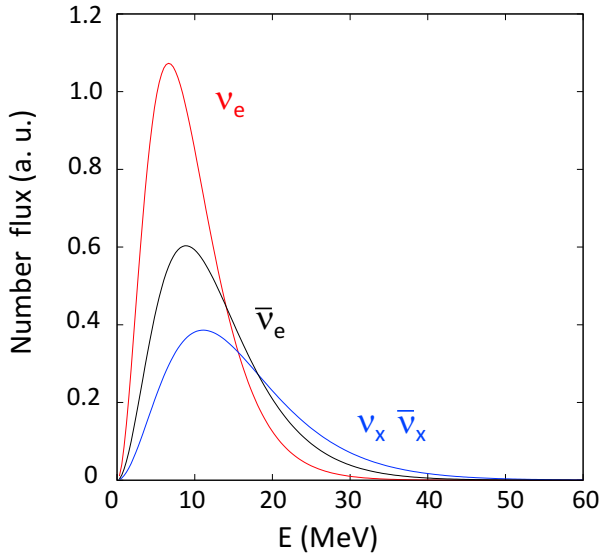

Figure 3.6: Initial neutrino spectra on the surface of neutrino sphere. The fluxes are normalized by some arbitrary unit.

property of collective neutrino oscillations is confirmed clearly in this mass ordering. After the discussion in inverted mass hierarchy, we briefly show the result in normal mass hierarchy.

3.6.3 Collective neutrino oscillations and spectral swap

We solve different energy of Eqs.(3.30) and (3.31), simultaneously from the neutrino sphere $R_\nu = 10$ km to 200 km under the single angle approximation. The non-linear potential is updated iteratively as flavor transitions proceed. Here, the matter potential $V_{\mathrm{MSW}}(r)$ is ignored for a simple discussion. As long as an electron background

density is much larger than the MSW resonance density, the same discussion can be possible by replacing the vacuum mixing angle with the effective small mixing angle [59, 62, 65].

The radial evolution of diagonal components: $\rho_{ee}(r, E)$ and $\bar{\rho}_{ee}(r, E)$ are shown in Fig.3.7. We pick up three representative values of neutrino energy from neutrino spectra in Fig.3.6. These diagonal components should be constant if there is no flavor transition. The value of each $\rho_{ee}(r, E)$ represents the number ratio of ν_e among all flavor of neutrinos whose energy is E at the radius r. One of the special features in Fig.3.7 is the collective flavor transitions irrespective of neutrino energy and species. Such non-linear flavor transitions are called "collective neutrino oscillations" [189]. Up to $\sim$ 50 km, all of neutrinos oscillate in the same frequency without changing the center of oscillations. Near the neutrino sphere, the strength of neutrino self interaction $V_{\rm self}(r)$ is much larger than that of vacuum potential $\Omega(E)$, then all of neutrinos change their flavors satisfying $[V_{\rm self}(r), \rho(r, E)] \sim 0$. Interestingly, the non-linear potential $V_{\rm self}(r)$ itself is oscillating in neutrino flavor space with some frequency $\omega_c(r)$. All of neutrinos follow the motion of $V_{\rm self}$, so that it looks like collective flavor transitions in the same frequency $\omega_c(r)$. In the intermediate region (50 km $<$ r $<$ 100 km), the center of flavor transitions change simultaneously in all energy of ν and $\bar{\nu}$. Such significant flavor mixing is caused by the growth of the non-diagonal component in the non-linear potential. The neutrino self interactions are comparable with vacuum Hamiltonian in this intermediate region, so that non-diagonal components in vacuum Hamiltonian becomes a large fluctuation for growth of $|V_{\rm self}(r)_{ex}|$. In the later phase ($r >$ 100 km), the neutrino interaction becomes weaker than the vacuum Hamiltonian, so that neutrino density matrices no longer follow the motion of $V_{\rm self}(r)$ actively and energy dependence clearly appears in flavor transitions. The bottom panel of Fig.3.7 indicates that all of antineutrino change their flavor completely after the collective neutrino oscillations. On the other hand, the value of 5 MeV in the top panel of Fig.3.7 eventually comes back to original value on the surface of neutrino sphere even though more energetic neutrino are transformed to other flavors. Finally, collective neutrino oscillations have finished around 200 km and flavor conversions of the emitting neutrinos settle down to equilibrium states.

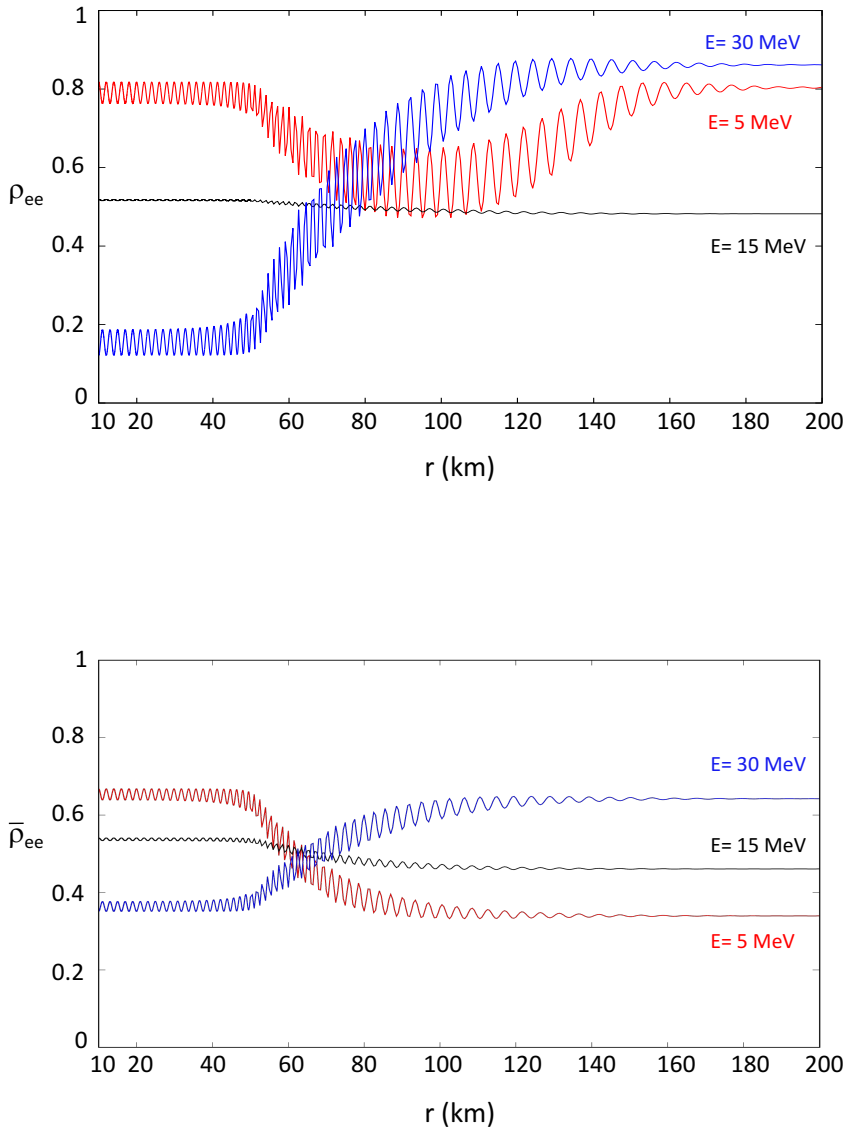

Figure 3.7: The upper (lower) panel represents the evolution of $\rho_{ee}(r, E)$ ($\bar{\rho}_{ee}(r, E)$) in collective neutrino oscillations. We select typical neutrino energy 5, 15 and 30 MeV outside the neutrino sphere. The initial values are given by Eqs.(3.36) and (3.37).

The neutrino spectra after the collective neutrino oscillations ($r = 200$ km) are shown in Figs.3.8 and 3.9. The implication found in Fig.3.7 is revealed. In the right panel of Fig.3.8, the sharp energy split is confirmed in $E = E_{\rm split} \sim 6$ MeV which is characterized by a static solution of self consistency equations [51, 62, 63]. There is no difference between the initial and final spectrum in low energy region ($E < E_{\rm split}$). However, dramatic spectrum exchange occurs in high energy region $E > E_{\rm split}$. The spectrum of ν_e at 200 km (red solid line) completely corresponds to that of ν_x at 10 km (the black dot line), and vice versa. Fig.3.9 shows that spectrum exchange occurs in all energy of antineutrinos, which is similar to the MSW resonance in inverted mass hierarchy. The collective neutrino oscillations and the spectral swap which are confirmed in this simple demonstration are fundamental phenomena in neutrino self interactions even though the coherence in collective motions are smeared out and the spectral split becomes less significant in precise three flavor multiangle calculation. In general, the spectral swap increases the mean energy of emitting electron type neutrinos because of the temperature hierarchy: $\langle E_{\nu_e} \rangle \leq \langle E_{\bar{\nu}_e} \rangle \leq \langle E_{\nu_X} \rangle$. The increased mean energy of ν_e and $\bar{\nu}_e$ would have serious influence on the neutrino detection and nucleosynthesis inside the core-collapse supernova because the cross sections of neutrino-induced charged current reactions are large in high energy neutrinos.

3.7 Geometrical representation in the Bloch space

It's impossible to solve collective neutrino oscillations analytically because of the non-linearity of the problem. However, numerical results shown in §3.6 can be interpreted as the MSW like level crossing in a co-rotating frame. The idea of going to a co-rotating frame is proposed in Ref. [58] and the value of the split energy E_c is estimated by the static solution of consistency equations in Refs. [51, 62, 63]. Here, we estimates value of the gamma factor in collective neutrino oscillations without solving consistent equations and shows that numerical results of collective neutrino oscillations can be regraded as adiabatic flavor transitions in a co-rotating frame. In this section, the geometrical representation of Bloch vector is introduced in neutrino

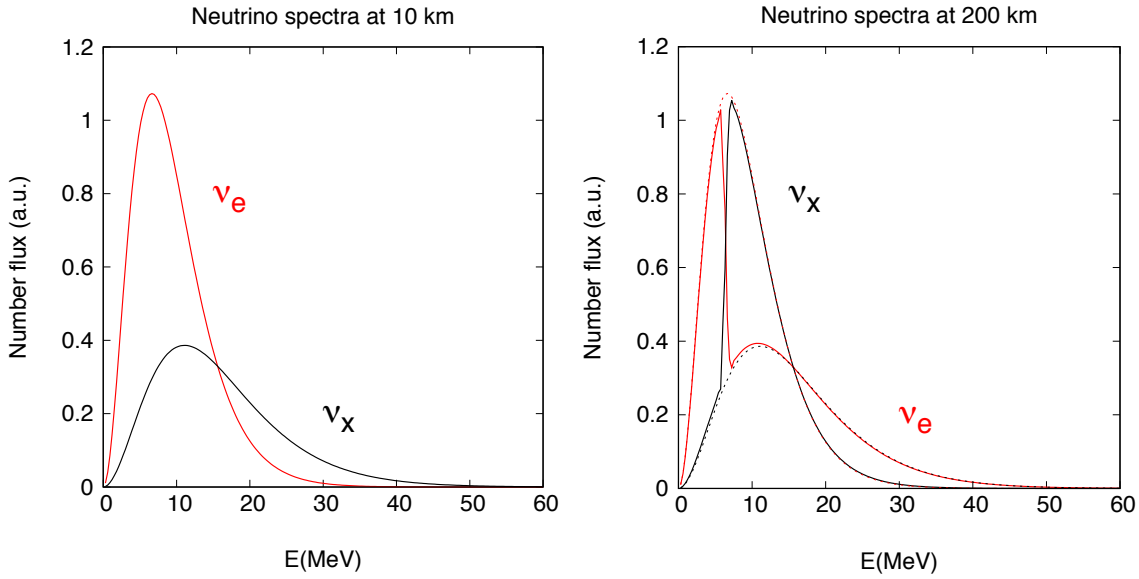

Figure 3.8: Neutrino spectra before (left panel) and after (right panel) the collective neutrino oscillations. The dot lines in the right panel represent the normalized neutrino spectra of the left panel. The solid red (black) line should corresponds to the dot red (black) one if any flavor transitions are negligible. The spectral swap occurs in high energy region $E > E_{\rm split} \sim 6$ MeV.

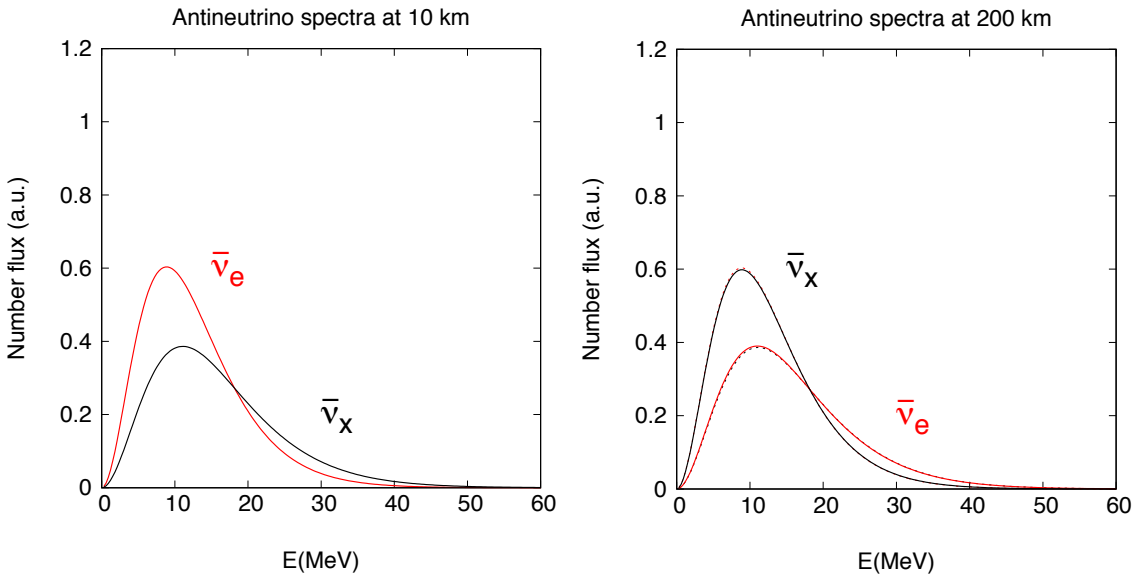

Figure 3.9: The spectra of antineutrino sector. There is no energy split and the spectral swap occurs in all energy antineutrinos.

flavor space, which replaces evolution of neutrino oscillations with the motion of Bloch vectors on the surface of Bloch sphere. In §3.8, we check whether collective neutrino oscillations are regarded as the adiabatic flavor transitions in a co-rotating frame.

In general, 2×2 Hermite matrix A is extend by Pauli matrices $\{\sigma_i\}_{i=x,y,z}$:

$$A = \frac{\mathrm{trA}}{2} I_{2\times 2} + \frac{a_i \sigma_i}{2}, \tag{3.39}$$

$$I_{2\times 2} = \begin{pmatrix} 1 & 0 \\ 0 & 1 \end{pmatrix}, \sigma_x = \begin{pmatrix} 0 & 1 \\ 1 & 0 \end{pmatrix}, \ \sigma_y = \begin{pmatrix} 0 & -i \\ i & 0 \end{pmatrix}, \ \sigma_z = \begin{pmatrix} 1 & 0 \\ 0 & -1 \end{pmatrix}, \tag{3.40}$$

where $\mathbf{a} = (a_x, a_y, a_z)$ is a real vector. Density matrices of both neutrino and antineutrino are Hermite matrices, so that the decomposition of Eq.(3.39) is possible:

$$\rho(r, E) = \frac{1}{2} I_{2\times 2} + \frac{\mathbf{P} \cdot \vec{\sigma}}{2}, \tag{3.41}$$

$$\bar{\rho}(r, E) = \frac{1}{2} I_{2\times 2} + \frac{\bar{\mathbf{P}} \cdot \vec{\sigma}}{2}, \tag{3.42}$$

where $\mathbf{P}(\bar{\mathbf{P}})$ is called a "polarization vector" or "Bloch vector" [61, 189–191]. Eigenvalues of a neutrino density matrix is conserved through the unitary transformation, so that the length of polarization vector is invariant in neutrino oscillations if there are no collisions. Fig.3.10 shows the picture of a polarization vector on the surface of the Bloch sphere whose radius is $|\mathbf{P}|(|\bar{\mathbf{P}}|)$. The projection of $\mathbf{P}$ onto the z axis represents the number of neutrinos because σ_z has diagonal components. On the other hand, amplitude of interference between two flavor neutrinos is described by the projection of $\mathbf{P}$ onto the $x - y$ plane. This geometrical representation is frequently employed to represent quantum states of a two-level system.

The time evolution of neutrino density matrices is equivalent to the motion of polarization vectors on the surface of Bloch sphere. The time evolution of i component of $\mathbf{P}$ is derived from $\mathrm{tr_F}[\dot{\rho}\sigma_i]$. Then, the Bloch equations of neutrino polarization vectors are given by

$$\frac{\mathrm{d}}{\mathrm{d}r}\mathbf{P} = (\omega\mathbf{B} + \mu\mathbf{D}) \times \mathbf{P}, \tag{3.43}$$

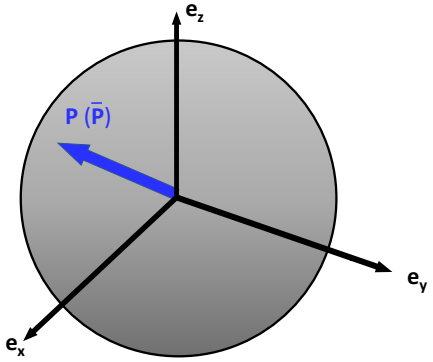

Figure 3.10: The schematic picture of the polarization vector $\mathbf{P}(\bar{\mathbf{P}})$ on the surface of the Bloch sphere. $\mathbf{e}_i (i = x, y, z)$ represents the unit vector of $i-$axis.

$$\frac{\mathrm{d}}{\mathrm{d}r}\bar{\mathbf{P}} = (-\omega\mathbf{B} + \mu\mathbf{D}) \times \bar{\mathbf{P}}, \tag{3.44}$$

where the first and second terms of the right hand sides in above equations represent the polarization vectors of vacuum Hamiltonian in Eq.(2.24) and neutrino self interactions in Eq.(3.32), respectively [61, 189]. The first term is described by

$$\omega = \frac{\Delta m^2}{2E}, \tag{3.45}$$

$$\mathbf{B} = (\sin 2\theta, 0, -\cos 2\theta)_{\mathrm{flavor}} = (0, 0, -1)_{\mathrm{mass}}, \tag{3.46}$$

where ω is a vacuum frequency and the components of unit vector $\mathbf{B}$ are shown in both flavor and mass bases [51]. If neutrino self interactions are negligible, Eqs.(3.43) and (3.44) show the precession of polarization vectors around the vacuum vector $\mathbf{B}$ with the vacuum frequency ω, which is similar to Larmor precession of a magnetic moment inside an external magnetic field. The vacuum neutrino oscillations discussed in §2.3 are shown visually in Fig.3.11. At first, only an electron type neutrino exists, so that the polarization vector is parallel to the z axis in the flavor space: $P_z = |P| = 1$. The polarization vector precesses around the vacuum vector without changing the length $|P|$. The oscillation frequency is $|\omega|$ and P_z takes the value in $[\cos 4\theta, 1]$. The survival probability of ν_e is obtained by $\rho_{ee} = 1/2 + P_z/2$. The oscillation length in Eq.(2.30) corresponds to $l_{\mathrm{osc}} = 2\pi/\omega$.

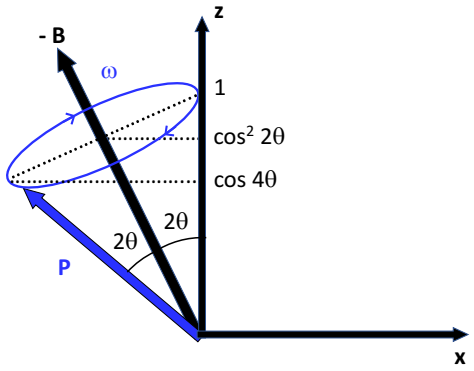

Figure 3.11: The geometrical representation of vacuum neutrino oscillations in §2.3. The polarization vector **P** is rotating around the vacuum vector **B** with frequency $\omega > 0$. The directions **x** and **z** represent x and z axis in the flavor basis, respectively.

The second term of the right hand side in Eq.(3.43) is given by

$$\mu = \sqrt{2} G_F (n^0_\nu + n^0_{\bar{\nu}}) D(R_\nu / r), \tag{3.47}$$

$$\mathbf{D} = \frac{1}{n^0_\nu + n^0_{\bar{\nu}}} \int \mathrm{d}q \; \frac{1}{2\pi R^2_\nu} \sum_{\alpha=\text{all flavor}} \left\{ \frac{L_{\nu_\alpha}}{\langle E_{\nu_\alpha} \rangle} f_{\nu_\alpha}(q) \mathbf{P} - \frac{L_{\bar{\nu}_\alpha}}{\langle E_{\bar{\nu}_\alpha} \rangle} f_{\bar{\nu}_\alpha}(q) \bar{\mathbf{P}} \right\}, \tag{3.48}$$

$$n^0_\nu = \frac{1}{\pi R^2_\nu} \sum_{\alpha=\text{all flavor}} \frac{L_{\nu_\alpha}}{\langle E_{\nu_\alpha} \rangle}, \tag{3.49}$$

$$n^0_{\bar{\nu}} = \frac{1}{\pi R^2_\nu} \sum_{\alpha=\text{all flavor}} \frac{L_{\bar{\nu}_\alpha}}{\langle E_{\bar{\nu}_\alpha} \rangle}, \tag{3.50}$$

where μ represents the strength of neutrino self interaction at radius r. Eqs.(3.49) and (3.50) are number density of all flavor of neutrinos and antineutrinos on the surface of neutrino sphere, respectively. One of the benefits of the single angle approximation is the separation of the oscillation frequency μ and normalization vector **D**. Fig.3.12 shows the precession of the polarization vector **P** around both the vacuum vector **B** and the vector of neutrino self interactions **D**. The equation of motion of **D** is written as

$$\frac{\mathrm{d}}{\mathrm{d}r}\mathbf{D} = \mathbf{B} \times \mathbf{S} = \omega_c \mathbf{B} \times \mathbf{D} + \kappa \mathbf{B} \times (\mathbf{B} \times \mathbf{D}), \tag{3.51}$$

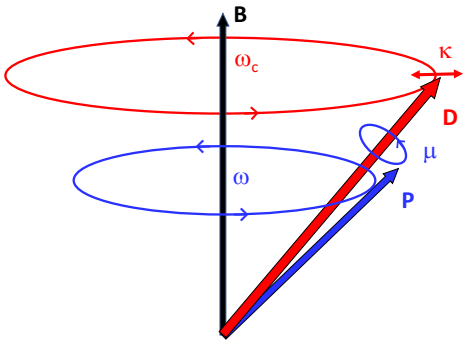

Figure 3.12: The dynamics of **P** and **D** following Eqs.(3.43) and (3.51). The inner product $D_{\parallel} = \mathbf{B}\cdot\mathbf{D}$ is constant, so that **D** rotate on the same plane perpendicular to **B**. The precession frequency of **D** is ω_c. The length of **D** is governed by κ as shown in Eq.(3.54). Each polarization vector **P** follows the motion of **D**. The strength of neutrino self interactions μ corresponds to oscillation frequency of **P** around **D**.

$$\mathbf{S} = \frac{1}{n^0_\nu + n^0_{\bar\nu}} \int \mathrm{d}q \; \frac{1}{2\pi R^2_\nu} \frac{\Delta m^2}{2q} \sum_{\alpha=\text{all flavor}} \left\{ \frac{L_{\nu_\alpha}}{\langle E_{\nu_\alpha}\rangle} f_{\nu_\alpha}(q)\mathbf{P} + \frac{L_{\bar\nu_\alpha}}{\langle E_{\bar\nu_\alpha}\rangle} f_{\bar\nu_\alpha}(q)\bar{\mathbf{P}} \right\} \tag{3.52}$$

where ω_c represents the precession frequency around **B** (see Fig.3.12). From the inner product in Eq.(3.51), we find a conserved quantity:

$$D_{\parallel} = \mathbf{B}\cdot\mathbf{D} = \text{const.} = -\cos 2\theta \frac{\frac{L_{\nu_e}}{\langle E_{\nu_e}\rangle} - \frac{L_{\bar\nu_e}}{\langle E_{\bar\nu_e}\rangle}}{\frac{L_{\nu_e}}{\langle E_{\nu_e}\rangle} + \frac{L_{\bar\nu_e}}{\langle E_{\bar\nu_e}\rangle} + 2\frac{L_{\nu_x}}{\langle E_{\nu_x}\rangle}}, \tag{3.53}$$

which indicates that the tip of **D** stays on the same plane perpendicular to **B**. The time evolution of perpendicular component $D_\perp = \sqrt{|D|^2 - |D|^2_{\parallel}}$ is characterized by κ in Eq.(3.51):

$$\frac{\mathrm{d}}{\mathrm{d}r}|D_\perp| = -\kappa |D_\perp|, \tag{3.54}$$

where the positive (negative) sign of κ represents the inward (outward) spiral motion of **D**, respectively. The values of ω_c and κ are obtained dynamically through collective neutrino oscillations. The non-linear phenomena of collective neutrino oscillations would be analyzed by the comparison between μ and ω of typical neutrino energy. In our demonstration, near the neutrino sphere, neutrino self interactions are much

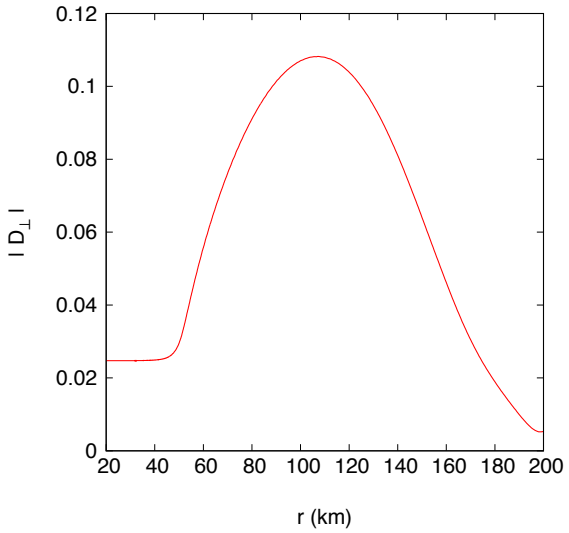

Figure 3.13: The evolution of $|D_\perp|$ in §3.6.

stronger than the vacuum Hamiltonian: $\mu >> |\omega|$, which results in the synchronization of polarization vectors [60,61] whose oscillation frequency is ω_c. The evolution of $|D_\perp|$ is shown in Fig.3.13. $|D_\perp|$ is constant ($\kappa = 0$) during the synchronization. The synchronized motion is gradually violated when μ decreases down to $|\omega|$. The finite κ appears around 50 km which corresponds to the onset of significant flavor transitions in Fig.3.7. The negative κ causes the outward spiral motion of $\mathbf{D}$ which induces flavor mixing of following polarization vectors. The perpendicular component $|D_\perp|$ becomes maximum around 105 km. After such maximum point, κ remains positive. Then, each polarization vector $\mathbf{P}$ follows the inward spiral motion of $\mathbf{D}$ but energy dependence appears in non-linear flavor transitiosn because the vacuum Hamiltonian gradually overcomes the self interactions. Polarization vectors are finally parallel or antiparallel to the direction of $\mathbf{B}$ after collective neutrino oscillations ($\mu << |\omega|$). If $\mathbf{P}$ changes the original direction towards $\mathbf{B}$ after collective neutrino oscillations, spectral swap occurs in such energy of neutrinos.

3.8 Adiabatic flavor transitions in a co-rotating frame

The precession frequency ω_c can explain the split energy $E_{\rm split}$ in the right panel of Fig.3.8 if MSW like level crossing occurs adiabatically in a co-rotating frame. For convenience, we describe components of matrices in vacuum mass basis where the z direction is antiparallel to $\mathbf{B}$. In this mass basis, the Hamiltonian of neutrinos is written as

$$\begin{aligned} H &= \omega\frac{\mathbf{B}\cdot\vec{\sigma}}{2} + \mu\frac{\mathbf{D}\cdot\vec{\sigma}}{2} \\ &= \begin{pmatrix} -\omega - \mu D_{\parallel} & \mu|D_{\perp}|e^{-i\alpha} \\ \mu|D_{\perp}|e^{i\alpha} & \omega + \mu D_{\parallel} \end{pmatrix}_{\rm mass} \end{aligned} \tag{3.55}$$

where ω is the vacuum frequency and the phase α is defined by $\alpha = \tan^{-1}(D_y/D_x)$. The phase α is a time dependent variable because $\mathbf{D}$ precesses around $\mathbf{B}$ as shown in Fig.3.12. Here, we introduce a co-rotaing frame which moves together with $\mathbf{D}$ [58]. We employ the unitary transformation from the mass basis to the co-rotating frame:

$$U_{\rm r} = \exp(-\frac{i\alpha}{2}\sigma_z), \tag{3.56}$$

which eliminates phase α in $U_r^{\dagger}HU_r$. In analogy with Eq.(2.73), the Hamiltonian in the co-rotating frame is given by

$$H' = U_{\rm r}^{\dagger}HU_{\rm r} - iU_r^{\dagger}\frac{{\rm dU_r}}{{\rm dr}} = \begin{pmatrix} -\omega + \omega_c - \mu D_{\parallel} & \mu|D_{\perp}| \\ \mu|D_{\perp}| & \omega - \omega_c + \mu D_{\parallel} \end{pmatrix}_{\rm mass} \tag{3.57}$$

where the contribution from precession of $\mathbf{D}$ is included in the frequency $\omega_c = -{\rm d}\alpha/{\rm dr}$. In the co-rotating frame, the Hamiltonian has only z and x components, so that we can consider the MSW like level crossing in this frame. As discussed in §2.7, the level crossing occurs when the diagonal component disappears:

$$\omega = \omega_{cr} = \omega_c - \mu D_{\parallel}. \tag{3.58}$$

Such adiabatic level crossing in the co-rotating frame can be regarded as the rapid adiabatic passage (RAP) [192]. The diagonal component in Eq.(3.57) would correspond to a detuning parameter in Rabi oscillations [192].

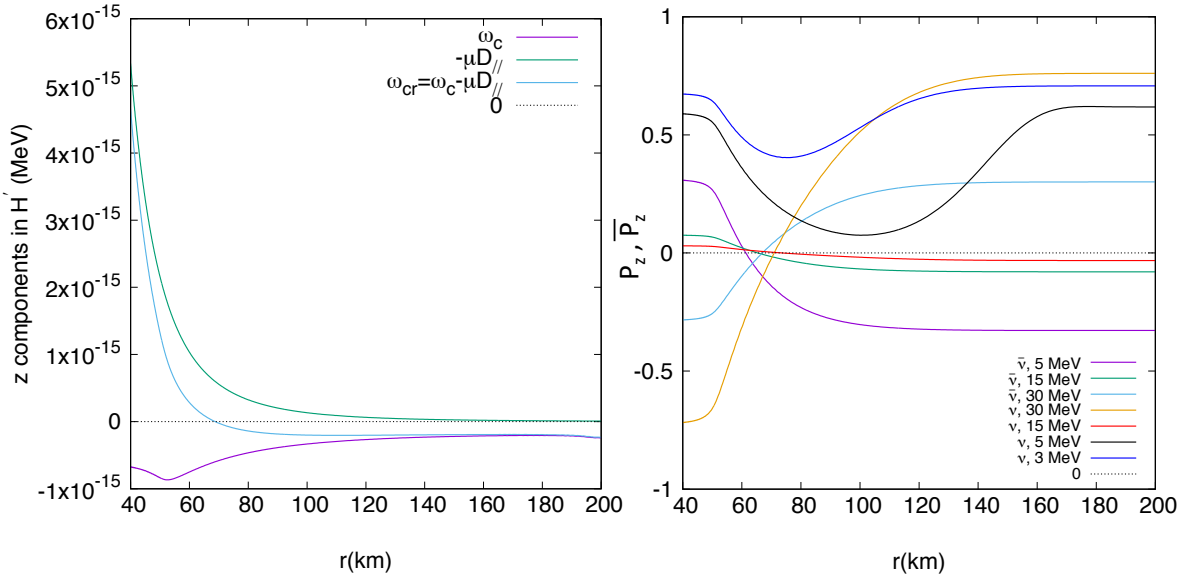

Figure 3.14: The left panel represents the evolution of diagonal components in Eq.(3.57). The right panel shows evolution of P_z and $\bar{P}_z$ where the z axis corresponds to direction of $-\mathbf{B}$.

The left panel of Fig.3.14 shows the evolution of ω_{cr}, ω_c and $-\mu D_{\parallel}$ in our demonstration. The value of precession frequency ω_c is obtained numerically by

$$\omega_c = \frac{\mathbf{D}\cdot\mathbf{S} - (\mathbf{D}\cdot\mathbf{B})(\mathbf{S}\cdot\mathbf{B})}{|D_{\perp}|^2}. \tag{3.59}$$

Near the neutrino sphere ($r \sim 40$ km), the value of ω_{cr} becomes positive because of large $\mu(>> \omega_c)$ and the negative sign of $D_{\parallel}$ in our demonstration. In case of inverted mass hierarchy, the resonance condition in Eq.(3.58) is satisfied with negative energy neutrinos. From Eqs.(3.44) and (3.45), the negative energy neutrino is equivalent to a positive energy antineutrino. Therefore, level crossing occurs from low energy to high energy antineutrinos as the value of μ becomes small. The value of ω_{cr}

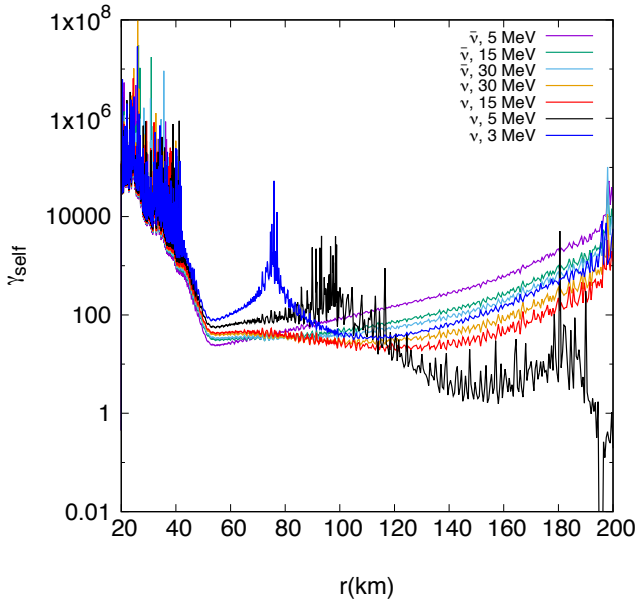

Figure 3.15: The evolution of adiabatic parameter in collective neutrino oscillations. The flavor transition becomes adiabatic when $\gamma_{\rm self} >> 1$ is satisfied.

continues to decrease and becomes negative at $r > 70$ km. Then, the level crossing also starts in the neutrino sector from high energy to low energy region. Actually, such resonance phenomena are confirmed in our demonstration as shown in the right panel of Fig.3.14. The level crossing occurs when the value of P_z becomes zero. The level crossing does not happen in 3 and 5 MeV neutrinos because ω_{cr} is always larger than ω of these energies. After the collective neutrino oscillations, ω_{cr} settles down to equilibrium $\sim -2.1 \times 10^{-16}$ MeV which reproduces the value of energy split in the right panel of Fig.3.8: $E_{\rm split} = 2\omega_{cr}/\Delta m^2 \sim 6.2$ MeV. We confirm that collective neutrino oscillations in our demonstration look like adiabatic in a co-rotating frame. In analogy with Eq.(2.70), the condition of adiabatic flavor transition is written as

$$\gamma_{\rm self} = \frac{\{(-\omega+\omega_{cr})^2 + (\mu D_\perp)^2\}^{3/2}}{2|\ (-\omega+\omega_{cr})\frac{\rm d}{{\rm d}r}(\mu|D_\perp|) - \mu|D_\perp|\frac{{\rm d}\omega_{cr}}{{\rm d}r}\ |} >> 1, \tag{3.60}$$

where $\gamma_{\rm self}$ is the gamma factor in collective neutrino oscillations. An equivalent adiabatic condition is also derived in Ref. [63]. Fig.3.15 represent the evolution of $\gamma_{\rm self}$. It seems that adiabatic condition is well satisfied except for 5 MeV neutrino. Especially, the increasing $|D_\perp|$ at $r \sim 50$ km prevents violation of adiabaticity. The split energy $E_{\rm split}$ is close to 5 MeV, so that the gamma factor of 5 MeV neutrinos tends to be small because of cancellation $(-\omega + \omega_{cr})^2$ in the numerator of Eq.(3.60). The sharp peak appears in 3 MeV neutrino at $r \sim 75$ km which reflects the small denominator in Eq.(3.60). Such peak structure is not found in antineutrinos and more energetic neutrinos because of the small value of $-\omega + \omega_{cr}$.

In our demonstration, we only focus on collective neutrino oscillations in inverted mass hierarchy ($\Delta m^2 < 0$). However, the same analytic discussion is possible in normal mass hierarchy ($\Delta m^2 > 0$) if non-linear flavor transitions occur adiabatically. In normal mass hierarchy, the sign of vacuum frequency ω becomes positive (negative) in neutrino (antineutrino) sector, respectively. Therefore, the level crossing occurs from low energy to high energy neutrinos. The sign of ω_c is also positive in normal mass hierarchy, so that there is no spectral swap in antineutrino spectra. Fig.3.16 shows the neutrino spectra after collective neutrino oscillations, which reflects the above picture of adiabatic flavor transition in the co-rotating frame. The spectral split appears in 1.2 MeV in the neutrino sector. Such flavor transitions have almost negligible in the detection of supernova neutrinos.

We should keep in mind that there is a limitation of above adiabatic flavor transitions. Spectra swap in high energy region appears even in normal mass hierarchy depending on the value of initial neutrino spectra: $\Phi^0 = L_i/\langle E_i \rangle$ [67,71]. Furthermore, in inverted mass hierarchy, multispectral splits are obtained in such initial neutrino fluxes. The mechanism of multispectral swap is still unknown even though Ref. [67] suggests that the crossing of initial spectra of different flavors are related to the stability of multispectral swap. The multispectral splits can not be explained by the picture of adiabatic flavor transitions we discuss. In case of violation of adiabaticity, a large $|\kappa|$ in Eq.(3.54) induces the significant nutation motion of $\mathbf{D}$ which overcomes precession motion of $\mathbf{D}$ around $\mathbf{B}$. Small asymmetry among initial neutrino fluxes is

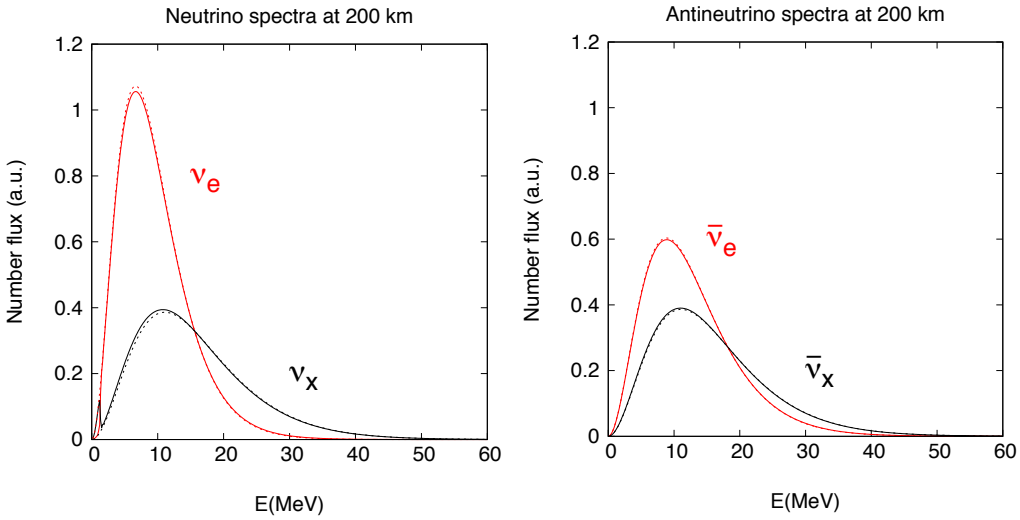

Figure 3.16: The solid lines show the neutrino spectra after collective neutrino oscillations ($r = 200$ km) in normal mass hierarcy. The dot lines corresponds to the normalized spectra on the surface of neutrino sphere. There is no difference between solid and dot lines in the antineutrino spectra. On the other hand, spectral swap occur in low energy neutrinos $E < E_{\rm split} = 1.2$ MeV.

favorable for such dominant nutation of **D** [60, 64, 67, 71, 72]. Here, we only discuss behavior of collective neutrino oscillations in two flavor single angle calculation. The situation becomes more complex in more realistic calculation method of neutrino oscillations. However, fundamental properties such as collective non-linear motion and spectra swap are also common even in more updated neutrino transport. From the next chapter, we show numerical results of three flavor multiangle simulations.

Chapter 4

Detectability of collective neutrino oscillations in electron capture supernovae

There is no observational evidence of collective neutrino oscillations even though such non-linear flavor transitions are predicted theoretically. The extensive studies of collective neutrino oscillations are provided by Ref. [80] where $18M_{\odot}$ progenitor is employed. The expected neutrino event rate at Super-Kamiokande (SK) and DUNE are computed. However, collective neutrino oscillations are fragile in such $18M_{\odot}$ progenitor model because of the large multiangle matter suppression. More light mass progenitor is preferable for the detection of collective neutrino oscillations. In this chapter, we show numerical results of three flavor multiangle calculations in electron capture supernovae whose progenitor mass is $8.8M_{\odot}$. Then, we discuss how traces of collective neutrino oscillations can be observed in future neutrino detectors such as Hyper-Kamioknade (HK), JUNO and DUNE. The content of Ref. [84] is reviewed focusing on my contributions: three flavor multiangle simulations and analysis in neutrino detectors.

4.1 Numerical setup

Neutrino oscillations are calculated as post processes by using time snapshots obtained by hydrodynamic simulations. We employ the $8.8M_{\odot}$ progenitor model of electron capture supernovae [118, 119, 129]. The numerical setup of the envelope is the same as that of Ref. [120]. The dilute envelope structure of electron capture supernovae prevents the multiangle matter suppression [65] (see §4.2), which results in significant signature of collective neutrino oscillations. The hydrodynamic simulation was carried out by 3DnSNe code (see the references [82, 145, 151, 186, 193–195] for recent application of this code). The models are computed on 1 dimensional spherical polar coordinate grid. The equation of state used in the simulation is the Lattimer and Swesty with incomprehensibility of $K = 220$ MeV [196].

The dynamics of the supernova explosion is characterized by the shock wave. In our model, the shock revives quite early by neutrino heating. The black curve of Fig.4.1 shows the evolution of the averaged shock radius. The shock revival time is 90 ms after bounce. We adopt the widely used convention of shock revival time defined as the time when the shock reaches 400 km [197]. This early shock revival time is due to the low mass accretion rate of this progenitor which has a very diluted envelop (see Fig.2 of Ref. [198]). After the shock revival, the shock continuously expands and reaches 1000 km at 120 ms after bounce. This result agrees with previous works (e.g.Fig 3 of Ref. [199]). It should be noted that shock revival happens even in 1D explosion model.

After the shock revival, the baryon density of the shocked region decreases. The color map of Fig.4.1 shows the logarithmic baryon density as a function of time and radius. As shown in §4.2, the region above 200 km is important for collective neutrino oscillations in this model. Before 50 ms post bounce, the density in such region is high and exceeds 10^9 g/cm^3. During this phase, the density gradually decreases with time due to the reduction of the mass accretion rate. After the shock revival around 90 ms post bounce, the density briefly increases as a function of time since mass is ejected from the central region. During this epoch, the density reaches $\sim 10^{7-8}$ g/cm^3 above 200 km. After 200 ms post bounce, the density decreases due to the reduction

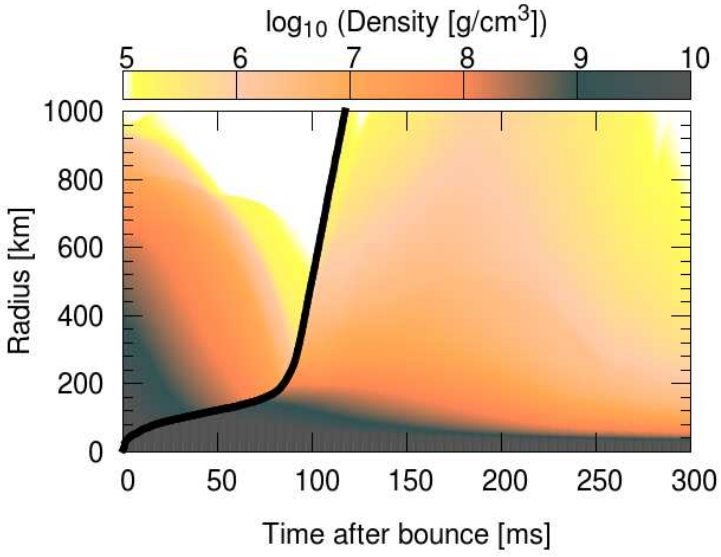

Figure 4.1: Black Curve: Time evolution of Shock Radius. Color: Time evolution of logarithmic baryon density profile [g/cm^3]. The horizontal axis is the time after bounce in ms and the vertical axis is the radial coordinates in km.

of mass ejection from the central region.

The information of neutrino spectra is necessary for the input of the simulation of collective neutrino oscillations. The evolutions of the neutrino luminosities and energies are shown in Fig.4.1. The green, red and blue curves correspond to ν_e, $\bar{\nu}_e$ and $\nu_X = (\nu_\mu, \nu_\tau, \bar{\nu}_\mu, \bar{\nu}_\tau)$, respectively. In the top panel, the luminosities after 150 ms post bounce are not so deviated from that of Ref. [74]. Before 150 ms, our luminosities are higher than that of Ref. [74] since an updated set of neutrino opacities is used (see Fig.15 of Ref. [193]). In our model, the luminosity of anti-electron neutrino is larger than that of electron type neutrino. This feature is not prominent in previous works (see Fig.1 of Ref. [74] and the hydrodynamic model of Ref. [200] for the detail of the setting). Our feature may originate from the employment of weak magnetism [201, 202] that is not used in previous works. The weak magnetism decreases the opacity for the anti-electron neutrino making them easier to escape. This would enlarge the antineutrino luminosity. In the middle panel, the hierarchy of the average energy is consistent with other simulations during the accretion phase:

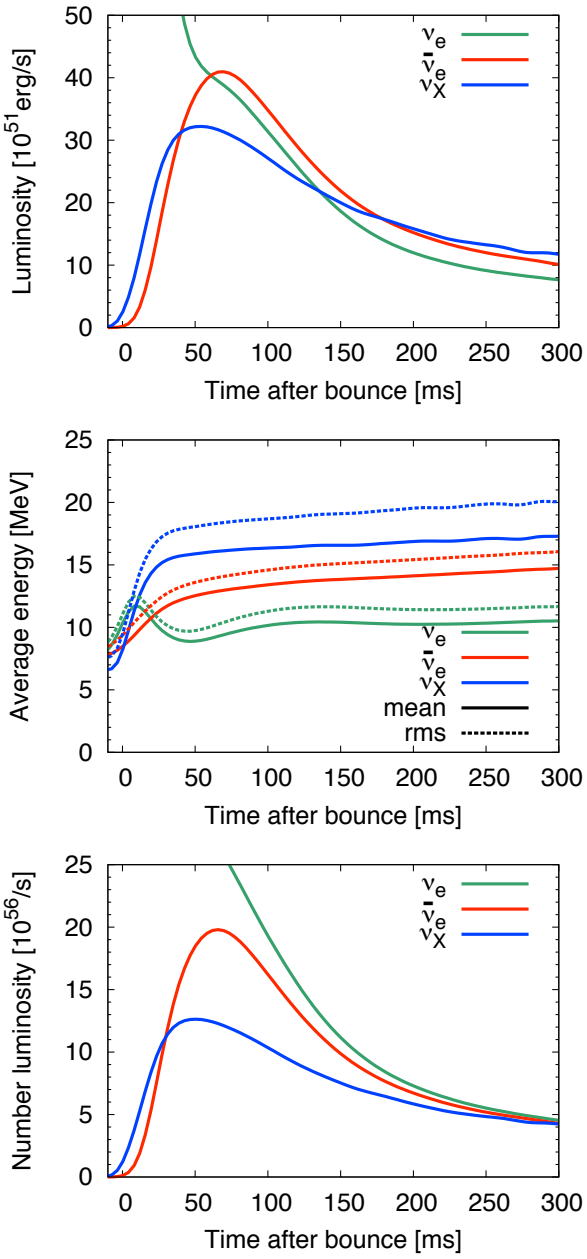

Figure 4.2: Time evolution of neutrino luminosity (top panel), neutrino average energy (middle panel), and neutrino number luminosity (bottom panel). In all, the green, red, and blue curves correspond to ν_e, $\bar{\nu}_e$ and $\nu_X = (\nu_\mu, \nu_\tau, \bar{\nu}_\mu, \bar{\nu}_\tau)$, respectively. In the middle panel, the solid line denotes the mean energy and the dotted line shows the root mean square (rms) energy. We evaluate the luminosities and energies at 500 km.

$\nu_X > \bar{\nu}_e > \nu_e$. The average energy is also higher compared to that of Ref. [74] due to the new reaction set (see Fig.15 of Ref. [193] again). The hierarchy of number luminosity has an interesting feature. In the bottom panel of Fig.4.1, the number luminosity is shown and initially the hierarchy is $\nu_X < \bar{\nu}_e < \nu_e$, which is typical in the accretion phase of core-collapse supernovae. However, at 300 ms post bounce, all number luminosities converge and there is no hierarchy. This feature leads to three flavor mixing as discussed in next sections.

The demonstration held in §3.6 is useful to abstract properties of neutrino self interactions such as non-linear flavor conversions and subsequent spectra swap inside core-collapse supernovae. However, the neutrino transport used in §3.6 is not enough for precise estimation of neutrino spectra because neutrinos have three flavors and multiangle effects are removed in the single angle approximation. In this chapter, we carry out three flavor multiangle simulations by solving Eqs.(3.30) and (3.31), which gives us more reliable neutrino spectra after collective neutrino oscillations. We take following neutrino mixing parameters: $\sin^2(2\theta_{12}) = 0.84$, $\sin^2(2\theta_{23}) = 1$, $\sin^2(2\theta_{13}) = 0.19$, $\Delta m^2_{21} = 7.9 \times 10^{-5}$ eV^2, $|\Delta m^2_{32}| = 2.0 \times 10^{-3}$ eV^2 and $\delta_{\rm CP} = 0$. The radius of neutrino sphere is set to $R_\nu = 30$ km which is close to sharp declines in the baryon density profiles. The neutrino spectra on the surface of neutrino sphere often show pinched spectra [203,204] compared to non-degenerate Fermi-Dirac distributions. We impose initial normalized neutrino spectrum $f_i(E)$ ($i = \nu_e, \bar{\nu}_e, \nu_X$) [205] at $r = R_\nu$ which satisfies Eq.(3.35)

$$f_i(E) = \frac{E^{\gamma_i}}{\Gamma(\gamma_i + 1)} \left(\frac{\gamma_i + 1}{\langle E_i \rangle} \right)^{\gamma_i + 1} \exp\left[-\frac{(\gamma_i + 1)E}{\langle E_i \rangle} \right], \tag{4.1}$$

with,

$$\gamma_i = \frac{\langle E_i^2 \rangle - 2\langle E_i \rangle^2}{\langle E_i \rangle^2 - \langle E_i^2 \rangle}, \tag{4.2}$$

where the $\Gamma(x)$ is a gamma function and the γ_i is a pinching parameter (the symbol α is often used in other works [203–205]). The pinching parameter γ_i is given by neutrino mean energies $\langle E_i \rangle$ and root mean square (rms) of neutrino energies $\sqrt{\langle E_i^2 \rangle}$ as shown

in the middle panel of Fig.4.1. Neutrino luminosities in the top panel of Fig.4.1 determine the strength of neutrino self interactions on the surface of neutrino sphere. The multiangle calculations are carried out up to 1500 km where collective neutrino oscillations have already finished. The matter potential: $V_{\rm MSW}(r) = \sqrt{2}G_F n_e(r)\,{\rm diag}(1,0,0)$ is obtained by profiles of baryon density and electron fraction Y_e at the corresponding times. In our simulation, MSW resonances do not appear in $E > 3$ MeV within 1500 km because of high electron number density. Neutrino spectra on the earth is derived by assuming adiabatic flavor transitions at MSW resonances [80]. The validity of such analytical treatment at MSW resonances is discussed in §4.3.

4.2 Results

Numerical results of three flavor multiangle simulations and subsequent MSW effects are shown in §4.2.1−§4.2.5. The detectability of collective neutrino oscillations in HK, JUNO and DUNE are discussed in §4.2.6−§4.2.8.

4.2.1 Spectral swap in different time snapshots

Three flavor multiangle calculations are carried out by using several time snapshots of hydrodynamic simulations in both normal hierarchy ($\Delta m^2_{32} > 0$) and inverted mass hierarchy ($\Delta m^2_{32} < 0$). Fig.4.3 shows survival probabilities of $\bar{\nu}_e$ at 1500 km in different time snapshots. The definition of such survival probability is given by $P(\bar{\nu}_e \to \bar{\nu}_e)$ in Eq.(4.5). Collective neutrino oscillations and MSW effects are almost separated in our progenitor model, so that survival probabilities in Fig.4.3 reflect contributions from collective neutrino oscillations solely. The top (bottom) panel corresponds to the case in inverted (normal) mass hierarchy, respectively. We find spectral swap in both mass hierarchy, but the mechanism of non-linear flavor transitions are different (see §4.2.2 and 4.2.3). Fig.4.4 shows the survival probabilities of ν_e at 1500 km. The values of such survival probabilities follow a similar pattern as Fig.4.3 in high energy region. In general, collective neutrino oscillations are suppressed in a dense region because of the large matter potential. The survival probabilities are almost unity at 31 ms post bounce, so that collective neutrino oscillations are highly suppressed.

Dense falling material above the shock wave (> 200 km) prevents flavor transitions. At 81 ms after core bounce, large flavor transitions occurs and the value of survival probabilities decrease down to 0.2 in both mass hierarchies. The dilute envelop of electron capture supernova enables the active nonlinear flavor transitions outside the shock wave. Around 200 ms, the matter density outside the neutrino sphere becomes slightly higher due to the shocked matter ejected from the center, which results in large multiangle matter suppression [65]. Especially, flavor transitions in normal mass hierarchy are easily affected by such matter suppression as shown in the bottom panels of Figs.4.3 and 4.4. This comes from the different mechanism of flavor transitions depending on neutrino mass hierarchy. After 300 ms, values of survival probabilities of both $\bar{\nu}_e$ and ν_e are close to 0.33 in high energy region, which implies active three flavor conversions because of decreasing matter density and small asymmetry among different neutrino fluxes: $\Phi_i^0 \propto L_i/\langle E_i \rangle (i = \nu_e, \bar{\nu}_e, \nu_X)$ as shown in the bottom panel of Fig.4.1.

4.2.2 Three flavor oscillations in inverted mass hierarchy

Instead of usual flavor basis $e - \mu - \tau$, we analyze collective neutrino oscillations in a rotate basis $e - x - y$ [66] defined by

$$\begin{pmatrix} \nu_x \\ \nu_y \end{pmatrix} = \begin{pmatrix} \cos\theta_{23} & -\sin\theta_{23} \\ \sin\theta_{23} & \cos\theta_{23} \end{pmatrix} \begin{pmatrix} \nu_\mu \\ \nu_\tau \end{pmatrix}. \tag{4.3}$$

In dense material such as deep inside of stars, ν_μ and ν_τ acquire about the same effective mass, so that their spectra are almost degenerate. Such degeneracy inside a dense matter results in a decouple of one of flavors in neutrino oscillations [206]. This implies that behaviors of three flavor oscillations can be treated as a problem of two flavor oscillations in some special basis. The vacuum Hamiltonian in the $e - x - y$

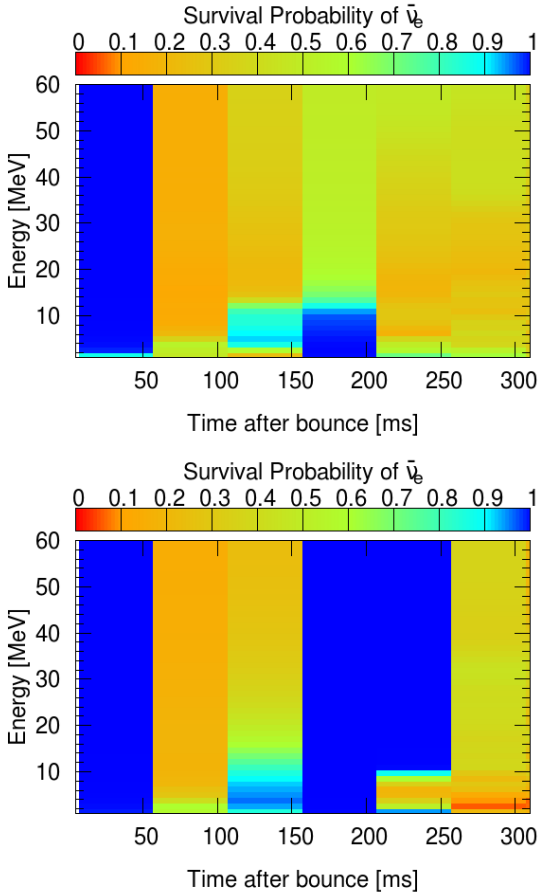

Figure 4.3: The survival probabilities of $\bar{\nu}_e$ at a radius of 1500 km as functions of neutrino energy and emission time. Top: the probability for the inverted mass hierarchy. Bottom: the probability for the normal mass hierarchy.

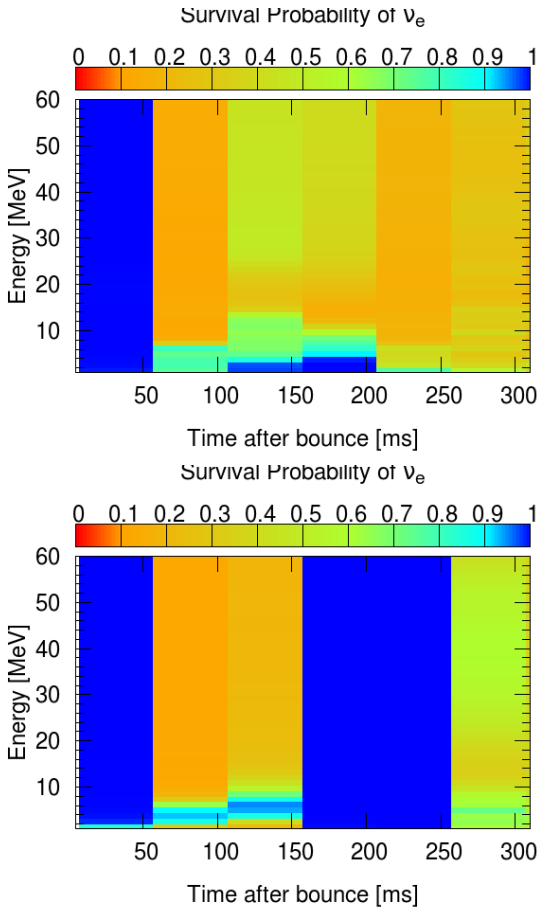

Figure 4.4: The survival probabilities of ν_e at a radius of 1500 km as Fig.4.3. The top (bottom) panels shows the probability for the inverted (normal) mass hierarchy, respectively.

basis is given by imposing $\theta_{23} = 0$ in Eq.(2.32):

$$\begin{aligned}\Omega(E) = \frac{\Delta m^2_{21}}{6E} \begin{pmatrix} 1 - 3c^2_{12}c^2_{13} & 3c_{12}s_{12}c_{13} & 3c^2_{12}s_{13}c_{13} \\ 3c_{12}s_{12}c_{13} & 1 - 3s^2_{12} & -3s_{12}c_{12}s_{13} \\ 3c^2_{12}s_{13}c_{13} & -3s_{12}c_{12}s_{13} & 1 - 3c^2_{12}s^2_{13} \end{pmatrix} \\ + \frac{\Delta m^2_{32}}{6E} \begin{pmatrix} -1 + 3s^2_{13} & 0 & 3s_{13}c_{13} \\ 0 & -1 & 0 \\ 3s_{13}c_{13} & 0 & -1 + 3c^2_{13} \end{pmatrix},\end{aligned} \tag{4.4}$$

where c_{ij} and s_{ij} stand for $\cos\theta_{ij}$ and $\sin\theta_{ij}$, respectively. This three flavor vacuum Hamiltonian is equivalent to Eq.(6) in Ref. [66] even though we employ different normalization: $\mathrm{Tr}\Omega(E) = 0$. One of the benefits of the $e - x - y$ basis is decoupling of ν_x in the second term of the right hand side of Eq.(4.4). In inverted mass hierarchy, this second term often induces significant $e - y$ conversions similar to behaviors of two flavor collective neutrino oscillations before the $e - x$ mixing because of $|\Delta m^2_{32}|/\Delta m^2_{21} > \mathcal{O}(10)$.

We can study collective neutrino oscillations directly by analyzing density matrices of neutrinos and antineutrinos as shown in §3.6 but conversion probabilities $P_{e\alpha} = P(\bar{\nu}_e \to \bar{\nu}_\alpha)$ $(\alpha = e, x, y)$ [71] are also helpful to understand behavior of collective neutrino oscillations. Fig.4.5 shows radial profiles of conversion probabilities of $\bar{\nu}_e$ at 231 ms in inverted mass hierarchy. In our multiangle simulation, such conversion probabilities are derived by angular averaged diagonal components of density matrices:

$$P(\bar{\nu}_e \to \bar{\nu}_\alpha)(r, E) = \frac{\langle \bar{\rho}_{\alpha\alpha}(r, E)\rangle - \langle \bar{\rho}_{xx}(R_\nu, E)\rangle}{\langle \bar{\rho}_{ee}(R_\nu, E)\rangle - \langle \bar{\rho}_{xx}(R_\nu, E)\rangle}, \tag{4.5}$$

where $\alpha = e, x, y$ and $\langle..\rangle$ represents the angular average over the emission angle like Eq.(5.15). The top panel of Fig.4.5 corresponds to the evolution of survival probabilities of $\bar{\nu}_e$. The value of P_{ee} remains unity as long as flavor transitions are negligible. The middle and bottom panels show how emitted $\bar{\nu}_e$ on the surface of the neutrinosphere is transformed to $\bar{\nu}_y$ and $\bar{\nu}_x$, respectively. The origin of non-linear flavor transitions in this multiangle simulation are qualitatively the same as that of single

angle calculation in §3.6. When the strength of neutrino self interactions is comparable with vacuum frequencies, non-diagonal components of $V_{\rm self}(r, \theta_p)$ (Eq.(3.29)) grow up prominently, which gives rise to non-linear collective motion in flavor space.

As expected in Eq.(4.4), the electron antineutrino essentially experiences collective neutrino oscillations in the $e - y$ sector in inverted mass hierarchy. In Fig.4.5, we show the flavor evolution in inverted mass hierarchy for three $\bar{\nu}_e$ energies: 2.4, 12.0 and 40.0 MeV. It can be seen that non-linear motion starts around 250 km in the $e - y$ sector: the survival probability decreases (top panel) and the conversion probability P_{ey} increases (bottom panel). Such non-linear $e - y$ conversions in inverted mass hierarchy are also confirmed in a two flavor multiangle simulation [74] and a three flavor multiangle simulation using a more massive progenitor [80]. Subsequent collective neutrino oscillations occur in $\bar{\nu}_x$ at 450 km after the early $e - y$ mixing. Two types of non-linear transitions reflect the coupling of self interaction with two vacuum frequencies, $\omega_{\rm solar} = \Delta m^2_{21}/2E$ and $\omega_{\rm atm} = |\Delta m^2_{32}|/2E$. Such three flavor peculiar mixing is also found in previous numerical studies [71, 72] and arise from a small flavor asymmetry in the neutrino number luminosity, e.g., at 231 ms: $\Phi^0_{\nu_e} : \Phi^0_{\bar{\nu}_e} : \Phi^0_{\nu_X} = 1.17 : 1.09 : 1.00$. As shown in the bottom panel of Fig.4.1, the flavor asymmetry becomes smaller as time proceeds, which enhances the three flavor mixing in the post-accretion phase. Finally, collective neutrino oscillations have finished at 1000 km and conversion probabilities settle down to constant values. The flavor mixing is energy dependent. For example, low energy electron antineutrinos transform to other flavor $\bar{\nu}_x$ actively and $\bar{\nu}_y$ returns to the original flux as shown by the 2.4 MeV curves in Fig.4.5. On the other hand, $e - x$ mixing becomes small in more energetic electron antineutrinos, for example 12.0 and 40.0 MeV, even though the vacuum frequency $\omega_{\rm atm}$ induces partially $\bar{\nu}_y - \bar{\nu}_x$ conversions.

4.2.3 The $e - x$ conversions in normal mass hierarchy

In normal mass hierarchy, collective neutrino oscillations appear in two time domains around 100 and 300 ms post bounce even though non-linear flavor conversions continue after 50 ms post bounce in inverted mass hierarchy. Such hierarchy difference

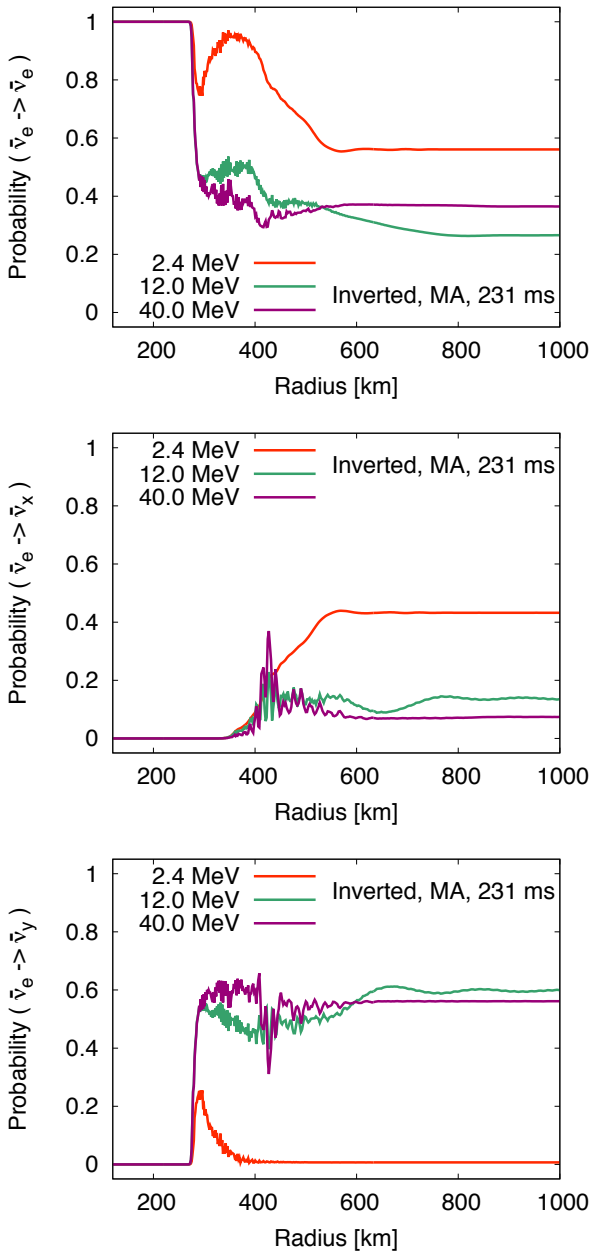

Figure 4.5: The radial profiles of conversion probabilities of $\bar{\nu}_e$ at 231 ms post bounce. The inverted mass hierarchy is assumed and multiangle scheme (labeled MA) is used. The different colors show the profile at different energies of the neutrino: red, green and violet correspond to 2.4, 12.0 and 40.0 MeV, respectively.

may come from the different multiangle suppressions [65] in $e-x$ and $e-y$ sectors. It seems that the role of $\bar{\nu}_x$ in normal mass hierarchy is that of $\bar{\nu}_y$ in inverted mass hierarchy. The $e-y$ conversion occurs dominantly thorough almost all energy region in inverted mass hierarchy. On the other hand, the $e-x$ conversion occurs dominantly in normal mass hierarchy. This feature is clearly seen in Fig.4.6. At ~ 100 ms, collective neutrino oscillations appear at about 700 km and the values of survival probabilities of 12.0 and 40.0 MeV settle down to ~ 0.2, while the survival probability of low energy neutrino (2.4 MeV) is about 0.5 at 1500 km. A significant fraction of electron antineutrino is converted to x antineutrino. At ~ 200 ms, any non-linear flavor conversions do not appear because of the dense electron background which induces the strong multiangle matter suppression in $e-x$ sector. At ~ 300 ms, collective neutrino oscillations revive owing to the reduction of the electron density outside the neutrino sphere. Three flavor mixing is significant due to the small asymmetry between neutrino number luminosities [72]. Flavor transitions mainly occur in $e-x$ sector and $x-y$ mixing follows it in energetic neutrinos and antineutrinos.

The dominant $e-x$ conversion in normal mass hierarchy as shown in Fig.4.6 has not been shown in previous three flavor simulations [66, 71, 72, 80]. We discuss a possible mechanism of such a new type of flavor mixing which would be equivalent to an instability for normal mass hierarchy suggested in a recent work [207]. We remark that such $e-x$ conversions in normal mass hierarchy are not caused by overlap between MSW resonances and neutrino self-coupling as confirmed during the neutronization burst [68]. We begin with a simpler problem. Namely, in two flavor collective neutrino oscillations, the relation between the direction of vacuum polarization vector $\omega\mathbf{B}$ and nonlinear polarization vector $\mathbf{D}$ (strictly speaking, sign of an inner product $\omega D_{\parallel} = \omega\mathbf{B}\cdot\mathbf{D}$) is crucial for the development of nonlinear effects [60]. For example, in previous two flavor demonstration, significant spectral swap are confirmed in inverted mass hierarchy ($\omega D_{\parallel} > 0$) as shown in Figs. 3.8 and 3.9. On the other hand, flavor transitions are negligible in normal mass hierarchy ($\omega D_{\parallel} < 0$). Here, the direction of polarization vector $\mathbf{P} = (P_x, P_y, P_z)$ is given by the sign of the z-component (note in this discussion the meanings of x, y are different from that of the rotated basis). The initial value of nonlinear potential

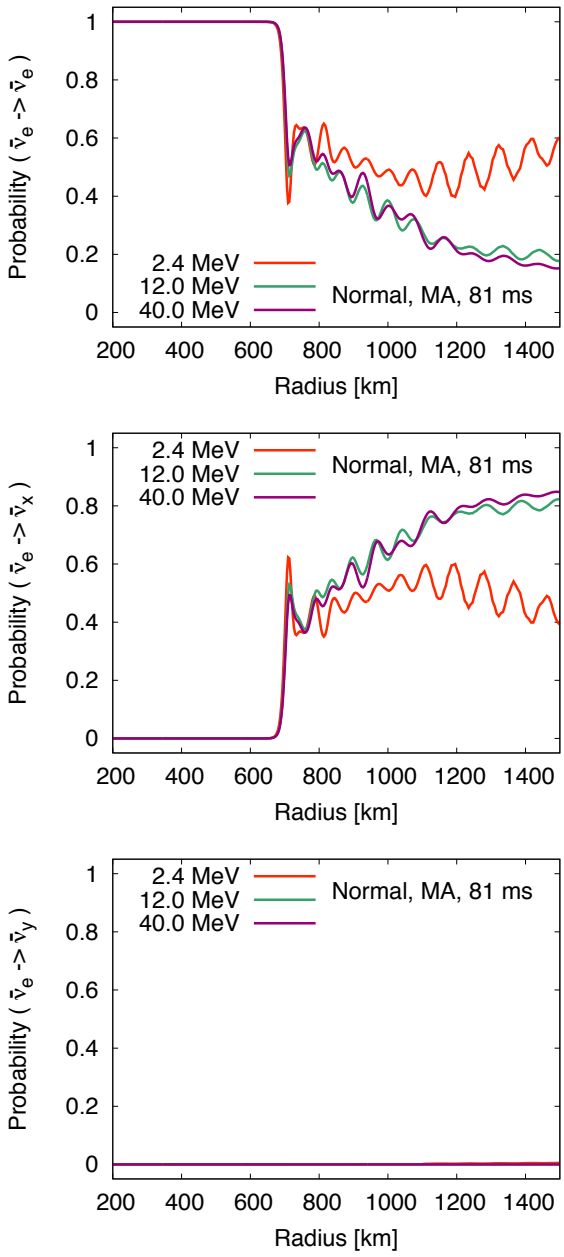

Figure 4.6: The radial profiles of conversion probabilities of $\bar{\nu}_e$ at 81 ms post bounce. The normal mass hierarchy is assumed and multiangle scheme (labeled MA) is used. The different colors show the profile at different energies of the neutrino: red, green and violet correspond to 2.4, 12.0 and 40.0 MeV, respectively.

is independent of neutrino mass hierarchy, so we only focus on the z-component of the vacuum polarization vector in each neutrino sector. Now in reality, we have to consider three flavor cases. In a rotated basis $e-x-y$, the vacuum Hamiltonian of three flavor neutrinos $\Omega(E)$ is described by Eq.(4.4). The decreasing nonlinear potential $V_{\rm self}(r,\theta_p)$ first couples to the second term on the right hand side of Eq.(4.4) which induces only $e-y$ conversions. From the definition of polarization vectors in Eq.(3.39), the z-component of the vacuum Hamiltonian in the $e-y$ sector is obtained by the difference between two diagonal components in the $e-y$ sector,

$$\Omega(E)_{ee}-\Omega(E)_{yy}\sim-\frac{\Delta m^2_{32}}{2E}\cos 2\theta_{13}, \tag{4.6}$$

where the sign of Δm^2_{32} depends on the neutrino mass hierarchy. If the sign of D_z is positive ($\Phi^0_{\nu_e}>\Phi^0_{\bar{\nu}_e}$), the positive sign in Eq.(4.6) is preferable for significant flavor transitions in the $e-y$ sector as shown in two flavor collective neutrino oscillations in inverted mass hierarchy (see §3.6 and Refs. [61, 189]).

We remark that some $e-y$ conversion also appears even in normal mass hierarchy if the asymmetry among neutrino number luminosities $\Phi^0_i(i=\nu_e,\bar{\nu}_e,\nu_x)$ is small enough to induce multiple spectral swaps in the inverted mass hierarchy [71]. This explains the $e-y$ conversion around $\sim$ 300 ms in normal mass hierarchy. In our explosion model, the asymmetry of neutrino number luminosity gradually decreases as shown in the bottom panel of Fig.4.1. Conversely, $e-y$ conversions in normal mass hierarchy are negligible for early explosion era of $\sim$ 100 ms. The $e-x$ conversions in normal mass hierarchy can be discussed in the same way as $e-y$ conversions above. Large instabilities would appear in $e-x$ conversions if the z-component of the vacuum Hamiltonian in the $e-x$ sector,

$$\begin{aligned}\Omega(E)_{ee}-\Omega(E)_{xx}=&-\frac{\Delta m^2_{21}}{2E}\left(\cos 2\theta_{12}-\cos^2\theta_{12}\sin^2\theta_{13}\right)\\&+\frac{\Delta m^2_{32}}{2E}\sin^2\theta_{13}.\end{aligned} \tag{4.7}$$

takes positive values. in inverted mass hierarchy ($\Delta m^2_{32}<0$), the sign of Eq.(4.7) is always negative because of $\Delta m^2_{21}>0$ and $|\Delta m^2_{32}|/\Delta m^2_{21}>\mathcal{O}(10)$. However, Eq.(4.7)

becomes positive in normal mass hierarchy ($\Delta m^2_{32} > 0$) if we impose a finite mixing angle θ_{13} larger than below a critical value

$$\sin^2\theta_{13} > \frac{\cos 2\theta_{12}}{\Delta m^2_{32}/\Delta m^2_{21} + \cos^2\theta_{12}}. \tag{4.8}$$

The matter potential can be canceled out in a co-rotating frame [58] which moves together with the non-linear potential of neutrino self interactions if the electron density is small enough to avoid the multiangle matter suppression (see §4.2.4). Therefore, the above criterion may be applicable to a sparse electron background. Our neutrino mixing parameters satisfy the condition in Eq.(4.8). This is also true for more updated values of neutrino mixing parameters [92]. On the other hand, Eq.(4.8) is violated in case of small mixing angle θ_{13} used in previous studies [66, 71, 72]. This seems to be a plausible reason why the $e-x$ conversions in normal mass hierarchy are discovered in our simulation but not confirmed in Refs. [66, 71, 72]. The $e-x$ conversions are not found in Ref. [80] in spite of a large value of θ_{13}. This might be related to the strong multiangle matter suppression in $e-x$ sector in the massive progenitor model ($18M_\odot$). In fact, flavor conversions in normal mass hierarchy are easily suppressed in a dense electron background as shown in the bottom panels of Figs.4.3 and 4.4. Nevertheless, further studies are necessary for more robust conclusions.

4.2.4 Multiangle matter effects

Complete spectral swap of neutrinos as shown in single angle calculations (see Figs.3.8 and 3.9) is not confirmed in multiangle simulations. For example, Fig.4.7 represents a comparison of neutrino spectra after collective neutrino oscillations at 281 ms post bounce in inverted mass hierarchy by using both the single (left) and the multiangle simulation (right). In case of the single angle calculation (left), there are two spectral splits around $E^{(1)}_{\rm split} = 5$ MeV and $E^{(2)}_{\rm split} = 42$ MeV in case of single angle calculation. The complete spectral swap in $e-y$ sector occurs in the energy range of $E^{(1)}_{\rm split} < E < E^{(2)}_{\rm split}$. On the other hand, the $e-x$ mixing is dominant in $E > E^{(2)}_{\rm split}$. Such three flavor multiple spectral splits in inverted mass hierarchy are also confirmed in previous studies [70–72] where $\Phi^0_{\nu_X}$ is the largest among all initial neutrino fluxes. As shown in the bottom panel of Fig.4.1, the asymmetry among neutrino fluxes becomes

small as the explosion time has passed, which increases the ratio of $\Phi^0_{\nu_X}$ in initial neutrino fluxes and results in multiple spectral swap in the later explosion phase. In multiangle calculation (right), however, multiple spectral splits are washed out badly. Such property is consistent with numerical results of multiangle calculation in Refs. [72, 73]. The multiangle effects are remarkable in case of small asymmetry in initial neutrino fluxes [64,72]. A quasi-single angle oscillations occur if the asymmetry of neutrino fluxes is large. This case often induces a single crossing in neutrino spectra after collective neutrino oscillations as shown in the right panel of Fig.(3.8). The smeared spectral swap in Fig.4.7 is caused by the multiangle matter suppression [65]. As shown in Eqs.(3.30) and (3.31), the time evolution of density matrices include the contribution of scattering angle $\cos\theta_p$, which gives rise to angular dispersion in matter potential in outer region ($r >> R_\nu$):

$$V_{\rm MSW}(r)/\cos\theta_p \sim V_{\rm MSW}(r) + \frac{\sin^2\theta_R}{2}\left(\frac{R_\nu}{r}\right)^2 V_{\rm MSW}(r), \tag{4.9}$$

where $V_{\rm MSW}(r) = \sqrt{2}G_F n_e(r)\ {\rm diag}(1,0,0)$ and θ_R is the emission angle on the surface of neutrino sphere in Fig.3.5. The first term of Eq.(4.9) is independent of neutrino energy and scattering angle, so that this term can be removed from the equation of motion of density matrices by going to a rotating frame as employed in §3.8. Therefore, non-linear phenomena in single angle calculations are not so sensitive to the matter potential even though the onset of collective neutrino oscillations is somewhat delayed [60]. However, in multiangle calculation, the second term of Eq.(4.9) can not be eliminated because of the θ_R dependence. Such angular dispersion in matter potential breaks the coherence of collective neutrino oscillations. Then, complete spectral swap obtained in the single angle calculation is smeared out. The multiangle matter effect is negligible when the strength of neutrino self interaction overcomes that of the angular disperion in Eq.(4.9). The criteria is given by $n_{e^-} - n_{e^+} << n_\nu$ [65, 73] where n_ν is a neutrino number density. Conversely, any collective neutrino oscillations are ignored if the net electron number density is much higher than that of neutrinos. Fig.4.8 shows neutrino spectra after collective neutrino oscillations at 181 ms in normal mass hierarchy. In the single angle case (left), ν_y almost decouples from

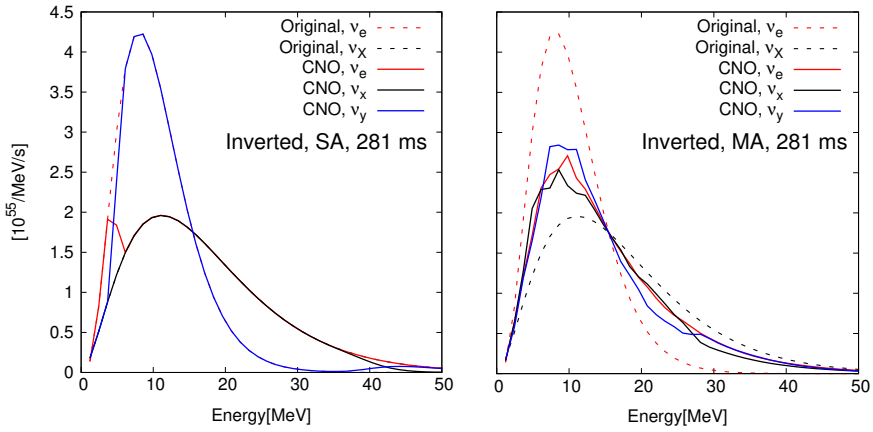

Figure 4.7: Neutrino spectra after collective neutrino oscillations (CNO) in both single angle (left) and multiangle calculations (right) at 281 ms post bounce in inverted mass hierarchy.

flavor conversions and a sharp energy split appears at ~ 5 MeV like two flavor oscillations. The three flavor mixing in high energy region would be negligible because of large asymmetry of initial neutrino fluxes. On the other hand, any flavor conversion disappears in multiangle calculation (right) because of the strong multiangle matter suppression caused by dense ejecta from the neutrino sphere. Flavor transitions in multiangle simulations are highly sensitive to the matter profile outside the neutrino sphere. The decreased matter profiles at ~ 100 ms and ~ 300 ms enable flavor transitions in normal mass hierarchy as shown in the bottom panel of Figs.4.3 and 4.4. The dilute envelop of electron capture supernovae is preferable to avoid the multiangle matter suppression. In massive progenitor model, collective neutrino oscillations are more weakened because of dense outer material. Here, we discuss the matter effect on spectral swap but the onset of flavor transitions are delayed in multiangle simulations because of the angular dispersion in $V_{\rm self}(r, \theta_p)$ [73], which is crucial for precise abundance of nuclei as mentioned in Chapter 5.

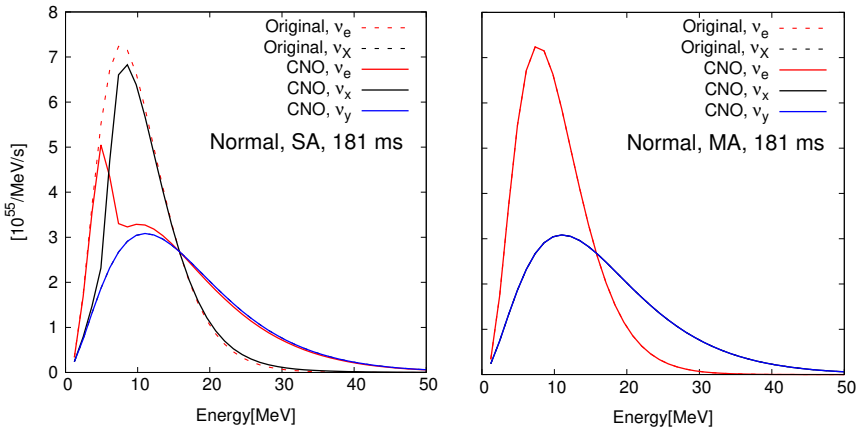

Figure 4.8: Neutrino spectra at 181 ms post bounce in normal mass hierarchy as Fig.4.7.

4.2.5 Contributions from MSW resonances to neutrino spectra on the earth

After collective neutrino oscillations, neutrino spectra are affected by matter effects in outer layers of the star where the baryon density decreases down to the critical density for MSW resonances:

$$\begin{aligned}\rho_{cr} &= \frac{\Delta m^2}{2\sqrt{2}G_F E N_A Y_e}\cos 2\theta \\ &= 2.63\times 10^4 \mathrm{g/cm^3}\left(\frac{\Delta m^2}{2\times 10^{-3}\mathrm{eV}^2}\right)\left(\frac{Y_e}{0.5}\right)^{-1}\left(\frac{E}{\mathrm{MeV}}\right)^{-1}\cos 2\theta\end{aligned} \tag{4.10}$$

where N_A is the Avogadro number. Above condition is equivalent to Eq.(2.69). We should take into account MSW effects in order to derive neutrino spectra on the earth. Neutrino spectra after MSW resonances are derived analytically if flavor transitions occur adiabatically as discussed in §2.7. The evolution of adiabatic flavor transitions is shown in Fig.4.9. In three flavor neutrinos, there are two resonances associated with two vacuum frequencies. Emitted neutrinos after collective neutrino oscillations

first experience the high (H) resonance in $e-y$ sector whose critical density ρ_{cr} is characterized by $(\Delta m^2_{32}, \theta_{13})$. After that, the low (L) resonance induces three flavor mixing owing to another set of mixing parameters $(\Delta m^2_{21}, \theta_{12})$. The L resonance is regarded as the two flavor MSW effects in $e-x$ sector because ey and ex components of the first term on the right hand side of Eq.(4.4) are small in our mixing parameters. After the adiabatic MSW resonances, each neutrino settles down to vacuum mass eigenstates (ν_1, ν_2, ν_3). According to the upper panel of Fig.4.9, in normal mass hierarchy, neutrino energy spectra on the earth $\{f^{(f)}_{\nu_\alpha}, f^{(f)}_{\bar{\nu}_\alpha}\}$ $(\alpha = e, \mu, \tau)$ are given by

$$\begin{pmatrix} f^{(f)}_{\nu_e} & 0 & 0 \\ 0 & f^{(f)}_{\nu_\mu} & 0 \\ 0 & 0 & f^{(f)}_{\nu_\tau} \end{pmatrix} = U_3 \begin{pmatrix} f^{(a)}_{\nu_x} & 0 & 0 \\ 0 & f^{(a)}_{\nu_y} & 0 \\ 0 & 0 & f^{(a)}_{\nu_e} \end{pmatrix} U_3^\dagger, \tag{4.11}$$

$$\begin{pmatrix} f^{(f)}_{\bar{\nu}_e} & 0 & 0 \\ 0 & f^{(f)}_{\bar{\nu}_\mu} & 0 \\ 0 & 0 & f^{(f)}_{\bar{\nu}_\tau} \end{pmatrix} = U_3 \begin{pmatrix} f^{(a)}_{\bar{\nu}_e} & 0 & 0 \\ 0 & f^{(a)}_{\bar{\nu}_x} & 0 \\ 0 & 0 & f^{(a)}_{\bar{\nu}_y} \end{pmatrix} U_3^\dagger, \tag{4.12}$$

where U_3 is the PMNS matrix in Eq.(2.31) and $\{f^{(a)}_{\nu_\alpha}, f^{(a)}_{\bar{\nu}_\alpha}\}$ $(\alpha = e, x, y)$ are neutrino spectra at 1500 km after collective neutrino oscillations. Here, we ignore slight modification by matter effects inside the earth [208]. Concretely, the spectrum $f^{(a)}_{\bar{\nu}_\alpha}$ [1/MeV/s] is derived from diagonal components of density matrices at 1500 km:

$$\begin{aligned} f^{(a)}_{\bar{\nu}_\alpha} &= f_{\bar{\nu}_\alpha}(r = 1500\text{km}) \\ &= \left[4\pi r^2 \int^1_{\sqrt{1-(R_\nu/r)^2}} \mathrm{d}(\cos\theta_p) \sum_{\alpha=e,\mu,\tau} \frac{L_{\bar{\nu}_\alpha}}{2\pi R^2_\nu \langle E_{\bar{\nu}_\alpha} \rangle} f_{\bar{\nu}_\alpha}(E) \bar{\rho}_{\alpha\alpha}(r, E, \theta_p) \cos\theta_p \right]_{r=1500\text{km}} . \end{aligned}$$

In the above equation, the scattering angle θ_p is integrated and only energy dependence is left. The antineutrino spectra $f_{\bar{\nu}_\alpha}(r)$ is almost independent of the radius r in outer region $r >> R_\nu$. Then, the number flux of $\bar{\nu}_\alpha$ in outer region is given by $F_{\bar{\nu}_\alpha}(r) = f_{\bar{\nu}_\alpha}(r)/4\pi r^2$. The right panel of Fig.4.8 represents $\{f^{(a)}_{\bar{\nu}_\alpha}\}$ $(\alpha = e, x, y)$ at 281 ms in inverted mass hierarchy. The value of $f^{(a)}_{\nu_\alpha}$ is also obtained in the same treatment by imposing the diagonal component of neutrino density matrices $\rho_{\alpha\alpha}$. In the supernova neutrino burst, we are interested in spectra of ν_e and $\bar{\nu}_e$. For normal

mass hierarchy, the fluxes of e-type neutrinos are

$$f_{\nu_e}^{(\mathrm{f})} = s_{13}^2 f_{\nu_e}^{(\mathrm{a})} + c_{12}^2 c_{13}^2 f_{\nu_x}^{(\mathrm{a})} + s_{12}^2 c_{13}^2 f_{\nu_y}^{(\mathrm{a})}, \tag{4.13}$$

$$f_{\bar{\nu}_e}^{(\mathrm{f})} = c_{12}^2 c_{13}^2 f_{\bar{\nu}_e}^{(\mathrm{a})} + s_{12}^2 c_{13}^2 f_{\bar{\nu}_x}^{(\mathrm{a})} + s_{13}^2 f_{\bar{\nu}_y}^{(\mathrm{a})}, \tag{4.14}$$

where c_{ij} and s_{ij} stand for $\cos\theta_{ij}$ and $\sin\theta_{ij}$, respectively. In inverted mass hierarchy, the final neutrino spectra are derived in the same way as the case of normal mass hierarchy:

$$\begin{pmatrix} f_{\nu_e}^{(f)} & 0 & 0 \\ 0 & f_{\nu_\mu}^{(f)} & 0 \\ 0 & 0 & f_{\nu_\tau}^{(f)} \end{pmatrix} = U_3 \begin{pmatrix} f_{\nu_x}^{(a)} & 0 & 0 \\ 0 & f_{\nu_e}^{(a)} & 0 \\ 0 & 0 & f_{\nu_y}^{(a)} \end{pmatrix} U_3^\dagger, \tag{4.15}$$

$$\begin{pmatrix} f_{\bar{\nu}_e}^{(f)} & 0 & 0 \\ 0 & f_{\bar{\nu}_\mu}^{(f)} & 0 \\ 0 & 0 & f_{\bar{\nu}_\tau}^{(f)} \end{pmatrix} = U_3 \begin{pmatrix} f_{\bar{\nu}_y}^{(a)} & 0 & 0 \\ 0 & f_{\bar{\nu}_x}^{(a)} & 0 \\ 0 & 0 & f_{\bar{\nu}_e}^{(a)} \end{pmatrix} U_3^\dagger, \tag{4.16}$$

Then, the fluxes of ν_e and $\bar{\nu}_e$ on the earth are given by

$$f_{\nu_e}^{(\mathrm{f})} = s_{12}^2 c_{13}^2 f_{\nu_e}^{(\mathrm{a})} + c_{12}^2 c_{13}^2 f_{\nu_x}^{(\mathrm{a})} + s_{13}^2 f_{\nu_y}^{(\mathrm{a})}, \tag{4.17}$$

$$f_{\bar{\nu}_e}^{(\mathrm{f})} = s_{13}^2 f_{\bar{\nu}_e}^{(\mathrm{a})} + s_{12}^2 c_{13}^2 f_{\bar{\nu}_x}^{(\mathrm{a})} + c_{12}^2 c_{13}^2 f_{\bar{\nu}_y}^{(\mathrm{a})}. \tag{4.18}$$

These analytical treatment of MSW resonances after collective neutrino oscillations are also employed in previous studies [66,80,83]. The coefficients $c_{12}^2 c_{13}^2 \sim 0.7$, $s_{12}^2 c_{13}^2 \sim 0.3$, $s_{13}^2 \sim 0$ are weight of flavor mixing through the matter effect. The neutrino spectra after collective neutrino oscillations $\{f_{\nu_\alpha}^{(f)}, f_{\bar{\nu}_\alpha}^{(f)}\}$ are also described by linear combination of original spectra on the surface of the neutrino sphere $\{f_{\nu_e}^{(o)}, f_{\bar{\nu}_e}^{(o)}, f_{\nu_X}^{(o)}\}$. As shown in the middle panel of Fig.4.1, the mean energy of ν_X is the highest after 50 ms, which results in hard spectra $f_{\nu_X}^{(o)}$. Collective neutrino oscillations make spectra of e-type neutrinos hard because energy swap in high energy region increases weight of $f_{\nu_X}^{(o)}$. On the other hand, a complete spectral swap occurs in $e-y$ sector at the H resonance. Such significant flavor transition induces soft e-type neutrino spectra again.

Fig.4.10 shows number fluxes of electron antineutrinos on the earth by using a

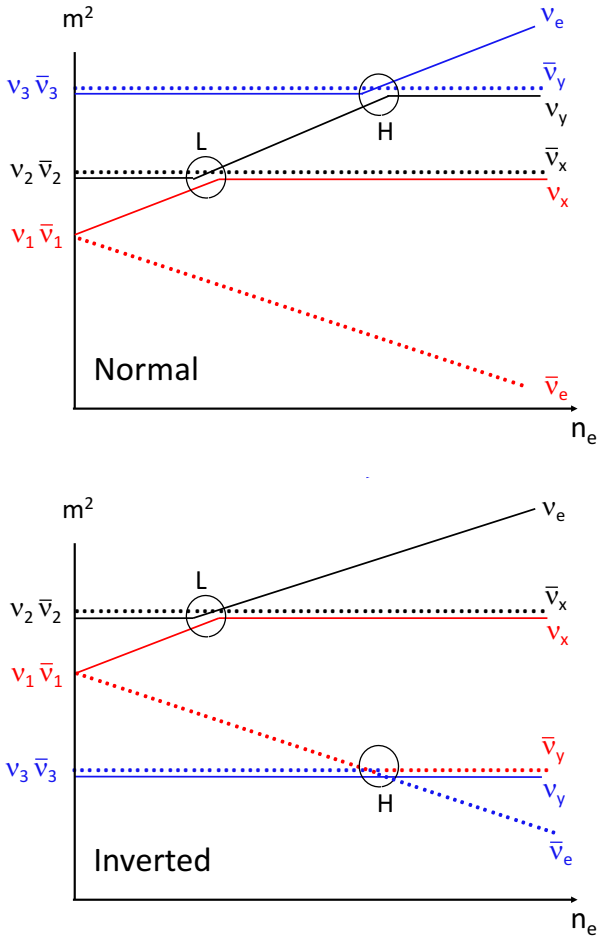

Figure 4.9: The schematic pictures of crossing diagrams through MSW resonances in three flavor neutrinos and antineutrinos in analogy with the left panel of Fig.2.3. The top (bottom) panel represents the case in normal (inverted) mass hierarchy, respectively. The solid and dot lines correspond to effective masses of ν and $\bar{\nu}$. The symbols L and H show low and high MSW resonances associate with $\omega_{\rm solar} = \Delta m^2_{21}/2E$ and $\omega_{\rm atm} = |\Delta m^2_{32}|/2E$ in Eq.(4.4), respectively.

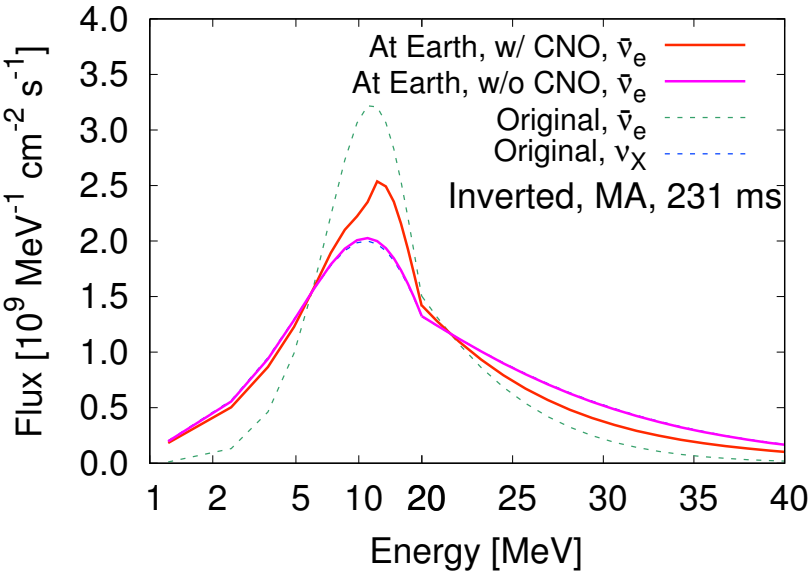

Figure 4.10: Flux spectra of electron antineutrinos in inverted mass hierarchy. Here, the source distance $d = 10$ kpc is assumed and the time snapshot of 231 ms is used. The red line represents a flux spectrum of electron antineutrinos on the earth including collective neutrino oscillations (CNO) and MSW effects. For comparison, electron antineutrino without collective neutrino oscillations (magenta), original electron neutrino (green dotted) and heavy lepton neutrino (blue dotted) are shown. The horizontal axis is logarithmic for $E < 20$ MeV and liner for $E > 20$ MeV in the both panels.

time snapshot at 231 ms post bounce in inverted mass hierarchy. The number flux of $\bar{\nu}_e$ on the earth is described by

$$F^{(f)}_{\bar{\nu}_e} = \frac{f^{(\mathrm{f})}_{\bar{\nu}_e}}{4\pi d^2}, \tag{4.19}$$

where d is the distance to the neutrino source. The number fluxes shown in Fig.4.10 assume a source distance of $d = 10$ kpc (1pc$= 3.09 \times 10^{18}$ cm), which corresponds approximately to the distance to the Galactic center. In the absence of collective neutrino oscillations, $\bar{\nu}_e$ spectrum (magenta) almost corresponds to the original spectrum of ν_X (blue) because of $f^{(\mathrm{a})}_{\bar{\nu}_x} = f^{(\mathrm{a})}_{\bar{\nu}_y} = f^{(\mathrm{o})}_{\nu_X}$ in Eq.(4.18). On the other hand, the amplitude of $\bar{\nu}_e$ flux considering collective neutrino oscillations (red) becomes small in high energy region. Such softened $\bar{\nu}_e$ spectrum has large influence on the neutrino detection, which may result in the clarification of collective neutrino oscillations. Fig.4.5 shows that energetic antineutrinos experience active flavor transitions in $e - y$ sector. The $e - x$ conversion is suppressed except for low energy region as shown, for example, by 2.4 MeV antineutrinos in Fig.4.5. In general, three flavor mixing would induce complex spectral swaps different from a simple two flavor picture but $e - x$ conversions in low energy region do not strongly contribute to the total event rates. The spectral swap of energetic $\bar{\nu}_e$ is approximately regarded as two flavor conversions in $e - y$ sector. The spectra of $\bar{\nu}$ in high energy region is roughly written as

$$f^{(\mathrm{a})}_{\bar{\nu}_e} \sim \epsilon f^{(\mathrm{o})}_{\bar{\nu}_e} + (1-\epsilon) f^{(\mathrm{o})}_{\bar{\nu}_X}, \tag{4.20}$$

$$f^{(\mathrm{a})}_{\bar{\nu}_x} \sim f^{(\mathrm{o})}_{\bar{\nu}_X}, \tag{4.21}$$

$$f^{(\mathrm{a})}_{\bar{\nu}_y} \sim (1-\epsilon) f^{(\mathrm{o})}_{\bar{\nu}_e} + \epsilon f^{(\mathrm{o})}_{\bar{\nu}_X}, \tag{4.22}$$

where ϵ is survival probability of $\bar{\nu}_e$ in $e - y$ sector. Complete spectral swaps ($\epsilon = 0$) fails in our multiangle simulation because of the multiangle matter effects as mention in §4.2.4. After collective neutrino oscillations, the spectrum of $\bar{\nu}_e$ becomes hard because of the contribution from $f^{(\mathrm{o})}_{\bar{\nu}_X}$ in Eq.(4.20), which enhances the νp-process nucleosynthesis inside neutrino driven winds (see Chapter 5). Under this two flavor picture in $e - y$ sector, the $\bar{\nu}_e$ spectrum after the H resonance is given by

$$f^{(\mathrm{f})}_{\bar{\nu}_e} \sim 0.7(1-\epsilon) f^{(\mathrm{o})}_{\bar{\nu}_e} + (0.3 + 0.7\epsilon) f^{(\mathrm{o})}_{\bar{\nu}_X}. \tag{4.23}$$

Above equation clearly indicates that finite flavor mixing ($\epsilon < 1$) decreases the contribution from original spectrum of ν_X, which results in soft $\bar{\nu}_e$ on the earth. According to the top panel of Fig.4.3, the survival probability of $\bar{\nu}_e$ at 231 ms is ~ 0.3 for $E > 20$ MeV. From Eq. (4.23), we obtain $f^{(\mathrm{f})}_{\bar{\nu}_e} = 0.49 f^{(\mathrm{o})}_{\bar{\nu}_e} + 0.51 f^{(\mathrm{o})}_{\bar{\nu}_X}$ for $\epsilon = 0.3$. This can be confirmed in Fig.4.10, where $f^{(\mathrm{f})}_{\bar{\nu}_e}$ (red line) sits almost at midpoint between $f^{(\mathrm{o})}_{\bar{\nu}_X}$ (blue line) and $f^{(\mathrm{o})}_{\bar{\nu}_e}$ (green line) for this energy range. In inverted hierarchy, this two flavor assumption in $e-y$ sector is most valid for the time between 80 ms to 250 ms post bounce. Around 300 ms, three flavor mixing occurs actively and the matter-induced spectral swap becomes more complex. We only focus on the case in inverted mass hierarchy, but the same discussion is possible in normal mass hierarchy. Around 100 ms, in normal mass hierarchy, two flavor conversions appear in $e-x$ sector. The spectra of ν_e becomes soft on the earth instead of $\bar{\nu}_e$ because the H resonance exists in neutrino sector as shown in the upper panel of Fig.4.9.

4.2.6 Detection Property of $\bar{\nu}_e$

We discuss the detectability of collective neutrino oscillations in electron capture supernovae through the observational signal of $\bar{\nu}_e$ in Hyper-Kamiokande (HK) and JUNO. There are several reactions for neutrino detection in these facilities [36, 37], but the main signal for supernova neutrino burst is given by the inverse beta decay: $\bar{\nu}_e + p \to e^+ + n$. The event rate of the inverse beta decay: $\frac{\mathrm{d}N}{\mathrm{d}t}$ [s^{-1}] can be evaluated by the following equation:

$$\frac{\mathrm{d}N}{\mathrm{d}t} = N_{\mathrm{tar}} \int_{E_{\mathrm{th}}} F\sigma \mathrm{d}E, \tag{4.24}$$

where N_{tar} is the number of the target in the detector, E_{th} is the threshold energy of the detector, F [$\mathrm{MeV}^{-1}\mathrm{cm}^{-2}\mathrm{s}^{-1}$] is the number flux of neutrino on the earth and $\sigma(E)$ [cm^2] is the cross section of the target to neutrinos. The variables in the integral of Eq.(4.24) depend on the energy of the neutrino E [MeV]. In addition, the neutrino number flux F is proportional to the inverse square of the source distance d^{-2} as shown in Eq.(4.19). Here we ignore the dependence of kinetic energy of the scattered particle in the cross section. In general, we have to take into account that. For example, in the case of the scattering of neutrino and electron, the kinetic energy

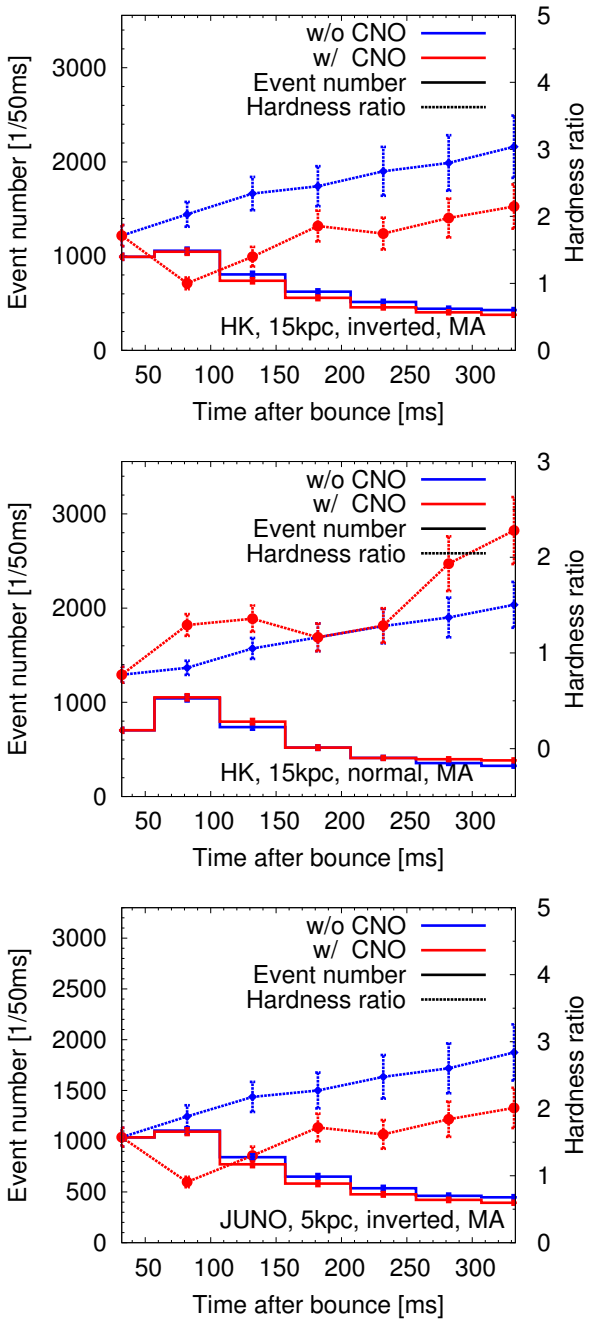

Figure 4.11: Evolution of event number in 50 ms bins (solid lines, left axis) and the hardness ratio (dotted lines, right axis) with/wihtout collective neutrino oscillations (CNO). Top: That of HK in inverted mass hierarchy. A volume of 220 kton is adopted. Middle: That of HK in normal mass hierarchy. Bottom: That of JUNO in inverted mass hierarchy. See the text for adopted detector parameters.

of the electron should be considered in the equation. In the case of inverse beta decay, the kinetic energy is identically determined and we do not have to include it explicitly in the equation.

In the case of HK detector, we adopt

$$N_{\rm tar} = N_{\rm A} \left(\frac{2M_{\rm H}}{M_{\rm H_2O}} \right) \rho_{\rm H_2O} V, \tag{4.25}$$

where V is the volume of the detector, set to 220 kton, $N_{\rm A}$ is Avogadro constant, and $\rho_{\rm H_2O}$ is the density of water. In the equation, $\left(\frac{2M_{\rm H}}{M_{\rm H_2O}} \right)$ is the mass fraction of hydrogen in H_2O and equals $\frac{2}{18}$. We use the cross section of $\sigma = 9.77 \times 10^{-44} \left(\frac{E}{1\ [\rm MeV]} \right)^2$ [cm^2]. Including corrections of order $1/M_p$ to the cross section and kinematics [209] yields typically 10-20% reduction in event rates depending on detection threshold. The threshold energy is set to $E_{\rm th} = 8.3\,\rm MeV$ [187].

Hundreds of neutrinos will be detected in every 50 ms bin in HK and JUNO when a supernova occurs near the galactic center as shown in Fig.4.11 in solid lines (the left axis). The top (middle) panel represents the case of HK in inverted (normal) mass hierarchy, respectively. The event number in 50 ms bin is given by $N = \frac{{\rm d}N}{{\rm d}t} \times \Delta t$ where $\Delta t = 0.05$ [s]. The error bar of the line, $\pm \delta N$, is evaluated by the Poisson error, i.e., $\delta N/N = 1/\sqrt{N}$. The red (blue) color represents the event number with (without) collective neutrino oscillations, respectively. Naively, one may expect that these two scenarios can be distinguished since their difference is larger than the Poisson error. However, this neglects other sources of errors coming from our limited knowledge on the progenitor. For example, it is hard to know the detailed structure of the stellar core in reality, which strongly affects the neutrino luminosity [155, 210]. And if the explosion happen in our galaxy, the evaluation of its distance is oftentimes difficult. The distance to the supernova can easily change the neutrino number flux [211]. These uncertainties can be larger than the difference between with and without collective neutrino oscillations. While it may be difficult to show the existence of collective neutrino oscillations based solely on the event number, there is another way to circumvent much of the additional systematic uncertainties. To see the effect

of collective neutrino oscillations, we define the hardness ratio [212]:

$$R_{\mathrm{H/L}} = \frac{N_{E_c<E}}{N_{E<E_c}}, \tag{4.26}$$

where $N_{E_c<E}$ and $N_{E<E_c}$ are event numbers whose neutrino energy is above E_c and below E_c, respectively. This ratio is sensitive to the neutrino average energy and not sensitive to the integrated flux. That means the error from the stellar structure and distance of the source does not strongly affect the ratio. The error of the ratio is given by the following equation:

$$\begin{aligned} \delta R_{\mathrm{H/L}}/R_{\mathrm{H/L}} &= \frac{\delta N_{E_c<E}}{N_{E_c<E}} + \frac{\delta N_{E<E_c}}{N_{E<E_c}} \\ &= \frac{1}{\sqrt{N_{E_c<E}}} + \frac{1}{\sqrt{N_{E<E_c}}}. \end{aligned} \tag{4.27}$$

The statistical error is linearly increasing with the source distance d because of the radial dependence of the event number $N \propto d^{-2}$.

In inverted mass hierarchy, the evolution of the hardness ratio with $E_c = 20$ MeV is shown in the top panel of Fig.4.11 in dotted lines (the right axis). The blue dotted line corresponds to the ratio without collective neutrino oscillations. The $\bar{\nu}_e$ spectrum on the earth $f^{(\mathrm{f})}_{\bar{\nu}_e}$ is exactly the same as $f^{(\mathrm{o})}_{\bar{\nu}_X}$ due to the MSW H-resonance as shown in Fig.4.10. The red dotted line shows the result considering the non-linear phenomena of collective neutrino oscillations. Owing to the spectral swap caused by collective neutrino oscillations, some fraction of $f^{(\mathrm{o})}_{\bar{\nu}_e}$ remains in the final spectrum $f^{(\mathrm{f})}_{\bar{\nu}_e}$. Compare to the case without neutrino self interactions, the spectrum with collective neutrino oscillations becomes softer as shown in Fig.4.10 since the average energy of the original $\bar{\nu}_e$ is lower than that of the original ν_X. When collective neutrino oscillations happens, the hardness ratio suddenly becomes smaller. Especially, a reduction of the hardness ratio is prominent at 81 ms. Such softened hardness ratio is favorable to distinguish the case with/without collective neutrino oscillations since the hardness ratio naturally tends to increase as time goes by. The latter trend is seen in the blue dotted line in the top panel of Fig.4.11. During this phase, the proto-neutron star is shrinking. Then the neutrino spectrum naturally evolves to become hard as the

neutrinosphere becomes smaller and the effective temperature becomes higher. Since the effect of collective neutrino oscillations is the opposite of this generic trend, it can be easily identified. The error bar of the hardness ratio at 15 kpc source is less than the difference between the models with and without collective neutrino oscillations. We can distinguish the two models even if we take the 1σ Poisson error into account. The error of the hardness ratio in Eq.(4.27) is smaller as the event number becomes larger. The reduction of $R_{\rm H/L}$ in early explosion phase before 181 ms is suitable for the detection of collective neutrino oscillations because of the large event number owing to high neutrino number luminosity.

In normal mass hierarchy, the event rate and the hardness ratio with $E_c = 20$ MeV are shown in the middle panel of Fig.4.11. The flux of $\bar{\nu}_e$ on the earth is given by Eq.(4.14). An approximate equation of Eq.(4.14) is

$$f_{\bar{\nu}_e}^{(\rm f)} \sim (0.3 + 0.4\epsilon) f_{\bar{\nu}_e}^{(\rm o)} + (0.7 - 0.4\epsilon) f_{\bar{\nu}_X}^{(\rm o)}, \tag{4.28}$$

where ϵ is the survival probability of $\bar{\nu}_e$ just after collective neutrino oscillations (two flavor conversion between $e - x$ is assumed). The blue line corresponds to the case without collective neutrino oscillations, i.e., $\epsilon = 1$. In normal mass hierarchy, there is no matter resonance in antineutrino sector (see the upper panel of Fig.4.9). Then, 70% of $\bar{\nu}_e$ survives on the earth after the adibatic flavor transitions in dense matter. As a result, $f_{\bar{\nu}_e}^{(\rm f)}$ is similar to $f_{\bar{\nu}_e}^{(\rm o)}$ and the hardness ratio becomes soft. On the other hand, the hardness ratio of $\bar{\nu}_e$ considering collective neutrino oscillations becomes hard as shown in the red dotted line. The value of survival probability ϵ can be seen in the bottom panel of Fig.4.3. The finite $e - x$ conversion reduces the value of ϵ, which results in the large contribution of hard spectrum $f_{\bar{\nu}_X}^{(\rm o)}$ in $f_{\bar{\nu}_e}^{(\rm f)}$. As a result, the hardness ratio becomes higher. At the onsets of collective neutrino oscillations around 81 ms and 281 ms, we can confirm rapid rise of the hardness ratio, but the values of hardness ratios are naturally increasing irrespective of collective neutrino oscillations. Therefore, harder $R_{\rm H/L}$ is not necessarily convenient to distinguish the effect of collective neutrino oscillations. We note that the hardness ratio with neutrino self interaction (red dotted line) is decreasing in the region of $131 - 181$ ms due to the multiangle matter suppression in dense ejecta. Such softened trend could

be detected in 3σ level within the statistical error of Eq.(4.27) by assuming a small source distance less than 2 kpc.

The value of the hardness ratio depends on the detector. The event rate and the hardness ratio of JUNO are given in the bottom panel of Fig.4.11. Here, the inverted mass hierarchy is assumed. Since the energy threshold of JUNO (1.8 MeV) is lower than that of HK (8.3 MeV), JUNO can capture low energy neutrinos. Therefore, the value of the hardness ratio becomes low compared to that of HK. However, the overall feature is not so different because the main signal for $\bar{\nu}_e$ detection in liquid scintillator also comes from the inverse beta decay. Due to the small volume of JUNO, the statistical error of $R_{\mathrm{H/L}}$ becomes large. The source distance should be less than some 5 kpc to distinguish the effect of collective neutrino oscillations. We use Eq.(4.24) to evaluate the event number assuming 20 kton detector [37]. First we estimate the event rate in KamLAND and later multiply a factor coming from the volume difference of 20/0.7 to obtain the rate in JUNO. The number of target proton in KamLAND, N_{tar}, is 5.98×10^{31} for each 0.7 kton, fiducial volume [213]. It should be noted that KamLAND detector uses dodekan as the target particle, so that the density and mass ratio for H_2O cannot be applied in Eq.(4.24). We employ the same cross section of inverse beta decay, but the energy threshold is 1.8 MeV.

4.2.7 Detection Property of ν_e

Collective neutrino oscillations have influence on not only a spectrum of electron antineutrinos but also a spectrum of electron type neutrinos. Although it is difficult to detect larger numbers of clean ν_e with detectors currently in operation, the future large-volume liquid argon detector, DUNE, is expected to change this situation. DUNE is the primary detector with an expected high-statistics, clean ν_e signal [38].

In analogy with §4.2.6, we estimate the event number in 50 ms bins and the hardness ratio with $E_c = 15$ MeV in DUNE detector as shown in Fig.4.12. We use the cross section of the primary charge-current interaction on liquid argon, $\nu_e + {}^{40}\mathrm{Ar} \rightarrow e^- + {}^{40}\mathrm{K}^*$ based on the random phase approximation scheme of Ref. [214]. The event rates due

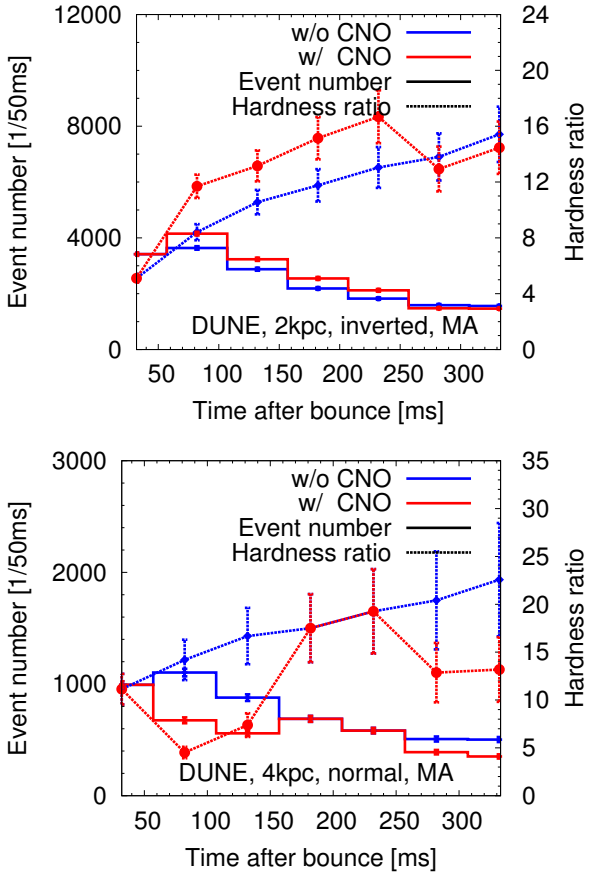

Figure 4.12: Event number and hardness ratio in 50 ms bins, both for ν_e detected by DUNE. Top: the case of inverted mass hierarchy and a source distance of 2 kpc. Bottom: the case of normal mass hierarchy and a source distance of 4 kpc. Here, we employ $E_c = 15$ MeV.

to this reaction are estimated by using Eq.(4.24). The number of target liquid argon is evaluated by adopting 40 kton as the total fiducial volume of the detector. The detection threshold of ν_e is set to 5 MeV. For simplicity, we assume a detection efficiency of 100%. The true threshold and efficiency remain to be determined. In reality, the supernova neutrino's low energy means that the interaction products may only leave stub-like tracks and blips in the liquid argon time-projection chamber; also, the signal may be vulnerable to radioactive and cosmogenic backgrounds [215]. More work is ongoing to understand the efficiency as a function of detector configuration. The statistical error of the hardness ratio is given by Eq.(4.27).

In normal mass hierarchy (bottom panel of Fig.4.12), the event number decreases and the hardness ratio becomes soft owing to the spectral swap of ν_e caused by collective neutrino oscillations. Such softening hardness ratio of ν_e is suitable to distinguish the contribution of collective neutrino oscillations. In normal mass hierarchy, there is the H resonance in neutrino sector as shown in the top panel of Fig.4.9. Collective neutrino oscillations make the spectrum of ν_e hard. However, the H resonance in neutrino sector cancels the spectral swap caused by collective neutrino oscillations. Fig.4.13 shows the example of ν_e fluxes on the earth by using the time snapshot at 81 ms post bounce in normal mass hierarchy. There is a single energy split around 5 MeV in the model considering neutrino self interactions (red solid line), so that the significant spectral swap occurs during collective neutrino oscillations in the region of $E > 5$ MeV. We confirm soft (hard) ν_e spectrum in the model with (without) collective neutrino oscillations, respectively. In such early explosion phase, $e-x$ conversion occurs dominantly and ν_y is decoupled from the flavor mixing in normal mass hierarchy. Therefore, the electron neutrino spectrum of the earth is roughly given by

$$f_{\nu_e}^{(\mathrm{f})} \sim (0.7 - 0.7\epsilon) f_{\nu_e}^{(\mathrm{o})} + (0.3 + 0.7\epsilon) f_{\nu_X}^{(\mathrm{o})}, \tag{4.29}$$

where Eq.(4.13) is used and ϵ is the survival probability in $e-x$ sector just after collective neutrino oscillations. The finite flavor mixing ($\epsilon < 1$) reduces the contribution of hard spectrum $f_{\nu_X}^{(\mathrm{o})}$ in the final spectrum $f_{\nu_e}^{(\mathrm{f})}$. The $e-x$ conversions are easily disturbed by multiangle matter effects, so that flavor conversions are negligible once the amount of mass ejection from the proto-neutron star increases. Such multiangle matter suppression will be observed by correspondence of two hardness ratios during $181 - 231$ ms as shown in the bottom panel of Fig.4.12. Since the amplitude of this softening is large compared to the error bar of the hardness ratio, the statistical errors remain smaller than the model difference if the source distance is set to $d = 4$ kpc. Especially, the significant reduction of the hardness ratio at 81 ms post bounce can be distinguished even within 10 kpc.

In inverted mass hierarchy (top panel of Fig.4.12), the value of hardness ratio considering collective neutrino oscillations (red) is increasing up to 231 ms post bounce.

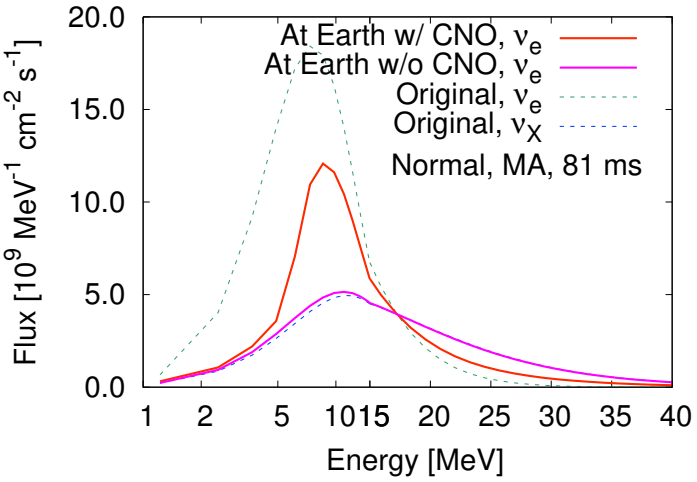

Figure 4.13: Same to Fig.4.10 but for ν_e spectra in normal mass hierarchy at 81 ms post bounce. The source distance is set to 10 kpc.

Such harder trend is similar to that of the middle panel of Fig.4.11. In both cases, there is no H resonance which strongly affects spectra of e-type neutrinos. Therefore, hard neutrino spectra after collective neutrino oscillations are maintained on the earth. Within the two flavor mixing before 231 ms, such relation between ν_e in inverted mass hierarchy and $\bar{\nu}_e$ in normal mass hierarchy is clearly seen. However, the situation is different if three flavor mixing is dominant. In the later explosion phase, such as 331 and 381 ms, $x-y$ mixing after $e-y$ conversion as shown in bottom panel of Fig.4.5 occurs actively in the neutrino sector. Such prominent three flavor mixing makes the hardness ratio of ν_e small in inverted mass hierarchy. This behavior can be explained by considering the survival probability η in the $x-y$ conversions. The final ν_e flux on Earth is written as

$$\begin{aligned} f_{\nu_e}^{(\mathrm{f})} \sim & [0.3\epsilon + 0.7(1-\eta)(1-\epsilon)] f_{\nu_e}^{(\mathrm{o})} \\ & + [1.0 - 0.3\epsilon - 0.7(1-\eta)(1-\epsilon)] f_{\nu_X}^{(\mathrm{o})}, \end{aligned} \tag{4.30}$$

where the two flavor conversions in $e-y$ sector before 231 ms post bounce are described by the limit of $\eta \to 1$. As shown in Eq.(4.30), three flavor mixing ($0 \leq \eta < 1$) increases the fraction of original ν_e which prevents hard ν_e spectrum on the earth.

To make the error bar of the hardness ratio smaller than the model difference, the source distance should be less than ~ 2 kpc.

4.2.8 Synergistic observation

We summarize influence of collective neutrino oscillations on the hardness ratio of neutrino detectors in Table 4.1. In inverted mass hierarchy, the spectrum of $\bar{\nu}_e$ becomes soft because of both collective neutrino oscillations and the MSW H resonance (see the second column of the second row). On the other hand, the spectrum of ν_e is hard before 231 ms when the two flavor conversions in $e - y$ sector occurs dominantly. This early ν_e spectrum contains large amount of original hard spectra of ν_X. In the later explosion phase > 281 ms, however, non-linear three flavor mixing enhances the fraction of original ν_e, which results in soft spectrum (see second column of the third row). To warn of this complicated behavior, we add a * mark in the table.

In normal mass hierarchy, the effect of collective neutrino oscillations on the hardness ratio becomes almost opposite as that in inverted mass hierarchy. Namely, the hardness ratio of ν_e ($\bar{\nu}_e$) becomes soft (hard) in normal mass hierarchy as shown in the last column of Table 4.1. In both neutrino mass hierarchy, neutrino spectra become harder owing to the spectral swap caused by collective neutrino oscillations. Therefore, the opposite behavior of the hardness ratio comes from the hierarchy dependence of MSW resonances in outer layers. Especially, the MSW H resonance has crucial for the soft neutrino spectrum on the earth.

Interestingly, the behavior of the hardness ratio is opposite depending on the neutrino mass hierarchy. This means synergistic observations of $\bar{\nu}_e$ and ν_e would be valuable to look for the occurrence of collective neutrino oscillations. In this respect, the result from HK (or JUNO) and DUNE will complement each other very strongly. The horizon for joint observation appears to be slightly smaller than 4 kpc. For example, DUNE may capture the onset of collective neutrino oscillations in inverted mass hierarchy for sources closer than ~ 2 kpc (see top panel of Fig. 4.12).

	Inverted	Normal
$\bar{\nu}_e$ spectrum	Soft	Hard
ν_e spectrum	Hard*	Soft

Table 4.1: Summary of the effect of collective neutrino oscillations (CNO) on the hardness ratio observed in neutrino detectors. See text for the meaning of $*$.

4.3 Summary and discussion

We carry out three flavor multiangle simulations by using simulation data of electron capture supernova whose progenitor mass is $8.8M_\odot$. Collective neutrino oscillations happen after 81 ms post bounce because of the dilute envelope of the progenitor. Such an early emergence of flavor transitions would be negligible in more massive progenitor such as $18M_\odot$ supernova model [80]. In multiangle simulations, collective neutrino oscillations are sensitive to the matter profile because of the angular dispersion in the right hand side of Eq.(4.9). The multiangle matter suppression [65] is well confirmed in Figs.4.7 and 4.8. The energy splits as shown in the single angle calculations are smeared out in the multiangle simulations. In inverted mass hierarchy, the $e-y$ conversions occur actively and subsequent $e-x$ conversions follow. Such behavior of non-linear flavor transitions are well confirmed in three flavor simulations [66, 71, 72, 80]. However, the dominant $e-x$ conversions in normal mass hierarchy are not found in these previous studies. The finite mixing angle θ_{13} which satisfies Eq.(4.8) would be necessary for the active $e-x$ conversions in normal mass hierarchy. Ref. [207] also derives a condition equivalent to Eq.(4.8) in the context of the linear stability analysis. As implied in Figs.4.3 and 4.4, the $e-x$ conversions are fragile in dense matter profile outside the neutrino sphere. Therefore, the $e-x$ conversions in normal mass hierarchy could be one of the specific signals of light mass progenitor supernova such as electron capture supernovae.

We study behavior of collective neutrino oscillations and their impacts on the neutrino detection in future neutrino facilities such as Hyper-Kamiokande (HK), JUNO, and DUNE. The hardness ratio of the observed neutrino spectra that we define in Eq.(4.26) can trace the appearance of collective neutrino oscillations. Especially, softened hardness ratio is favorable for the detection of collecticve neutrino oscillations

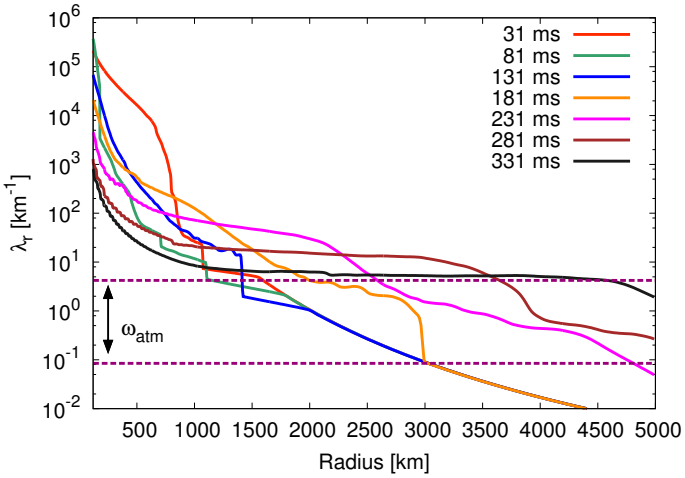

Figure 4.14: The radial profiles of $\lambda_r = \sqrt{2}G_F n_e(r)$ at different times and the region of $\omega_{\rm atm} = |\Delta m^2_{32}|/2E$ for E [MeV] $\in [1.2, 60]$. The MSW H resonance occurs when the matter profile λ_r enters the band of $\omega_{\rm atm}$.

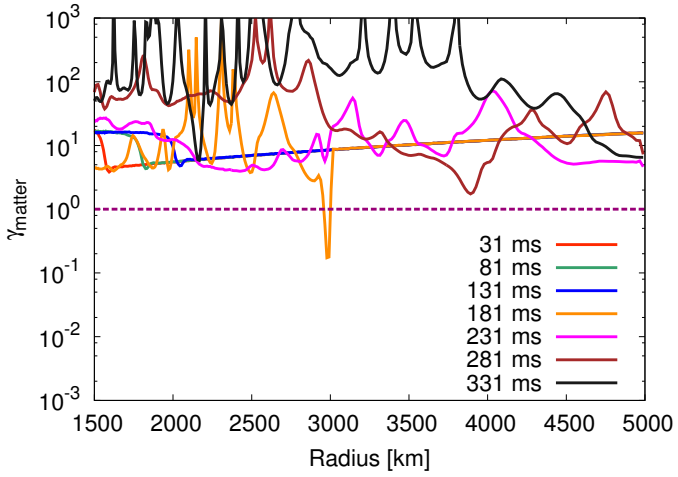

Figure 4.15: The radial profiles of the gamma factor $\gamma_{\rm matter}$ at different times. The definition of $\gamma_{\rm matter}$ is given in Eq.(2.72). Here, we impose a neutrino energy $E = 60$ MeV and mixing parameters of the H resonance: $(\Delta m^2, \theta) = (\Delta m^2_{32}, \theta_{13})$.

because the hardness ratio is naturally increasing without collective neutrino oscillations as the explosion time has passed owing to the shrink of proto-neutron star. In inverted mass hierarchy, the spectrum of $\bar{\nu}_e$ becomes soft owing to the combinations of collective neutrino oscillations and MSW matter resonances, which results in the reduction of hardness ratio. HK can distinguish this effect within the 1σ Poisson error if the source distance is smaller than 15 kpc. In normal mass hierarchy, on the other hand, the spectrum of ν_e becomes soft due to the collective neutrino oscillations and MSW matter resonances. DUNE can distinguish this effect when the supernova occurs within a distance of ~ 4 kpc. The reduction of hardness ratio around 100 ms can be detected even if the source distance is extended up to 10 kpc. If the spectrum of $\bar{\nu}_e$ becomes softer, the spectrum of ν_e becomes harder (and vice versa) as shown in the Table 4.1. This provides a synergistic opportunity to combine the $\bar{\nu}_e$ and ν_e from HK and DUNE as a valuable method to test the occurrence of collective neutrino oscillations.

Neutrino spectra after collective neutrino oscillations are affected by MSW matter resonances in outer layers. Here, we estimate neutrino flux on the earth by using analytical treatment of MSW resonances assuming adiabatic flavor transitions at resonances. Especially, the H resonance makes neutrino spectra soft, which results in the reduction of hardness ratio. In reality, however, adiabatic flavor transitions can be violated in steep density gradient of progenitor [183] or the density jump in the shock front [182, 184, 185]. Fig.4.14 shows radial profiles of $\lambda_r = \sqrt{2}G_F n_e(r)$ at different times and the region of $\omega_{\rm atm} = |\Delta m^2_{32}|/2E$. The H resonance happens when $\lambda_r \sim \omega_{\rm atm}$ is satisfied. In Fig.4.14, we can confirm that the position of the shock front propagates outwards as the explosion time has passed. The adiabaticity of the H resonance can be violated when the shock front stays in the band of $\omega_{\rm atm}$. In our explosion model, such violation of adiabaticity could be evident around 181 ms post bounce. Fig.4.15 shows radial profiles of the gamma factor $\gamma_{\rm matter}$ (see Eq.(2.72)) of the H resonance. In the radial profile at 181 ms, we can confirm the significant reduction of $\gamma_{\rm matter}$ around $r = 3000$ km which corresponds to the position of the shock front as shown in Fig.4.14. The adiabaticity can be broken when the gamma factor is smaller than unity: $\gamma_{\rm matter} < 1$. The violation of adiabaticity at MSW resonances

makes the hardness ratio of $\bar{\nu}_e(\nu_e)$ soft without collective neutrino oscillations in inverted (normal) mass hierarchy, respectively. However, the hardness ratio of $\nu_e(\bar{\nu}_e)$ in inverted (normal) mass hierarchy does not change in such nonadiabatic matter effect. Therefore, there is no correlation between the hardness ratio of $\bar{\nu}_e$ and that of ν_e as shown in Table 4.1. It seems that the reduction of hardness ratio caused by the violation of adiabaticity at MSW resonances can be distinguished from the contribution of collective neutrino oscillations by combining HK (or JUNO) with DUNE. Furthermore, we remark that the assumption of adiabaticity at MSW resonances for energetic neutrinos ($E > 3$ MeV) is valid for flavor transitions before 131 ms and after 231 ms post bounce. Especially, the reduction of hardness ratio caused by collective neutrino oscillations is significant in early explosion phase before 131 ms, so that the effect of collective neutrino oscillations can be distinguished before 131 ms irrespective of the uncertainty of the MSW resonances.

We remark several limitations in this study. First, we finished our hydrodynamic simulations at 331 ms after bounce, since the density of the envelope becomes too low and protrudes the region of our tabulated EoS. Due to that, we cannot investigate how long these non-linear flavor conversions continue. Second, we employ the single-bulb model [58] and uses a fixed neutrino sphere radius of $R = 30$ km irrespective of the post bounce time. We should keep in mind that, originally, the neutrino sphere radius depends on the explosion time as well as neutrino energy and neutrino species. Further study is required to consider all of these effects even though some previous works [165, 170] employ a multi-bulb model which incorporates the flavor dependence in the neutrino sphere. Finally, we ignore the instability of non-linear flavor transitions such as the multi-azimuthal-angle (MAA) instability [77–79, 163, 164] and fast flavor conversions [165–170] which associate with angular dependence of neutrinos. The MAA instability in normal mass hierarchy appears in electron capture supernovae [79] but such flavor conversions occur in the $e - y$ sector which is characterized by $(\Delta m^2_{32}, \theta_{13})$. Therefore, it seems that $e-x$ conversions in normal mass hierarchy would not be canceled by the MAA instability. Various linear stability analyses imply the possibility of fast flavor conversions which occur in the length scale of $(G_F n_\nu)^{-1} \sim$ cm, but the absolute proof of fast flavor conversions has not been found yet in numerical

studies. If fast flavor conversions would be prominent, active flavor mixing happened near the neutrino sphere, which might result in an equilibrium state of any non-linear flavor conversion: $\rho_{\alpha\alpha} = \bar{\rho}_{\alpha\alpha} = 1/3$ ($\alpha = e, x, y$). Such complete flavor mixing also reduces the value of hardness ratio of $\bar{\nu}_e$ (ν_e) in inverted (normal) mass hierarchy, respectively. Therefore, our finding may not change qualitatively irrespective of fast flavor conversions even though more developed numerical study is necessary to draw a robust conclusion.

Chapter 5

The enhanced νp process nucleosynthesis caused by collective neutrino oscillations

Heavy elements are synthesized inside core-collapse supernovae. The νp-process nucleosynthesis creates abundant p-nuclei in proton rich neutrino driven winds. The free neutrons produced through $p(\bar{\nu}_e, e^+)n$ trigger the νp-process. The reaction rate of $p(\bar{\nu}_e, e^+)n$ is enhanced by large amount of energetic electron antineutrinos, so that collective neutrino oscillations can affect the νp-process. The simple analytical spectral swap model is applied to the νp-process in Ref. [216], but more sophisticated numerical treatment is necessary for precise oscillation effects on abundances of p-nuclei. In this chapter, we apply the three flavor multiangle simulation to the nuclear network calculation in proton rich neutrino driven winds. Then, we show how collective neutrino oscillations can enhance the νp-process nucleosynthesis. Here, we review the content of our previous work [82]. Furthermore, we also discuss the contribution of a reverse shock on the νp-process which is not taken into account in Ref. [82].

5.1 Overview of nucleosynthesis inside core-collapse supernovae

Many layers of heavy elements are formed inside a star through nuclear fusion reactions during the stellar evolution. In a final stage of a massive star $M > 10M_{\odot}$, an iron core is produced at the center of the star. Nucleosynthesis has stopped up to iron group elements because nuclear binding energy per nucleon becomes maximum around ^{56}Fe. After the gravitational core-collapse, the core-bounce occurs inside the iron core and subsequent shock waves propagate outwards from the iron core depositing their energies into the outer material. The temperature of the material is enhanced once the shock waves pass through it, which induces the production of heavy elements. Nucleosyntesis in core-collapse supernovae is mainly divided by two parts.

5.1.1 Explosive nucleosynthesis in outer layers

The first part is the "explosive nucleosynthesis" in outer layers of the progenitor such as Si, O-Ne-Mg and C layers [217, 218]. Fig.5.1 represents the mass fraction of element X_i against the enclosed mass M_r after an explosive nucleosynthesis [219]. The progenitor belongs to population (Pop) III stars which are metal poor stars in the early universe. The mass of progenitor is $25M_{\odot}$ and the explosion energy (kinetic energy of the ejecta) is $E_{\rm exp} = 10^{51}$ erg. After the shock heating, the material becomes the radiation dominant because of the high temperature. In such radiation dominant region, the explosive energy is described by the radius r and the temperature T:

$$E_{\rm exp} \sim \frac{4\pi}{3} r^3 a T^4, \tag{5.1}$$

where a is the radiation constant. Therefore, T is higher in smaller r if the explosion energy is fixed. The temperature of the innermost layer is higher than 5×10^9 K, so that the Si burning has completed and iron group elements such as Ni, Zn and Co are synthesized. ^{56}Ni is the main product of the complete Si burning because of the stability of double magic nuclei: $Z = N = 28$. One of the energy sources of

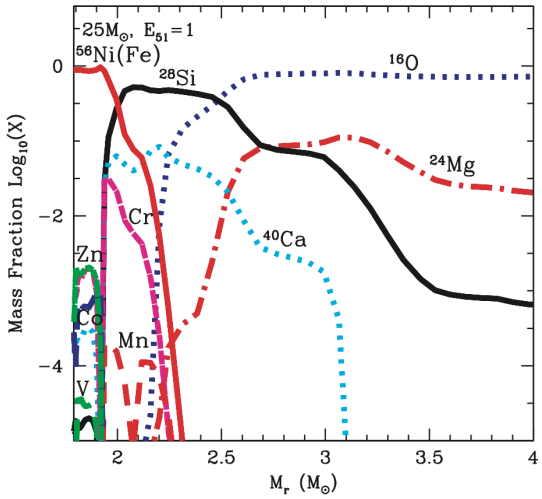

Figure 5.1: Explosive nucleosynthesis in $25M_{\odot}$ progenitor model [219]. The material which finally accretes to the central object is removed by mass cut.

supernova light curve is positrons and gamma rays produced by radioactive decays of ^{56}Ni $\rightarrow^{56}$Co $\rightarrow^{56}$Fe. Especially, the long half-life of ^{56}Co (77 days) accounts for the decline shape of the light curve [220]. The temperature T is decreasing in large radius R (large enclosed mass M_r) where incomplete Si burning and explosive O-Ne-C burning occur depending of their sensitive temperatures [218]. Heavier elements are produced abundantly deep inside of the star because high temperature is necessary for incident nuclei to penetrate Coulomb barriers in nuclear fusion reactions. The abundance pattern and the amount of heavy elements depend on the explosion energy [219, 221]. The explosion energy and the ejected ^{56}Ni mass can be estimated by observations of the light curve, which are useful to clarify the diversity of supernovae explosion [222].

5.1.2 Weak r-process and νp process inside neutrino driven winds

The second part is nucleosynthesis inside neutrino driven winds which are stripped from a proto-neutron star powered by neutrino heating. This nucleosynthesis occurs inside the iron core of the progenitor. Fig.5.2 shows example of wind trajectories

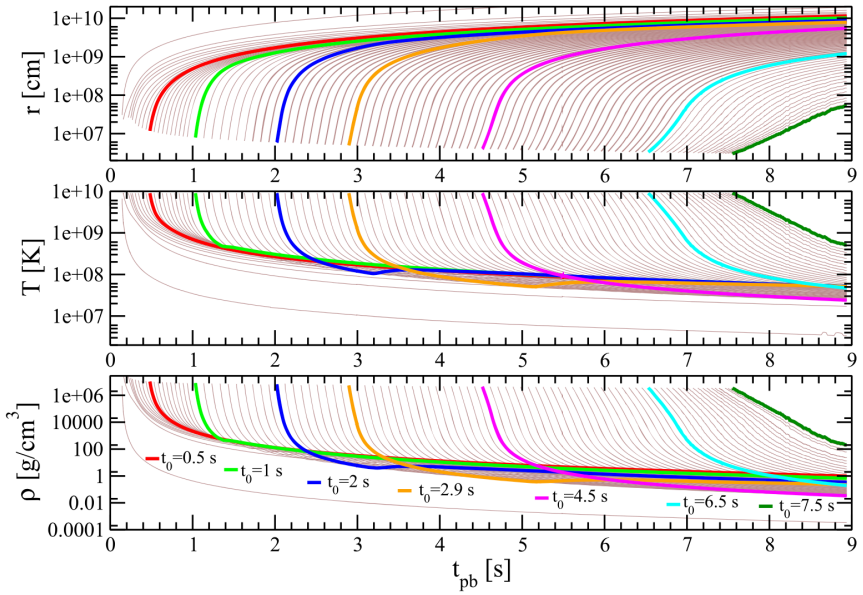

Figure 5.2: Trajectories of neutrino driven winds [223]. The radius r, temperature T and the density ρ of each trajectory are functions of post-bounce time t_{pb}.

obtained by a supernova explosion simulation [223]. Temperature and density of neutrino driven winds are decreasing during the expansion. Near the proto-neutron star, all of nuclei are decomposed by nucleons because of the high temperature $T > 10^{10}$ K. As the temperature decreases, however, ^{4}He (α-particle) and small amount of heavy elements are synthesized through nuclear fusion reactions. Within the hot gas ($T > 5 \times 10^9$ K), nuclear fusions and decompositions are balanced, so that all of nuclei are in Nuclear Statistical Equilibrium (NSE) where abundances of nuclei are parametrized by baryon density ρ, temperature T and electron fraction Y_e which represents the ratio of protons inside nuclei. In lower temperature, Coulomb barriers prevent the penetration of α-particle in α capture reactions. Then, nuclear abundances no longer follow NSE and large amounts of α-particle are out of nucleosynthesis. This is called "α-rich freeze-out" [224]. As the temperature decreases down to $\sim 1.5 \times 10^9$ K, all capture reactions of charged particles have terminated because of strong Coulomb barriers. Then, neutron captures and β decays are dominant in lower temperature region $T < 1.5 \times 10^9$ K.

In the past, the neutrino driven wind is regarded as main astrophysical site for r-process nucleosynthesis [143,224–226]. The r-process nucleosynthesis is rapid neutron capture process where the time scales of neutron capture reactions are much smaller than that of β decays. Heavy elements whose mass number A is larger than 200 are produced in the r-process. The specification of astrophysical sites for r-process has important role to reveal the origin of heavy elements such as Eu, Pt and Au in our solar system. One of the necessary conditions for r-process nucleosynthesis is a low electron fraction Y_e [226–228], which means abundant free neutrons inside neutrino driven winds. However, neutrino driven winds tend to be proton-rich $Y_e > 0.5$ in more sophisticated neutrino transport [200, 229–231]. The difference between mean energy of ν_e and that of $\bar{\nu}_e$ becomes smaller in the updated neutrino transport because of neutrino inelastic scatterings with nucleons and neutrino scattering themselves. Such small energy difference increases the value of Y_e [143, 200]. Therefore, in standard core-collapse supernovae, it seems that heavy elements are synthesized up to $A \sim 100$ through weak r-process [85] even if neutrino driven winds are neutron-rich $Y_e < 0.5$. Fig.5.3 shows abundance patterns of nuclei inside neutrino driven winds. The dots are observational data of r-process elements in our solar system. Color solid lines are simulation results of abundance patterns in different masses of central objects. The third peak nuclei ($A \sim 200$) are synthesized if the mass is larger than $2.2M_\odot$ because of small dynamical time scale $\tau \sim 20$ ms and large entropy per nucleon $S \sim 230\ k_{\rm B}$ [228]. However, nuclear flow can not reach the third peak in the case of standard mass 1.4 $M_\odot$, which implies neutrino driven winds in delayed explosion scenario are not main astrophysical sites for heavy r-process elements ($A > 200$). The neutrino absorption reaction $n(\nu_e, e^-)p$ prevents r-process nucleosynthesis inside neutrino driven winds even though it helps revival of stalled shock waves. Heavy r-process elements can be produced in some special type of supernova explosion such as magneto-rotational driven core-collapse supernovae [85, 152, 232] because the explosion energy is not mainly supplied by neutrino-heating. Neutron star mergers are another promising candidate for main r-process site [233] because of the neutron-rich environment and abundant ejection of heavy elements even though the event rate is smaller than that of core-collapse supernovae. After the detection of gravitational waves from neutron star mergers: GW170817 [234], the optical and near-infrared

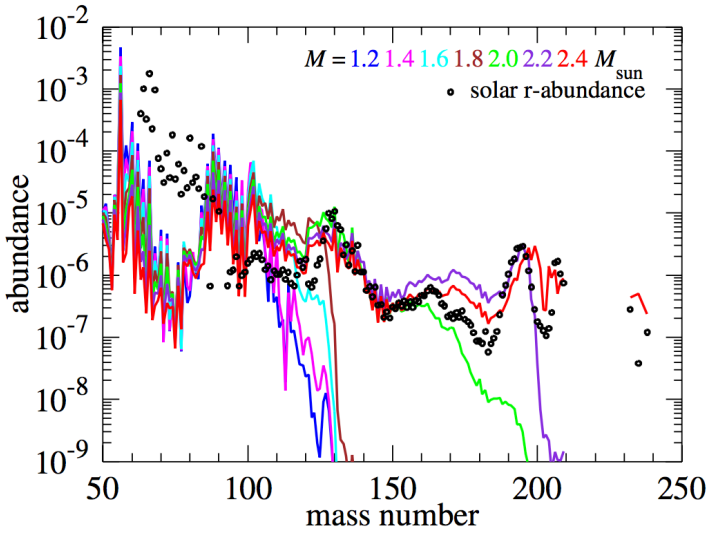

Figure 5.3: Solid lines represent abundance patterns in neutrino driven winds [228]. Circles show observational data of solar abundances. Heavy r-process elements (mass number$>$ 200) are not produced if the mass of proto-neutron star M takes standard value ($1.4M_{\odot}$).

emission AT2017gfo (SSS17a) was observed [235, 236]. This electromagnetic counterpart is called "kilonova" [237] which is powered by radioactive r-process elements. The light curves of AT2017gfo are explained by the ejecta of $0.03M_{\odot}$ containing lanthanide elements [238].

Instead of r-process nucleosynthesis, νp-process nucleosynthesis [86–88] is induced by free neutrons produced through $p(\bar{\nu}_e, e^+)n$ interactions in proton rich outflows ($Y_e > 0.5$). These free neutrons enables (n, p) reactions on the waiting point nucleus ^{64}Ge such as ^{64}Ge(n, p)^{64}Ga instead of β^+ decay, which promotes synthesis of heavier elements than ^{64}Ge. The νp-process induces creation of heavy elements in proton rich region toward the β stability line. Such isotopes are called p-nuclei [239, 240] which are not synthesized through neutron capture processes in neutron rich environment. The photodisintegration reactions in explosive nucleosynthesis (γ-process) [241, 242] explain solar abundances of p-nuclei except for lighter p-elements such as ^{92,94}Mo and ^{96,98}Ru [241–246]. However, the νp-process inside neutrino driven winds supplies abundant lighter p-elements, which might resolve the underproduction of ^{92,94}Mo and ^{96,98}Ru [82, 216, 247–250].

The νp-process is induced by free neutrons supplied from the charged current reaction: $p(\bar{\nu}_e, e^+)n$. The flux of electron antineutrino is affected by collective neutrino oscillations outside the neutrino sphere $r \sim \mathcal{O}(100)$ km where the νp-process occurs actively inside neutrino driven winds. Therefore, the νp-process is sensitive to collective neutrino oscillations. Conversely, the abundances of p-nuclei might be useful tool to probe the appearance of collective neutrino oscillations in addition to direct observations of neutrino spectra.

Nucleosynthesis inside neutrino driven winds considering collective neutrino oscillations are studied in previous works [80, 216, 223, 251–253]. In neutron rich outflows, inaccurate prediction for the yields are given by collective neutrino oscillations under the single angle approximation [252]. This is because the onset of non-linear oscillations becomes earlier in the single angle approximation, which changes the value of electron fraction Y_e artificially. The multiangle calculation which takes into account angular dependences of neutrino fluxes is required for precise abundances of nuclei.

In proton rich outflows, Ref. [216] shows that the abundances of p-nuclei are enhanced if neutrino spectral swap as shown in Fig.3.9 are systematically included by hand. However, such simple scenario does not always occur in more complex three flavor multiangle simulations. A realistic calculation coupling collective neutrino oscillations with nuclear network calculations has not yet been done in proton rich outflows. Such numerical treatment is required for precise nuclear abundances because it is difficult to predict the onset of non-linear flavor transitions analytically. In the later part of this chapter, we discuss influence of collective neutrino oscillations on the νp-process by using realistic three flavor multiangle calculations together with nuclear network simulations based on a 1D supernova explosion model.

5.2 Numerical setup

We employ neutrino driven winds obtained in a 1D explosion simulation. The numerical setup of hydrodynamics and neutrino radiation are based on Ref. [194] except for the consideration of phenomenological general relativistic corrections on the gravitational potential [254]. The $40M_\odot$ progenitor model [132] is used as the initial matter profile for the explosion because of large neutrino luminosities and mean energies after core bounce in such a massive star, which helps an active νp-process nucleosynthesis inside neutrino driven winds. The mass of the iron core (final remnant) is $\sim 1.6(1.8)M_\odot$, respectively. These values are consistent with Fig.17 of Ref. [132]. The mass accretion rate is reduced by hand in order to obtain a successful shock revival in 1D explosion model as in Ref. [255]. Fig.5.4 shows the time evolution of neutrino luminosities, mean energies and pinching parameters (see the definition in Eq.(4.2)) in our explosion model. The sharp decrease of neutrino luminosities at $t = 250$ ms after bounce reflects the sudden reduction of the mass accretion rate. Basically, it corresponds to the arrival of Si layer to the shock. In this work, the accretion rate is reduced by hand and the shock revives at that time. In the late phase of the explosion, the mean energy of $\nu_\beta = (\nu_\mu, \nu_\tau, \bar{\nu}_\mu, \bar{\nu}_\tau)$ is higher than the value obtained in recent simulations, e.g. Refs. [230, 231] since inelastic scatterings of neutrinos with nucleons are not included in our simulation.

We simulate the effect of collective neutrino oscillations on nucleosynthesis as post processes by using two representative neutrino driven winds. We employ time snapshots of baryon density, temperature and outflow velocity at $t = 0.6$ and 1.1 s as the fiducial models of wind trajectories. The reverse shock in the time snapshot at $t = 0.6$ s is removed in our previous work [82]. In this thesis, however, we also discuss the contribution of such removed reverse shock on the νp-process nucleosynthesis. The hydrodynamic quantities in both with and without the reverse shock are shown in Fig.5.14. The electron fraction of the outflow is given by

$$Y_e = \sum_{i=\text{all species}} \frac{Z_i}{A_i} X_i, \tag{5.2}$$

where A_i, Z_i and X_i represent mass number, atomic number and mass fraction of

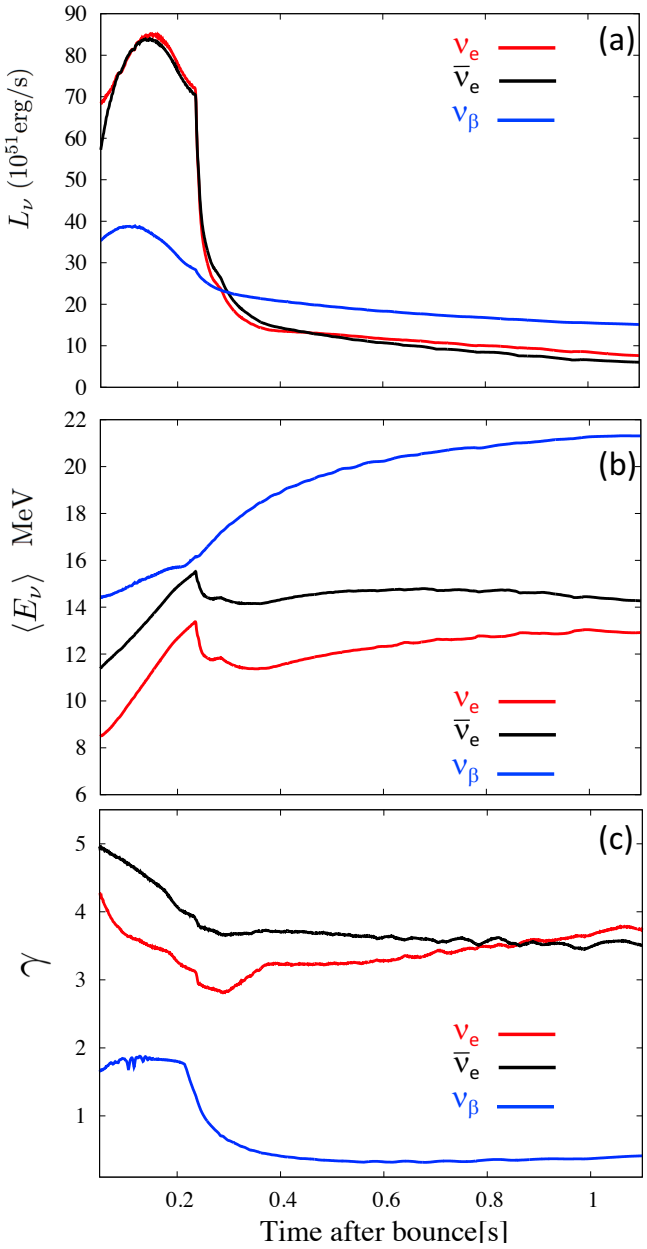

Figure 5.4: The time evolution of luminosities L_ν, mean energies $\langle E_\nu \rangle$ and pinching parameters γ of neutrinos in our 1D explosion model [82].

nucleus i, respectively. Here, the summation of X_i is normalized by unity:

$$\sum_{i=\text{all nuclei}} X_i = 1. \tag{5.3}$$

The mass of nucleus i inside ejecta is given by $M_{\text{ejecta}}X_i$ where M_{ejecta} is the ejecta mass. The value of Y_e is sensitive to neutrino absorbed reactions on free nucleons near the proto-neutron star where all of nuclei are decomposed by nucleons because of high temperature. However, the feedback effect of neutrino oscillations on the value of Y_e is negligible at $r > 100$ km for the following two reasons. At first, the outflow velocity is so fast that free nucleons inside the outflow do not have enough time to absorb much neutrinos. Secondly, few free nucleons are produced via $n(\nu_e, e^-)p$ and $p(\bar{\nu}_e, e^+)n$ at $r > 100$ km where large numbers of target free nucleons for these reactions are exhausted because of the α-particle creations. These two reasons indicate that collective neutrino oscillations which occur at $r > 100$ km in multiangle simulations can not change the value of Y_e significantly. Actually, in our models at $t = 0.6(1.1)$ s, the electron fraction takes almost the same constant value $Y_e \sim 0.55(0.58)$ at $r > 40$ km irrespective of neutrino oscillation effects. In multiangle simulations, collective neutrino oscillations start in outer region compared with the onset of flavor transitions in single angle approximation. Such delayed non-linear conversions in multiangle simulations are caused by the interplay between dispersion of neutrino self interactions and that of vacuum Hamiltonian [73]. This multiangle suppression makes critical deviations in nucleosynthesis in comparison to single angle calculations [252]. Earlier collective neutrino oscillations in the single angle calculation induce artificial feedback effects on Y_e. Therefore, three flavor multiangle simulations are necessary to study oscillation effects on nucleosynthesis precisely.

In the nuclear network calculation, nuclear abundances $Y_i = X_i/A$ inside neutrino driven winds are obtained by solving

$$v(r)\frac{\mathrm{d}}{\mathrm{d}r}Y_i = \sum_j \left(-\lambda^{(1)}_{j;i}Y_i + \lambda^{(1)}_{i;j}Y_j\right) + \sum_{jkl}\left(-\lambda^{(2)}_{kl;ij}\rho N_A Y_i Y_j + \lambda^{(2)}_{ij;kl}\rho N_A Y_k Y_l\right) + .., \tag{5.4}$$

where ρ and N_A are baryon density of the wind and Avogadro number, respectively.

Number density of nucleus i is written as $n_i = \rho N_A Y_i$. The matterial derivative D/Dt is replaced with $v(r)\mathrm{d}/\mathrm{d}r$ on the left hand side in Eq.(5.4) by assuming steady wind trajectories [143, 226, 256]. The coefficient $\lambda^{(1)}_{j;i}$ $[s^{-1}]$ represents the reaction rate of one-body reaction $(i \to j)$ such as β-decays, photodisintegration and neutrino absorptions on nucleus i. The $\lambda^{(1)}_{i;j}$ represents a rate of corresponding inverse reaction $(j \to i)$. In case of two-body interaction $(i + j \to k + l)$, the reaction rate $\lambda^{(2)}_{kl;ij}$ is derived by thermal average of $\sigma_{kl;ij} v_{ij}$ where $\sigma_{kl;ij}$ is the cross section and v_{ij} is the relative velocity between nucleus i and j. More higher order N-body nuclear reactions $(N \geq 3)$ are also included on the right hand side of Eq.(5.4). We should keep in mind that reaction rates of neutrino absorptions on nuclei are given by average of the cross sections using neutrino fluxes, so that neutrino oscillations have influence on nucleosynthesis by increasing values of reaction rates. In this work, we use the analytical cross sections of $\nu_e + n \to e^- + p$ and $\bar{\nu}_e + p \to e^+ + n$ [251]:

$$\sigma_{\nu_e} = 9.6 \times 10^{-44} \left(E/\mathrm{MeV} + 1.293\right)^2, \tag{5.5}$$

$$\sigma_{\bar{\nu}_e} = 9.6 \times 10^{-44} \left(E/\mathrm{MeV} - 1.293\right)^2, \tag{5.6}$$

respectively. Furthermore, we consider electron and positron captures on free nucleons [203] and neutrino-induced reactions on α-particles [257, 258] such as

$$\alpha + \nu \to {}^3\mathrm{H} + p + \nu', \tag{5.7}$$

$$\alpha + \nu \to {}^3\mathrm{He} + n + \nu', \tag{5.8}$$

$$\alpha + \nu \to 2\ {}^2\mathrm{H} + \nu', \tag{5.9}$$

$$\alpha + \nu \to 2n + 2p + \nu', \tag{5.10}$$

$$\alpha + \nu_e \to {}^3\mathrm{He} + p + e^-, \tag{5.11}$$

$$\alpha + \bar{\nu}_e \to {}^3\mathrm{H} + n + e^+, \tag{5.12}$$

$$\alpha + \nu_e \to {}^2\mathrm{H} + 2p + e^-, \tag{5.13}$$

$$\alpha + \bar{\nu}_e \to {}^2\mathrm{H} + 2n + e^+, \tag{5.14}$$

where the cross sections of above α-induced reactions are derived by the WBP Hamiltonian [259]. Free nucleons and light elements are supplied by these spallations. Especially, produced free neutrons contribute to the νp-process. Any flavor transitions do not affect Eqs.(5.7)-(5.10) because of neutral current reactions. On the other hand, Eqs.(5.11)-(5.14) are sensitive to neutrino oscillations because of charged current reactions. α-particles becomes dominant species inside neutrino driven winds after the temperature decreases down to $T \sim 6 \times 10^9$ K, so that such neutrino absorptions on α-particles are no longer negligible. We adopt data of other reaction rates on more than 8000 species from JINA Reaclib database [260]. Numerical simulations in neutrino driven winds are carried out by running LIBNUCNET reaction network engine [261]. The contribution from neutrino oscillations are taken into account in the network calculation successively.

We adopt following neutrino mixing parameters: $\theta_{12} = 34^{\rm o}$, $\theta_{13} = 8.5^{\rm o}$, $\theta_{23} = 45^{\rm o}$, $\Delta m^2_{21} = 7.5 \times 10^{-5}{\rm eV}^2$, $|\Delta m^2_{32}| = 2.4 \times 10^{-3}{\rm eV}^2$ and $\delta_{CP} = 0$. We employ the bulb model and the radius of neutrino sphere is set to the same value $R_\nu = 18$ km in both wind trajectories at $t = 0.6$ and 1.1 s. This assumption can be applied to our simulation because the onset radius of flavor instability [73] is not so sensitive to small differences by a few km in R_ν. We employ initial normalized neutrino spectrum $f_i(E)$ $(i = \nu_e, \bar{\nu}_e, \nu_\beta)$ as defined in Eq.(4.1). Table 5.1 represents values of initial neutrino parameters which characterize the normalized neutrino spectra and neutrino self interactions in Eq.(3.29). We carry out three flavor multiangle simulations by solving Eqs.(3.30) and (3.31) from $r = 40$ km. We neglect any flavor transitions between the neutrino sphere ($r = R_\nu$) to the beginning of oscillation simulation ($r = 40$ km) because of the dominant matter effects and delayed multiangle flavor transitions [72, 73, 252].

t (s)	L_{ν_e} (10^{51}erg/s)	$L_{\bar{\nu}_e}$ (10^{51}erg/s)	L_{ν_β} (10^{51}erg/s)	$\langle E_{\nu_e}\rangle$ (MeV)	$\langle E_{\bar{\nu}_e}\rangle$ (MeV)	$\langle E_{\nu_\beta}\rangle$ (MeV)	γ_{ν_e}	$\gamma_{\bar{\nu}_e}$	γ_{ν_β}
0.6	11.7	10.7	18.3	12.3	14.7	20.2	3.16	3.66	0.32
1.1	7.6	6.0	15.1	12.9	14.3	21.3	3.72	3.53	0.42

Table 5.1: The neutrino parameters on the surface of the neutrino sphere ($r = R_\nu$) where $\nu_\beta = \nu_\mu, \nu_\tau, \bar{\nu}_\mu, \bar{\nu}_\tau$.

5.3 Results

5.3.1 Later neutrino driven wind ($t = 1.1$ s)

We focus on numerical results of three flavor multiangle calculations and their effects on abundances of p-nuclei in the later wind model at $t = 1.1$ s rather than the early wind model at $t = 0.6$ s because of absence of the reverse shock effect [247, 248]. The reverse shock is formed when the supersonic outflow collides with slower preceding supernova ejecta [247]. Fig.5.5 represents the temperature profiles of two wind models. The decreasing temperature is raised up by the reverse shock around $r \sim 870(3500)$ km in the early (later) wind model, respectively. In the later wind model, we can ignore the contribution from the reverse shock for the νp-process nucleosynthesis because the temperature of subsonic region is lower than the temperature range of the νp-process ($1.5 - 3.0 \times 10^9$ K) [247]. In the early wind model, we discuss both contributions from neutrino oscillations and the reverse shock.

In proton-rich outflow, the νp-process is caused by $p(\bar{\nu}_e, e^+)n$, so that we focus how collective neutrino oscillations affect a spectrum of electron antineutrinos. Fig.5.6 shows the evolution of angular averaged ratio of $\bar{\nu}_e$ which is given by

$$\langle \bar{\rho}_{ee}(r, E) \rangle = \frac{2}{\pi} \int_0^{\frac{\pi}{2}} \mathrm{d}\theta_R \; \bar{\rho}_{ee}(r, E, \theta_p), \tag{5.15}$$

where θ_R is an emission angle as shown in Fig.3.5. The value of this quantity is conserved in case of no flavor transition. Collective neutrino oscillations induce flavor mixing among three neutrino flavors, which changes the value of Eq.(5.15) and the amount of $\bar{\nu}_e$ flux. We shows numerical results of collective neutrino oscillations in both normal and inverted mass hierarchies.

In normal hierarchy, non-linear flavor transitions are suppressed until $r \sim 110$ km because of high electron density and synchronized motion near the neutrino sphere as shown in Fig.3.7. Henceforth, the decreasing non-linear potential gradually becomes comparable to the atmospheric vacuum frequency $\omega_{\rm atm} = |\Delta m^2_{32}|/2E$, and then collective neutrino oscillations occur in $e - y$ sector without coupling the x type

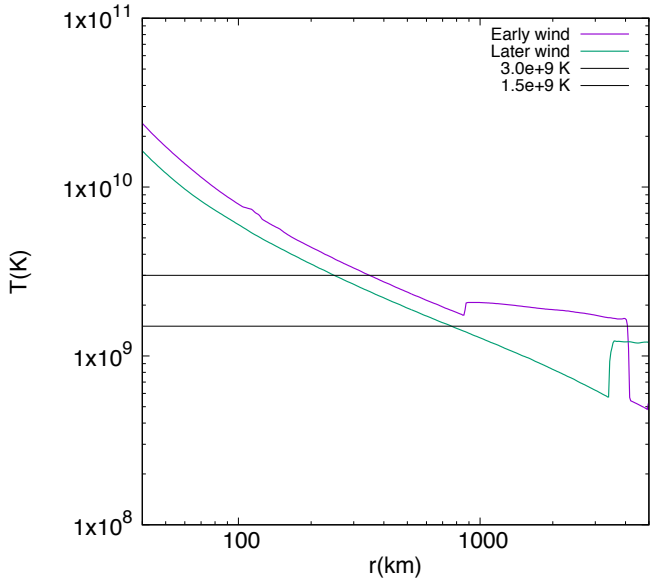

Figure 5.5: The temperature profiles of two wind models. Two black lines represent $T = 3.0 \times 10^9$ and 1.5×10^9 K which are boundaries of νp-process temperature range. The wind temperature is increased by the reverse shock around $r \sim 870(3500)$ km in the early (later) wind model, respectively.

neutrinos. In such $e-y$ conversions, the adiabaticity of flavor transitions in §3.8 is violated. The $e-y$ conversions in normal hierarchy are also confirmed numerically in previous works [67, 71, 73] where an order of neutrino flux $\Phi_i^0 = L_i/\langle E_i \rangle$ becomes $\Phi^0_{\bar{\nu}_e} \leq \Phi^0_{\nu_e} \leq \Phi^0_{\nu_\beta}$. This flux hierarchy is also satisfied in our later wind model: $\Phi^0_{\nu_e} : \Phi^0_{\bar{\nu}_e} : \Phi^0_{\nu_\beta} = 0.83 : 0.59 : 1$. After the onset around $r = 110$ km, flavor mixing is enhanced by collective neutrino oscillations but flavors of antineutrinos gradually come back to original ones. However, there is a sharp flavor conversion raising the flux of $\bar{\nu}_e$ around 280 km in high energy region as shown by the 30 MeV antineutrinos in Fig.5.6(a). Around $r \sim 400$ km, the contribution of neutrino self interactions in total Hamiltonian is much smaller than vacuum Hamiltonian and the electron matter potential, so that non-linear flavor transitions have terminated. Antineutrino spectra at $r = 400$ km are shown in Fig.5.7(b). The spectral swap occurs in high energy region $E > E^{(l)}_{c2} = 17.8$ MeV where $E^{(l)}_{c2}$ represents the second spectral crossing point of antineutrino specra in the later wind model. Such enhanced energetic $\bar{\nu}_e$ reflects the sharp flavor conversion around 280 km which results in significant influence on the νp-process nucleosynthesis. Complete spectral swaps as confirmed in the single angle calculations do not emerge in multiangle simulations. Such smeared oscillations in multiangle simulations are consistent with previous works [61, 72, 73]. The spectra of $\bar{\nu}_\mu$ and $\bar{\nu}_\tau$ are almost degenerate because of the two flavor conversions in $e-y$ sector. After the collective neutrino oscillations, the value of $\langle \bar{\rho}_{ee}(r, E) \rangle$ is increasing in low energy antineutrinos as shown by 1.8 MeV antineutrino in Fig.5.6(a) even though there is no MSW resonance of antineutrinos in normal mass hierarchy. As the electron density decreases, an adiabatic transition occurs from flavor eigenstates $(\bar{\nu}_e, \bar{\nu}_\mu, \bar{\nu}_\tau)$ to vacuum mass eigenstates $(\bar{\nu}_1, \bar{\nu}_2, \bar{\nu}_3)$. These eigenstates connect with each other through complex conjugate of PMNS matrix in Eq.(2.31). Especially, a large mixing angle $\theta_{12} = 34^\circ$ enhances flavor mixing through such matter effect. Fig.5.7(c) shows antineutrino spectra at $r = 3300$ km. The matter effect increases the flux of $\bar{\nu}_e$ in low energy region $E < E^{(l)}_{c1} = 8.2$ MeV where $E^{(l)}_{c1}$ represents the first spectral crossing point. Furthermore, the matter effect also makes a difference between the flux of $\bar{\nu}_\mu$ and that of $\bar{\nu}_\tau$, which reflects three flavor mixing caused by the PMNS matrix.

In inverted mass hierarchy (Fig.5.6(b)), some flavor mixing appears around 330 km owing to collective neutrino oscillations, but the amplitude of flavor transitions are almost negligible because of the multiangle matter decoherence [65]. Therefore, collective neutrino oscillations fail to change antineutrino spectra as shown in Fig.5.7(e). After the collective neutrino oscillations, MSW resonances occur actively in $e-y$ sector. In inverted mass hierarchy, the resonance condition for antineutrinos is given by $\omega_{\rm atm}\cos 2\theta_{13} = \sqrt{2}G_F n_e(r)$ (see Eq.(2.68)). The resonance point depends on the antineutrino energy because of the energy dependence in $\omega_{\rm atm} \propto E^{-1}$. The spectral swap occurs from low energy to high energy antineutrinos as electron density decreases. The MSW resonance causes the spectral split around $E \sim 1$ MeV in Fig.5.7(e). In outer region, the dramatic spectral swap also happens in high energy electron antineutrinos as shown in Fig.5.7(f).

Here, we discuss how collective neutrino oscillations have influence on the νp-process nucleosynthesis. In proton-rich outflows ($Y_e > 0.5$), the νp-process happens through (p,γ) and (n,p) reactions during $T \sim 1.5-3\times10^9$ K which corresponds to $r \sim 250-760$ km as shown in a green line in Fig.5.5. In this temperature region, most of free neutrons are supplied by the charged current reaction $\bar{\nu}_e + p \to e^+ + n$. In addition, the neutral current reaction $\alpha + \nu \to {}^3{\rm He} + n + \nu'$ also produces abundant free neutrons because α-particles become dominant species after the α-rich freeze-out. The modification of antineutrino energy spectra due to neutrino oscillations has influence on the neutrino induced reaction rates. The reaction rate $\lambda\,[s^{-1}]$ represents the frequency of nuclear reaction per unit time and a target particle. There is no oscillation effects on the reaction rate of $\alpha(\nu,\nu'n)^3$He because of the neutral current reaction. On the other hand, the charged current reaction $p(\bar{\nu}_e,e^+)n$ can probe evolution of collective neutrino oscillation as shown in Fig.5.6. The reaction rate of $p(\bar{\nu}_e,e^+)n$ is derived by the integration of $\bar{\rho}_{ee}(r,E,\theta_p)$:

$$\lambda_{\bar{\nu}_e} = \int {\rm d}E {\rm d}\cos\theta_p \sum_{\alpha=e,\mu,\tau} \frac{L_{\bar{\nu}_\alpha}}{2\pi R_\nu^2 \langle E_{\bar{\nu}_\alpha}\rangle} f_{\bar{\nu}_\alpha}(E)\bar{\rho}_{ee}(r,E,\theta_p)\sigma_{\bar{\nu}_e}(E). \tag{5.16}$$

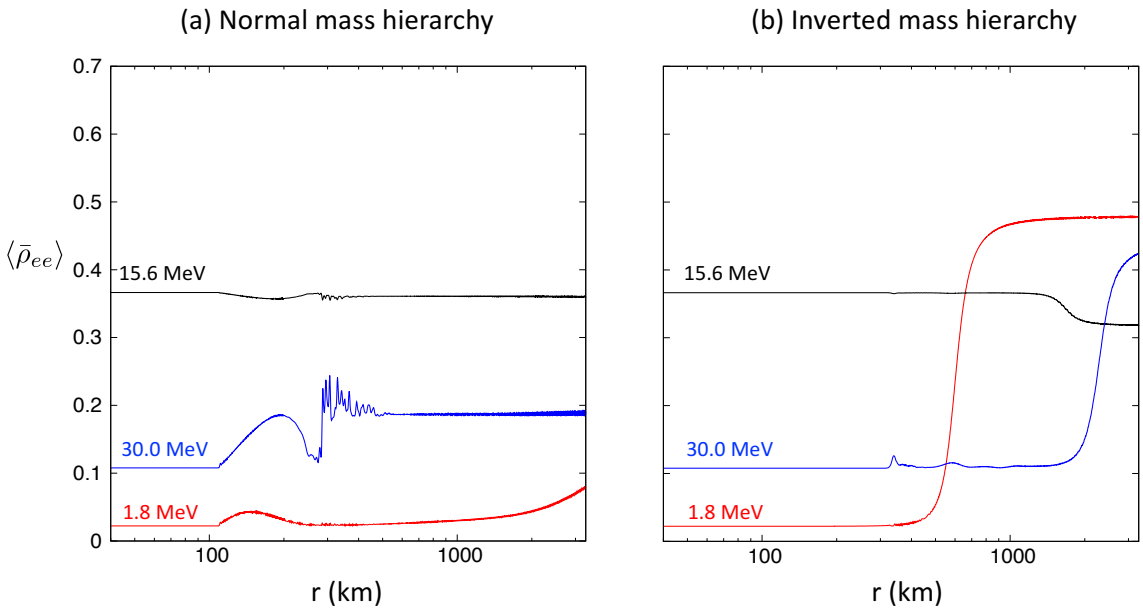

Figure 5.6: The evolution of angular averaged diagonal components $\langle \bar{\rho}_{ee}(r, E) \rangle$ in normal mass hierarchy (a) and inverted mass hierarchy (b) using the later wind model ($t = 1.1$ s). The values of these diagonal components do not change if any flavor transition is negligible. Neutrino oscillations in $r \sim 250 - 760$ km can affect the νp-process nucleosynthesis.

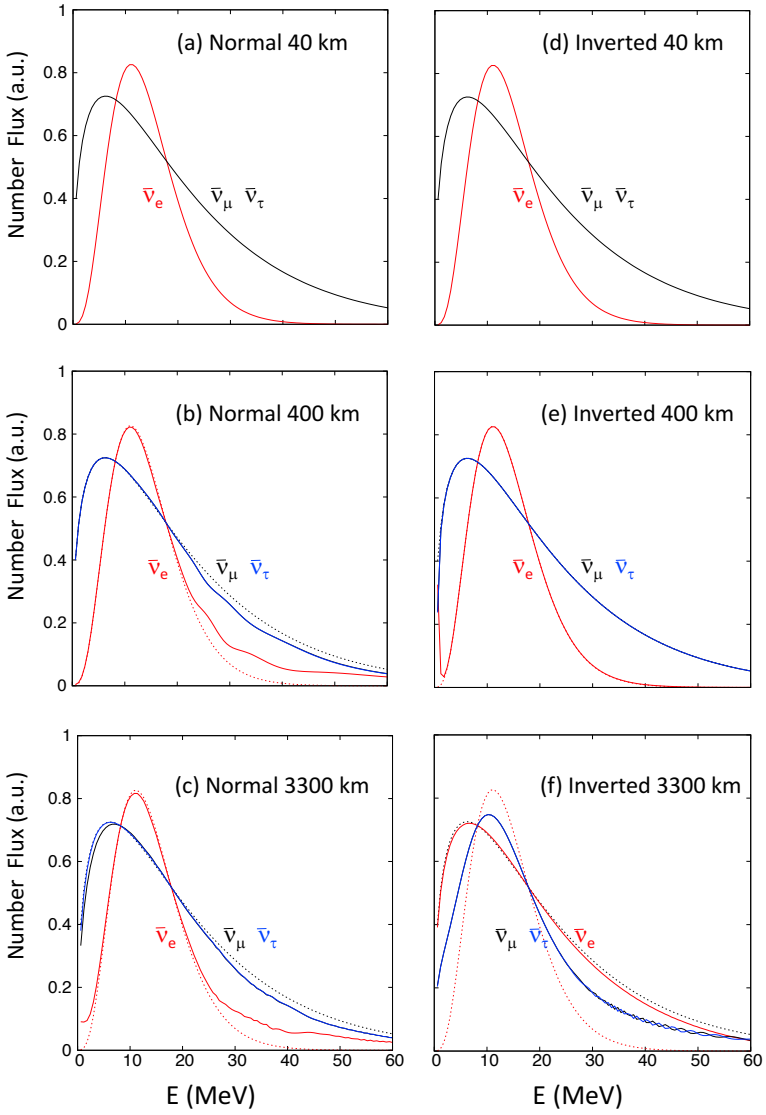

Figure 5.7: The energy spectra of antineutrinos in different radiuses in both neutrino mass hierarcies by using the later wind model ($t = 1.1$ s). Thin dashed lines display initial antineutrino spectra. There are two spectral crossings whose energies are $E_{c1}^{(l)} = 8.2$ MeV and $E_{c2}^{(l)} = 17.8$ MeV.

Fig.5.8 shows the evolution of normalized λr^2 in the later wind model where λ represents the reaction rate of $\alpha(\nu,\nu' n)^3$He or $p(\bar{\nu}_e, e^+)n$. Without flavor transitions, the reaction rate λ decreases as $\lambda \propto 1-\sqrt{1-(R/r)^2} \sim 1/2(R/r)^2$ ($r >> R$). We normalize the quantity λr^2 by the final value of $\lambda_{\bar{\nu}_e} r^2$ in no oscillation case as shown in the dashed black curve in Fig.5.8. The contribution from collective neutrino oscillations on Eq.(5.16) is included in diagonal components of antineutrino density matrices $\bar{\rho}_{ee}(r, E, \theta_p)$.

In normal mass hierarchy, collective neutrino oscillations increases the value of $\lambda_{\bar{\nu}_e}$ around $r \sim 200$ km where quasistatistical equilibrium (QSE) [262] is satisfied in almost all nuclides. In the QSE state ($T \sim 3-5\times10^9$ K), nuclear abundances are determined by baryon density, Y_e, temperature and small amount of heavy elements Y_h in the system. The value of Y_e is not so sensitive to the feedback effect of neutrino oscillations in multiangle simulations. Therefore, the enhanced reaction rate does not have strong impact on nucleosynthesis in this region. Before the νp-process, seed elements for heavy nuclei, for example, ^{56}Ni, ^{60}Zn and ^{64}Ge are produced through α-capture reactions. Around the onset of the νp-process ($T \sim 3\times10^9$ K), a NiCu cycle below

$$^{56}\mathrm{Ni}(n,p)^{56}\mathrm{Co}(p,\gamma)^{57}\mathrm{Ni}(n,p)^{57}\mathrm{Co}(p,\gamma)^{58}\mathrm{Ni}(p,\gamma)^{59}\mathrm{Cu}(p,\alpha)^{56}\mathrm{Ni}, \tag{5.17}$$

prevents the production of nuclei heavier than ^{56}Ni [248]. When the temperature becomes smaller than $\sim 3\times10^9$ K, another proton capture reaction $^{59}\mathrm{Cu}(p,\gamma)^{60}\mathrm{Zn}$ occurs more actively than $^{59}\mathrm{Cu}(p,\alpha)^{56}\mathrm{Ni}$. This breaks the NiCu cycle and produces heavier elements through the νp-process. The early increased $\lambda_{\bar{\nu}_e}$ near the onset of flavor transitions ($r \sim 110$ km) does not have any contribution to nucleosynthesis. However, the sharp enhancement of $\lambda_{\bar{\nu}_e}$ around 280 km induces remarkable influence on the nucleosynthesis. This sharp structure of $\lambda_{\bar{\nu}_e}$ is due to the collective neutrino oscillations of energetic antineutrinos as shown by 30 MeV antineutrinos in Fig.5.6(a) because of the energy dependence of $\sigma_{\bar{\nu}_e} \propto (E/\mathrm{MeV}-1.293)^2$. The value of $\lambda_{\bar{\nu}_e}$ is raised by a factor 2 and kept up until the freeze out of the νp-process inside the outflow. This implies that the νp-process is enhanced successfully by collective neutrino oscillations, which results in the creation of more abundant p-nuclei.

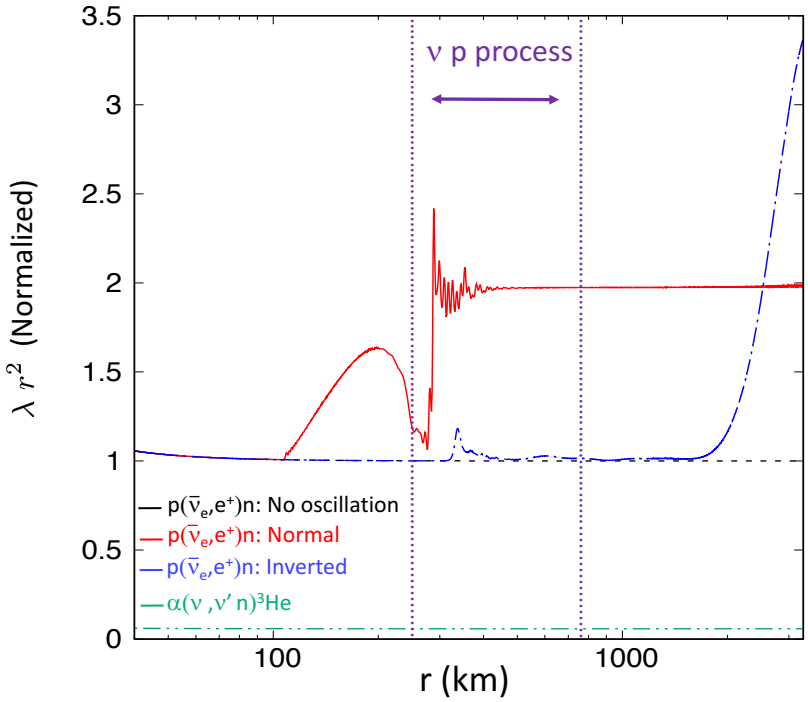

Figure 5.8: The evolution of λr^2 in the later wind model ($t = 1.1$ s) where λ represents the normalized reaction rate of $p(\bar{\nu}_e, e^+)n$ and $\alpha(\nu, \nu' n)^3$He. The νp-process occurs actively in the interval $r \sim 250 - 760$ km which corresponds to $T \sim 1.5 - 3.0 \times 10^9$ K.

In inverted mass hierarchy, the reaction rate $\lambda_{\bar{\nu}_e}$ is not raised up by collective neutrino oscillations in the region $r \sim 250 - 760$ km where the νp-process occurs. After the νp-process, β^+ decays and (n, γ) become dominant nuclear reactions inside the neutrino driven winds. Even though $\lambda_{\bar{\nu}_e}$ increases dramatically later owing to MSW effects and finally exceeds the value in normal mass hierarchy, few free neutrons are produced inside the wind trajectory because of the decreasing neutrino fluxes and the large wind velocity $v(r) \sim 3 \times 10^9$ cm/s. Therefore, we can expect that the νp-process and neutron-capture reactions in the later wind model are not affected by neutrino oscillations in inverted mass hierarchy.

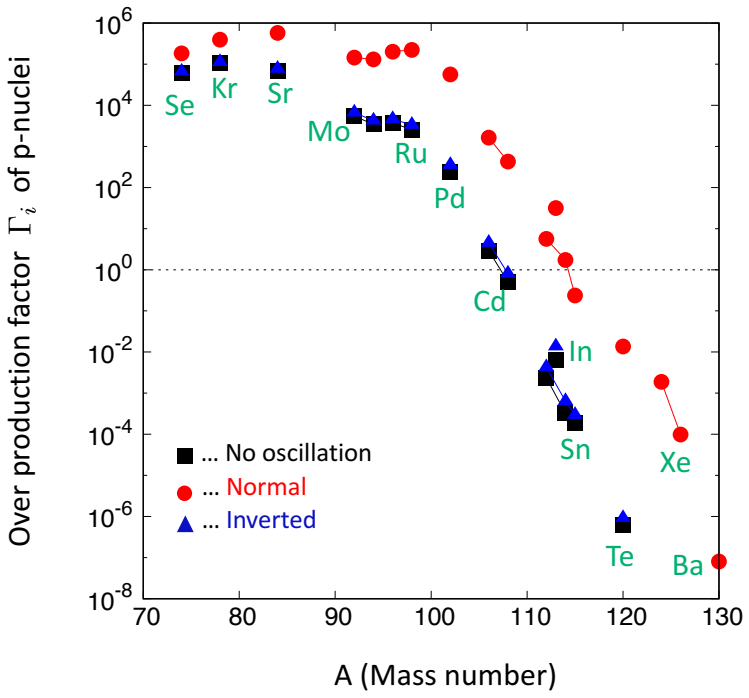

Figure 5.9: The overproduction factors of p-nuclei derived from Eq.(5.18) in the later wind model ($t = 1.1$ s). The value of Γ_i increases if collective neutrino oscillations induce more active νp-process which results in the production of large amount of p-nuclei.

Fig.5.9 shows the overproduction factor of p-nuclei:

$$\Gamma_i = \frac{X_i}{X_{i,\mathrm{solar}}} / \frac{X_{^{56}\mathrm{Fe}}}{X_{^{56}\mathrm{Fe,solar}}}, \tag{5.18}$$

where X_i and $X_{i,\mathrm{solar}}$ represent the mass fraction of nuclear species i inside the wind and in our solar system [263], respectively. The mass fraction X_i is estimated by calculating the nucleosynthesis until all reactions freeze out. The value of Γ_i becomes large if abundant p-nuclei are produced through the νp-process. In case of $\Gamma_i > 1$, the neutrino driven wind contains large amounts of nucleus i which can explain the solar abundance of i sufficiently if all of ^{56}Fe in the solar system is given only by this wind trajectory. Therefore, $\Gamma_i > 1$ is necessary condition if neutrino driven winds are one of the promising sites for the origin of light p-nuclei in our solar system. The absolute value of Γ_i is important to study the contribution from neutrino driven winds to the solar abundances of p-nuclei. We should include the contribution from the early wind model if we discuss the possibility that collective neutrino oscillations can affect solar abundances of p-nuclei.

The suggestions obtained in Fig.5.8 are actually confirmed in Fig.5.9. More p-nuclei are produced by collective neutrino oscillations in normal mass hierarchy. Owing to the oscillation effects, the nuclear flow on the chart of nuclides can reach heavier p-nuclei such as ^{124}Xe,^{126} Xe and ^{130}Ba which are not created in the no oscillation case. Collective neutrino oscillations enhances the overproduction factor extremely by up to $\sim 10^4$ times. The amount of such enhancement is larger than that of Ref. [216] (up to ~ 20 times). Our initial neutrino parameters as shown in Table 5.1 are favorable for the enhancement of energetic $\bar{\nu}_e$ through the neutrino self interactions because of a large excess of the ν_β flux over the $\bar{\nu}_e$ flux in $E > E_{c2}^{(l)}$. The spectral swap in energetic antineutrino results in the large overproduction factor of p-nuclei in our model owing to the energy dependence in Eq.(5.6). In inverted mass hierarchy, the νp-process is not enhanced evidently even though the reaction rate $\lambda_{\bar{\nu}_e}$ is increased significantly by MSW resonances after the νp-process, as suggested in Fig.5.8 and the previous paragraph. In the no oscillation case, the nucleosynthesis also fails to produce heavier p-nuclei although lighter p-elements, for example, ^{74}Se, ^{78}Kr and ^{84}Sr

are synthesized. These results indicate that collective neutrino oscillations should be taken into account in the network calculation of the νp-process in order to estimate precise abundances of p-nuclei inside neutrino driven winds.

5.3.2 Early neutrino driven wind ($t = 0.6$ s) without the reverse shock

Collective neutrino oscillations are highly sensitive to the ratio of number fluxes among all species of neutrinos [72]. In the cooling phase of the proto-neutron star, neutrino luminosities and mean energies are changing, which results in the variety of non-linear flavor transitions. In this section, we show numerical results of the early wind model ($t = 0.6$ s) ignoring the reverse shock effect. Then, we discuss the enhanced νp-process nucleosynthesis caused by collective neutrino oscillations in the same way as §5.3.1. In the early wind trajectory ($t = 0.6$ s), collective neutrino oscillations are well confirmed in inverted mass hierarchy, which produces more abundant p-nuclei. The contribution of the reverse shock to the nucleosynthesis is mentioned in the next subsection.

In normal mass hierarchy (Fig.5.10(a)), collective neutrino oscillations start around $r \sim 110$ km but all of antineutrinos return to their original flavors after the flavor mixing. Such behaviors are similar to that of Fig.5.6 (a) except for the sharp flavor transition in high energy region. Antineutrino spectra after collective neutrino oscillations ($r \sim 400$) km corresponds to original spectra as shown in Fig.5.11(b). The onset of the νp process is $r \sim 350$ km in our early wind model. Therefore, the effect of collective neutrino oscillations on the νp process may be almost negligible in normal mass hierarchy. After the collective neutrino oscillations, flavor eigenstates of antineutrinos are transformed to vacuum eigenstates adiabatically as the baryon density decreases because of the matter-induced flavor transition as discussed in the later wind model. Such matter effects violate the degeneracy between $\bar{\nu}_\mu$ and $\bar{\nu}_\tau$ as shown in Fig.5.11(c).

On the other hand, significant non-linear flavor transitions of energetic antineutrinos take place around $r \sim 250$ km in inverted mass hierarchy as shown by 15.6 and 30 MeV in Fig.5.10(b). Such flavor transitions result in the spectral swap of

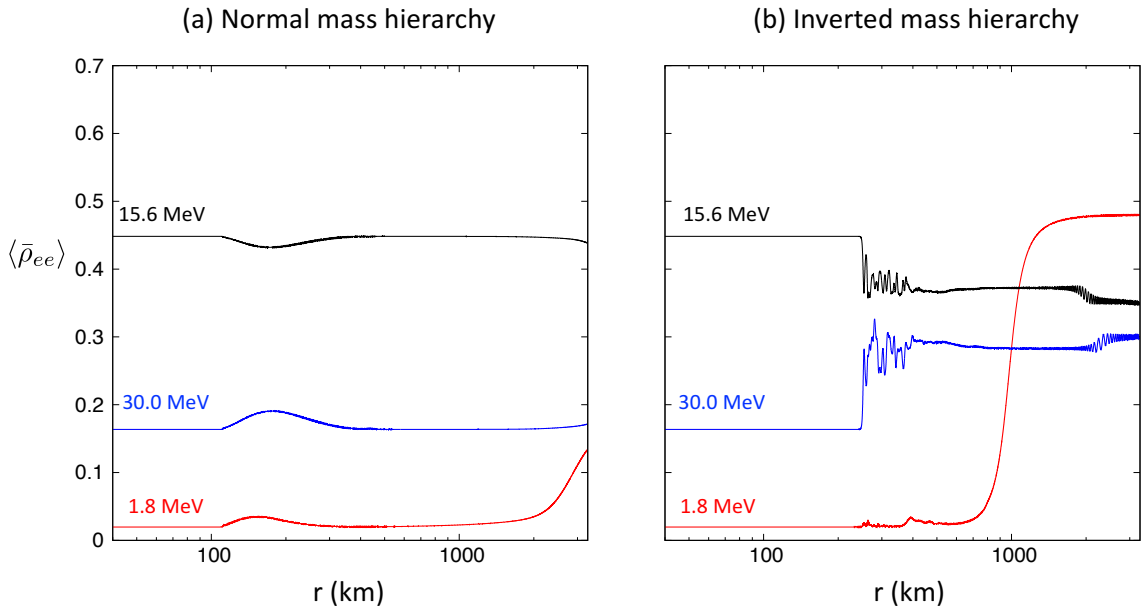

Figure 5.10: The evolution of Eq.(5.15) in normal mass hierarchy (a) and inverted mass hierarchy (b) using the later wind model ($t = 0.6$ s) without the reverse shock. Neutrino flavor transitions in $r \sim 350 - 1060$ km can affect the νp-process nucleosynthesis.

antineutrinos as shown in Fig.5.11(e). The spectral splits after neutrino self interactions appear around the spectral crossing points of antineutrino spectra [67, 71]. Flavor conversions are observed in high energy region $E > E_{c1}^{(e)} = 7.1$ MeV where $E_{c1}^{(e)}$ represents energy of the first crossing in the early wind model. The increased $\bar{\nu}_e$ whose energy is larger than the second spectral crossing point ($E_{c2}^{(e)} = 22.3$ MeV) causes the enhancement of the νp-process. After the neutrino self interactions, MSW resonances appears from low energy antineutrinos in $e - y$ sector as the baryon density decreases. In the outer region, energetic antineutrinos are also affected by the MSW resonances, which results in large modification in the $\bar{\nu}_e$ spectrum as shown in Fig.5.11(f).

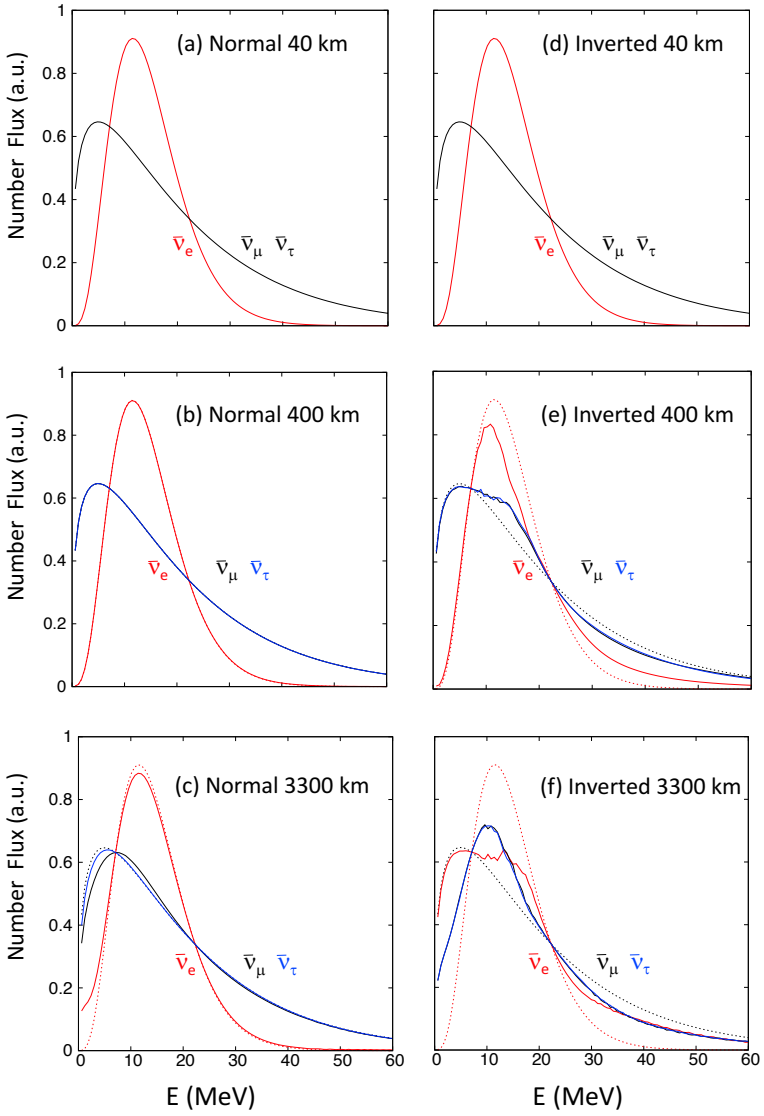

Figure 5.11: The energy spectra of antineutrinos in different radiuses for the early wind model without the reverse shock as in Fig.5.6. The value of two spectral crossings points are $E_{c1}^{(e)} = 7.1$ MeV and $E_{c2}^{(e)} = 22.3$ MeV.

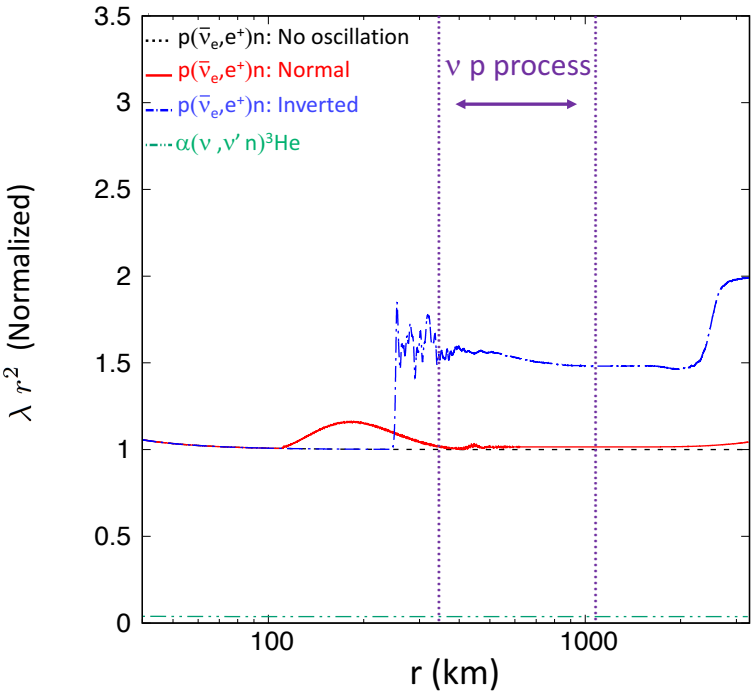

Figure 5.12: The evolution of λr^2 in the early wind model ($t = 0.6$ s) without the reverse shock as in Fig.5.8. The νp-process takes place in $r \sim 350 - 1060$ km.

Fig.5.12 shows the evolution of reaction rates in the early wind model without the reverse shock. The behaviors of collective neutrino oscillations as mentioned in previous paragraphs are reflected in this figure. In normal mass hierarchy, the normalized $\lambda_{\bar{\nu}_e} r^2$ (red solid line) is raised up and comes back to the value in no oscillation case (black dash line) before the νp-process nucleosynthesis, so that oscillation effects on nucleosynthesis are small. In inverted mass hierarchy (blue dash-dot line), however, collective neutrino oscillations can increase the reaction rate $\lambda_{\bar{\nu}_e}$ successfully and its high value is maintained during the νp-process ($r \sim 350 - 1060$ km). Such enhancement is mainly due to the increasing energetic electron antineutrinos ($E > E_{c2}^{(e)}$) because of the energy dependent cross section $\sigma_{\bar{\nu}_e} \propto (E/\mathrm{MeV} - 1.293)^2$. The normalized reaction rate is also raised up by the MSW effect of energetic antineutrinos around $r \sim 2000$ km. The enhancement caused by MSW resonances is too far to affect the production of p-nuclei as discussed in the later wind model.

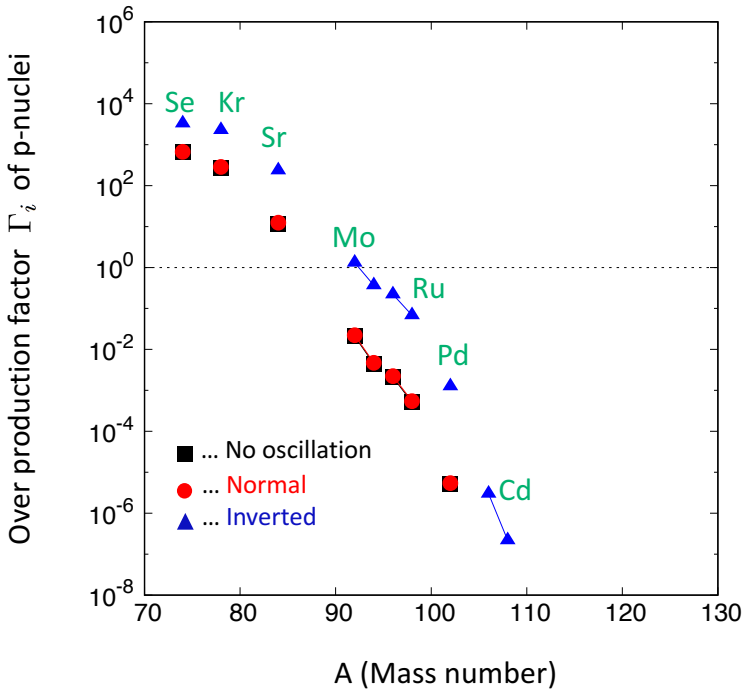

Figure 5.13: The overproduction factors of p-nuclei in the early wind model ($t = 0.6$ s) without the reverse shock.

The overproduction factor of p-nuclei in our early wind model without the shock effect is shown in Fig.5.13. These results clearly reflect the evolution of normalized $\lambda_{\bar{\nu}_e} r^2$ in Fig.5.12. In normal mass hierarchy, oscillation effects hardly contribute to the νp-process nucleosynthesis, so that the values of Γ_i is nearly equivalent to that of no oscillation case. In inverted mass hierarchy, however, the abundances of p-nuclei are increased by up to $\sim 10^2$ times due to the enhancement of $\lambda_{\bar{\nu}_e}$ in $r \sim 350 - 1060$ km. Heavy p-nuclei tend to be synthesized more abundantly because the large reaction rate produces more free neutrons which are supplied for subsequent (n, p) reactions on heavy nuclei as discussed in Ref. [216]. Even though oscillation effects are considered, the p-nuclei are created up to ^{106}Cd and ^{108}Cd. Without the reverse shock, temperature decreases slower than the time scale of α-captures [226] in the early wind model. Therefore, more iron-group elements such as ^{56}Ni are synthesized before the νp-process, which results in small amount of heavier elements than ^{56}Ni.

5.3.3 Reverse shock effect on the early neutrino driven wind ($t = 0.6$ s)

The νp-process depends on both electron antineutrino spectrum and hydrodynamic quantities of neutrino driven winds. We discuss an uncertainty of neutrino oscillations for the νp-process nucleosynthesis and the production of p-nuclei in last subsections. In this subsection, however, we mention an uncertainty of hydrodynamics. We show numerical results of the early wind model ($t = 0.6$ s) considering the reverse shock. Previous studies [247, 248] show that the νp-process inside neutrino driven winds can be enhanced by the reverse shock (or wind termination). Fig.5.14 represents the radial profile of wind temperature, baryon density and wind velocity in the early wind model ($t = 0.6$ s) both with and without the reverse shock. The time snapshots including the reverse shock (purple lines in Fig.5.14) are original data obtained by 1D explosion simulation. After the reverse shock, expansion speed of the ejecta decreases dramatically, which enables matter to be exposed to high neutrino fluxes. Actually, an abundance of free neutrons supplied through $p(\bar{\nu}_e, e^+)n$ from r to $r + \Delta r$ is written as

$$\Delta Y_n|_{\rm cc} = \frac{\lambda_{\bar{\nu}_e} Y_p \Delta r}{v(r)}, \tag{5.19}$$

where Y_p represents the abundance of free protons. The value of $\Delta Y_n|_{\rm cc}$ becomes large when the wind velocity $v(r)$ is reduced by the reverse shock. In addition, the reverse shock keeps the wind temperature within the temperature range of $T \sim 1.5-3.0\times10^9$ K. These hydrodynamical effects are favorable for the production of heavier p-nuclei through the νp-process. The time snapshots without the reverse shock (green lines in Fig.5.14) are employed in §5.3.2. The contribution of the reverse shock is removed from such wind trajectory. The radial profiles of baryon density and wind temperature after the reverse shock are fitted to exponential declines by assuming a constant entropy per baryon: $S \propto T^3/\rho =$ const. and constant wind velocity: $v(r) =$ const..

Fig.5.15 shows the evolution of the normalized reaction rates in the early wind model with the reverse shock. Such behaviors are equivalent to that in Fig.5.12 till the position of the reverse shock $r = 870$ km. In both mass hierarcies, collective neutrino oscillations have terminated before the reverse shock, so that the reverse shock only affects matter-induced flavor transitions in outer region. The amplitude of the matter potential does not decrease significantly after the reverse shock because of the plateau of the baryon density profile as shown in Fig.5.14(b). Therefore, flavor conversions caused by matter effects in Fig.5.10 are highly suppressed if we take into account the shock effect. Especially, in inverted mass hierarchy, the enhancement of $\lambda_{\bar{\nu}_e}$ around $r \sim 2000$ km in Fig.5.12 disappears in Fig.5.15. The end point of the νp-process is extended to $r \sim 4070$ km owing to the almost constant temperature profile after the reverse shock as shown in Fig.5.14(a), which results in production of more abundant p-nuclei. The MSW resonances are suppressed after the reverse shock, so that the νp-process can easily probe the contribution of collective neutrino oscillations even though the temperature region of νp-process is broadened outward.

The overproduction factor of p-elements Γ_i in the early wind model with the reverse shock is shown in Fig.5.16. Heavy p-nuclei are synthesized up to ^{120}Te owing to the reverse shock effect. Furthermore, overproduction factors of heavy p-nuclei are raised up significantly compared with that in Fig.5.13 regardless of flavor conversions

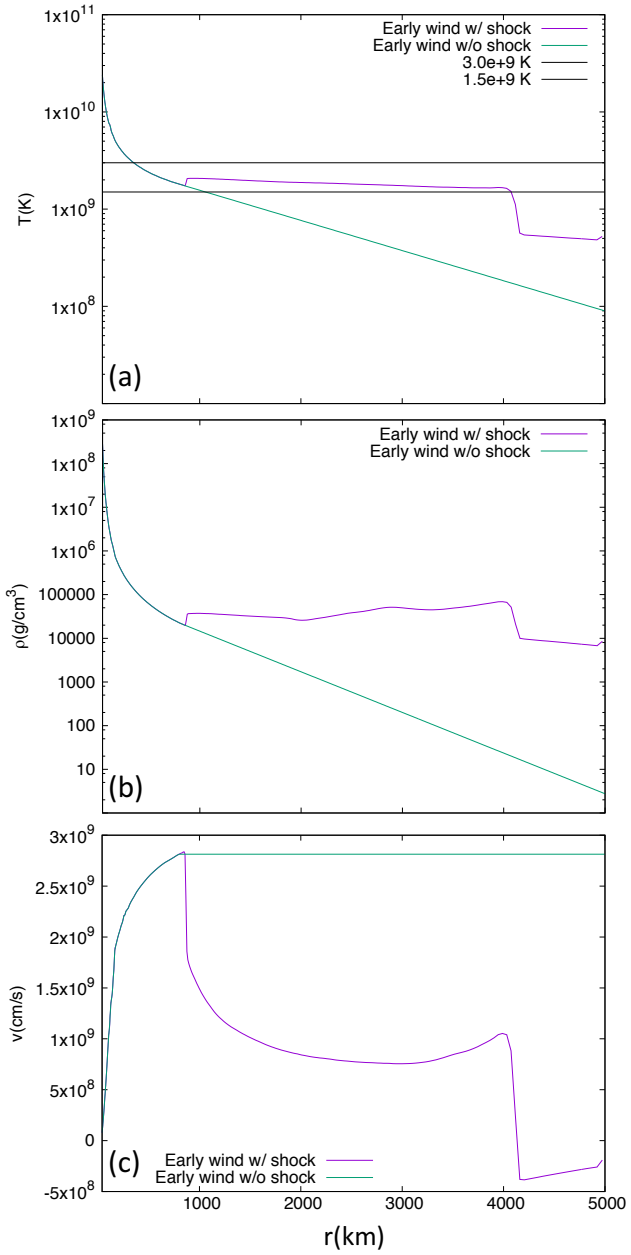

Figure 5.14: The radial profiles of temperature (a), baryon density (b) and wind velocity (c) in both early wind models ($t = 0.6$ s) with and without the reverse shock at 870 km. The early wind model with the reverse shock (purple lines) corresponds to the time snapshot at $t = 0.6$ s given by the 1D explosion simulation. Numerical results in §5.3.2 are obtained by employing the early wind model without the reverse shock (green lines).

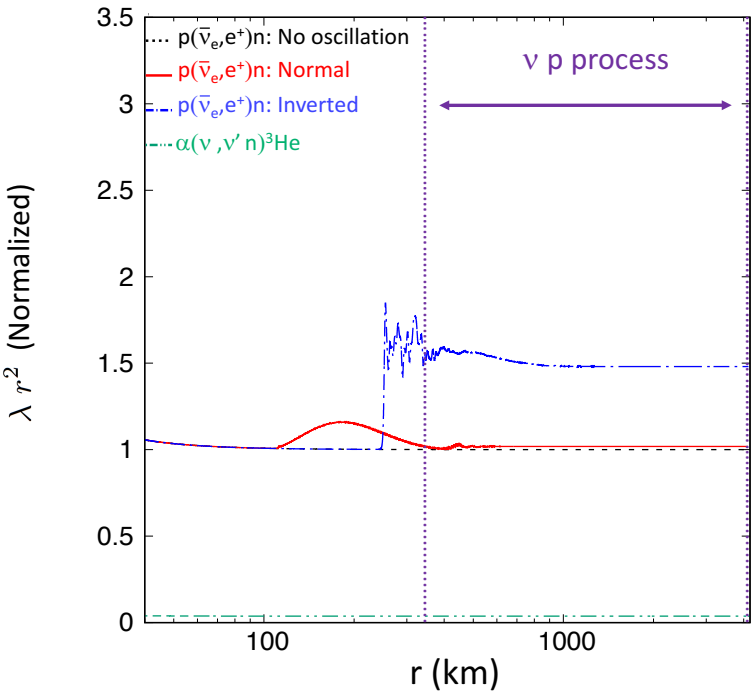

Figure 5.15: The evolution of λr^2 as in Fig.5.12 in the early wind model (t = 0.6 s) considering the reverse shock. The enhancement of $\lambda_{\bar{\nu}_e}$ caused by MSW resonances is suppressed in this wind trajectory. The temperature range of the νp-process is extended to 4070 km.

because of the small wind velocity and the plateau of wind temperature after the reverse shock. The enhancement of Γ_i caused by collective neutrino oscillations is also confirmed in this wind model. Such oscillation effect is prominent in inverted mass hierarchy as implied in Fig.5.15, which increases the total productions of ^{92,94}Mo and ^{96,98}Ru in inverted mass hierarchy in this progenitor model. In normal mass hierarchy, value of Γ_i is somewhat larger than that in no oscillation case even though any oscillation effects are negligible in the early wind model without the reverse shock (see Fig.5.13). The νp-process nucleosynthesis inside the small speed of ejecta is sensitive to the slight increase of normalized reaction rate in normal mass hierarchy $\lambda_{\bar{\nu}_e} r^2 \sim 1.018$ because small $v(r)$ easily amplifies the enhancement of $\Delta Y_n|_{\rm cc}$ caused by oscillation effects.

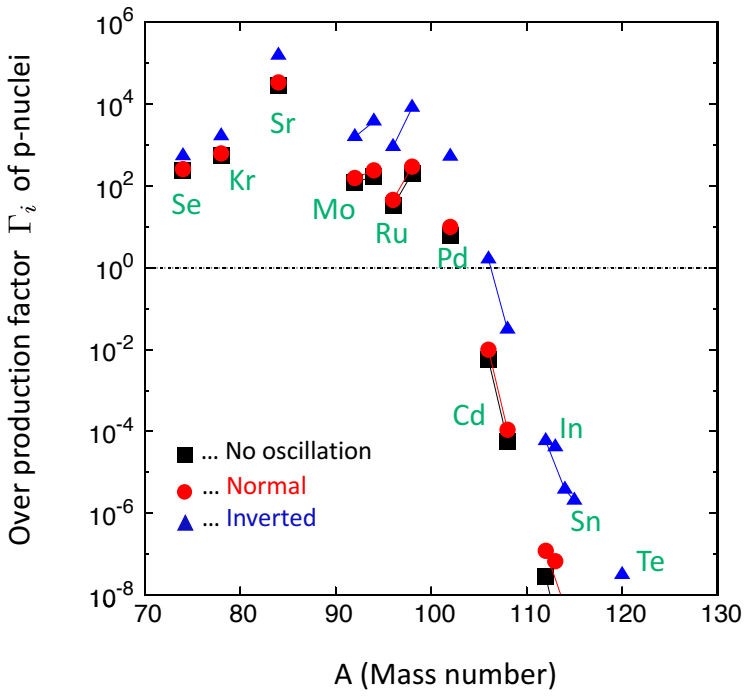

Figure 5.16: The overproduction factors of p-nuclei in the early wind model ($t = 0.6$ s) considering the reverse shock. More abundant heavy p-nuclei are produced compared with Fig.5.13 owing to the reverse shock effect.

5.3.4 Averaged overproduction factors of p-nuclei

The total abundances of p-nuclei produced inside neutrino driven winds are obtained by a summation of their abundances inside different wind trajectories. Behaviors of collective neutrino oscillations are sensitive to explosion time after the core-bounce. In the early wind models ($t = 0.6$ s), collective neutrino oscillations are outstanding in inverted mass hierarchy irrespective of the reverse shock. Conversely, in the later wind model ($t = 1.1$ s), the production of p-nuclei is enhanced by oscillation effects in normal mass hierarchy. Here, we average the overproduction factors of early and later wind models in order to discuss the contribution of neutrino oscillations to the total production of p-nuclei. The averaged overproduction factor $\langle \Gamma_i \rangle$ is given by

$$\langle \Gamma_i \rangle = (1-f)\Gamma_i|_{\rm early} + f\Gamma_i|_{\rm later}, \tag{5.20}$$

where $\Gamma_i|_{\rm early}$ ($\Gamma_i|_{\rm later}$) is the overproduction factor of nucleus i in the early (later) wind model, respectively. The mass weight f for the average is defined by

$$f = \frac{\Delta M_{^{56}\rm Fe}|_{\rm later}}{\Delta M_{^{56}\rm Fe}|_{\rm early} + \Delta M_{^{56}\rm Fe}|} \tag{5.21}$$

where $\Delta M_{^{56}\rm Fe}|_{\rm early}$ and $\Delta M_{^{56}\rm Fe}|_{\rm later}$ are mass of ^{56}Fe in the early ejecta ($0.6\ {\rm s} < t < 1.1$ s) and the later one ($t > 1.1$ s). The value of $\Delta M_{^{56}\rm Fe}|_{\rm later}$ is estimated by assuming the contribution of the later neutrino driven wind is effective up to $t \sim 3$ s because mass ejection after $t > 3$ s is small [223]. We can roughly regard this averaged quantity $\langle \Gamma_i \rangle$ as the overproduction factor of nucleus i in the total ejecta which are emitted through neutrino driven winds in the cooling phase.

	$\Delta M_{^{56}\rm Fe}\|_{\rm early}$ ($\times 10^{-6} M_\odot$)	$\Delta M_{^{56}\rm Fe}\|_{\rm later}$ ($\times 10^{-6} M_\odot$)	f ($\times 10^{-2}$)
No ocillations	68.0	5.29	7.2
Normal	68.0	3.11	4.4
Inverted	60.8	5.17	7.8

Table 5.2: The mass of ^{56}Fe in ejecta without the reverse shock and the mass weight f in each hierarchies. The value of f is derived by Eq.(5.21).

The averaged overproduction factor $\langle \Gamma_i \rangle$ by using overproduction factors of Figs.5.9

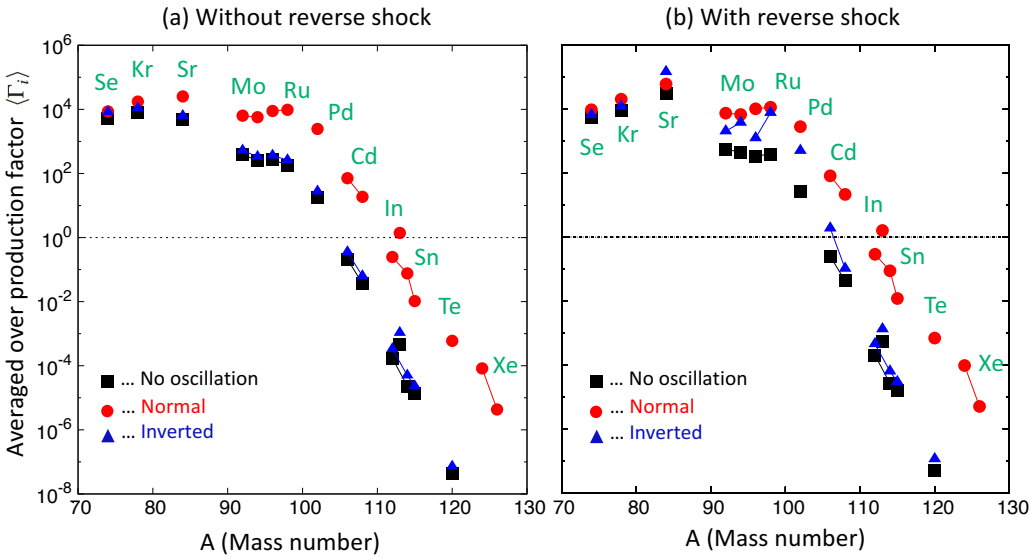

Figure 5.17: Averaged overproduction factors of p-nuclei both ignoring the reverse shock (a) and including the shock effect (b) in the early wind trajectory ($t = 0.6$ s).

	$\Delta M_{^{56}\mathrm{Fe}}\vert_{\mathrm{early}}$ ($\times 10^{-6} M_\odot$)	$\Delta M_{^{56}\mathrm{Fe}}\vert_{\mathrm{later}}$ ($\times 10^{-6} M_\odot$)	f ($\times 10^{-2}$)
No ocillations	58.2	5.29	8.3
Normal	58.1	3.11	5.1
Inverted	49.9	5.17	9.4

Table 5.3: The amount of ^{56}Fe and the ratio f in the case considering the reverse shock in the early wind model.

and 5.13 is shown in Fig.5.17(a). Here, we employ the ratio f in Table.5.2. The hierarchy difference is reduced in lighter p-nuclei ($A \leq 84$) because of the contribution from early phase in inverted mass hierarchy. On the other hand, heavier p-nuclei ($A \geq 92$) are mainly produced in the later wind model despite the small ratio f in Table.5.2 because the small dynamical time scale of later wind model prevents α-process which creates seed nuclei for heavy elements [226, 227]. In addition, the large electron fraction $Y_e \sim 0.59$ in the later wind model increases the abundance of free protons Y_p for $p(\bar{\nu}_e, e^+)n$, which results in the active νp-process and high values of Γ_i.

The reverse shock enhances the contribution of the early phase as shown in Fig.5.17(b). Such averaged overproduction factor $\langle \Gamma_i \rangle$ considering the reverse shock is derived by using the ratio f in Table.5.3. The ejected mass of ^{56}Fe in the early phase is smaller than that of Table.5.2 because the reverse shock encourages the nuclear flow on the chart of nuclei to move to heavier elements than ^{56}Ni. Such shift of nuclear flow promotes the creation of p-nuclei larger than ^{84}Sr exceedingly. In Fig.5.17(b), the deviation between no oscillation case (black square) and inverted mass hierarchy (blue triangle) becomes prominent in intermediate mass p-nuclei ($84 \leq A \leq 108$). On the other hand, the contribution of the later wind model is dominant in $A > 108$ because the nuclear flow in the early wind model has stopped up to ^{120}Te even though the reverse shock is taken into account. Productions of ^{92,94}Mo and ^{96,98}Ru are enhanced by collective neutrino oscillations in both neutrino mass hierarcies owing to the reverse shock effect.

5.4 Summary and discussion

We study how collective neutrino oscillations can affect the νp-process nucleosynthesis inside neutrino driven winds. We carry out three flavor multiangle simulations together with nucleosynthesis network calculation by using early (later) wind model at $t = 0.6(1.1)$ s after core bounce obtained by the 1D explosion simulation model. The contribution from the reverse shock effect is ignored in Ref. [82], but, in this thesis, we also introduce how the reverse shock multiplies the oscillation effects on the νp-process.

In the later wind model ($t = 1.1$ s), we find the νp-process is dramatically enhanced by sharp transitions around 280 km, which increases energetic electron antineutrinos. This flavor transition in normal mass hierarchy is induced mainly in $e - y$ sector, so that the mechanism of flavor mixing is different from the $e - x$ conversions in §4.2.3. The dominant $e - y$ conversion in normal mass hierarchy is also reported in Ref. [71] because a set of initial conditions where number fluxes of nonelectron (anti) neutrino flavors are larger than that of electron (anti) neutrino, which is also the case in our simulation. The enhanced νp process allows the value of the overproduction factor of p-nuclei Γ_i to be raised by $\sim 10 - 10^4$ times. The results depend on the initial neutrino parameters on the surface of neutrino sphere which are shown in Table 5.1. The dramatic enhancement of p-nuclei is partially due to the large excess of nonelectron antineutrinos over electron antineutrinos in the high energy region. Our results indicate the necessity of incorporating the effects of collective neutrino oscillations for precise νp process nucleosynthesis calculations in wind trajectories. Furthermore, our finding also suggests that such precise theoretical studies of νp process nucleosynthesis can potentially identify the still unknown origin of the solar ^{92,94}Mo and ^{96,98}Ru.

In the early wind model ($t = 0.6$ s) without the reverse shock, collective neutrino oscillations increase the flux of $\bar{\nu}_e$ in inverted mass hierarchy. The behavior of collective neutrino oscillations are sensitive to the initial neutrino spectra on the surface of neutrino sphere. The νp-process nucleosynthesis takes place during $\sim 350 - 1060$

km which corresponds to the temperature region: $T = 1.5 - 3.0 \times 10^9$ K. The energetic $\bar{\nu}_e$ promotes the νp-process actively because of the energy dependence of the cross section in Eq.(5.6), which results in abundant p-nuclei by up to 10^2 times larger than those in the no oscillation case. The νp-process does not reach the production of heavy p-elements because seed nuclei for heavy elements are synthesized so much through active α-capture reactions.

In the early wind model ($t = 0.6$ s) considering the reverse shock, however, the production of p-nuclei are enhanced dramatically in $A \geq 84$. Outside the reverse shock, the temperature becomes almost constant in the temperature region of the νp-process, so that the end point of the νp-process is extended up to 4070 km. In addition, the wind velocity $v(r)$ becomes small outside the reverse shock, which increases the production of free neutrons through $p(\bar{\nu}_e, e^-)n$ as shown in Eq.(5.19). These properties of reverse shock are favorable for the production of p-nuclei through the νp-process. Collective neutrino oscillations have terminated before the position of the reverse shock $\sim$ 870 km. The baryon density is nearly constant outside the reverse shock, so that the MSW effects of energetic $\bar{\nu}_e$ are highly suppressed. The νp-process is not sensitive to the MSW resonances. Therefore, oscillation effects on the νp-process come from only collective neutrino oscillations. The enhancement of the νp-process is prominent in inverted mass hierarchy as the case without the reverse shock.

We calculate the averaged overproduction factor of p-nuclei $\langle \Gamma_i \rangle$ by using early and later wind trajectories. The reverse shock effect in the early wind model increases the contribution from the early wind model to $\langle \Gamma_i \rangle$. Especially, in inverted mass hierarchy, p-nuclei in the region of $A = 84 - 108$ are mainly produced inside the early wind model. Therefore, the production of ^{92,94}Mo and ^{96,98}Ru are enhanced by collective neutrino oscillations in both mass hierarchies if we take into account the reverse shock. More quantitative discussion about the nucleosynthesis is desirable by using many more wind trajectories beyond $t \sim 1.1$ s which are ignored in the present calculation due to limited computational resources. In addition, the contributions of the outer Si-burning layer are necessary to obtain the total abundance of these

nuclides produced in this explosion model. The net overproduction factors would be $\Gamma_i \sim 1$ if the solar abundances of p-nuclei are explained successfully in the supernova model. In the calculation with the reverse shock, $\langle \Gamma_i \rangle$ for ^{92,94}Mo and ^{96,98}Ru take large values $\sim 10^3 - 10^4$ in both mass hierarcies. Taking into account the contributions of other ejecta affected by explosive nucleosynthesis in outer layers (see §5.1.1), the values of $\langle \Gamma_i \rangle$ will be lowered by several orders because large amount of ^{56}Fe is produced in the explosive nucleosynthesis. In our rough estimate assuming the total amount of ^{56}Ni ejecta in SN1987A: $M_{^{56}\mathrm{Ni}} = 0.07 M_\odot$ [222], the values of $\langle \Gamma_i \rangle$ in the present study decrease by 3 orders of magnitude.

The caveat of this study is the uncertainty of neutrino parameters describing neutrino spectra. Both collective neutrino oscillations and nucleosynthesis highly depend on the initial neutrino parameters. If the differences between luminosities and energies of different neutrino species are very small, oscillation effects on $\lambda_{\bar{\nu}_e}$ are negligible. In our explosion model, the value of $\langle E_{\nu_\beta} \rangle$ may decrease and approach to that of $\langle E_{\bar{\nu}_e} \rangle$ if we included neutral current reactions discussed in Ref. [230]. Such modifications may lower the initial number flux of ν_β in high energy region reducing the enhancement of $\lambda_{\bar{\nu}_e}$ as shown in Ref. [80]. However, note that nucleon-nucleon correlation may increase neutrino mean energies [193, 202, 264].

The νp process depends not only on initial neutrino parameters but also on hydrodynamic quantities as shown, for example, in the case of the reverse shock. Therefore, a comprehensive and systematic study of hydrodynamic quantities as well as initial neutrino parameters is desirable in order to better understand the behavior of collective neutrino oscillations and the properties of nucleosynthesis in neutrino driven winds.

Chapter 6

Conclusion

In this thesis, we carry out numerical simulations of collective neutrino oscillations inside core-collapse supernovae. Then, we study how such non-linear flavor conversions can be detected in future neutrino observatories and how the νp-process nucleosynthesis inside neutrino driven winds can be enhanced by collective neutrino oscillations. In this chapter, we summarize the contents of this thesis. The background knowledge for our research are shown in Chapters 2 and 3. The main work of this thesis is discussed in Chapters 4 and 5.

In Chapter 2, we show the basics of neutrino oscillations. We can study neutrino oscillations by solving Liuville-von Neumann equations of (anti)neutrino density matrices ρ and $\bar{\rho}$ in Eqs.(2.57) and (2.58). The diagonal components of such density matrices correspond to the ratio of each flavor of neutrinos. Non-diagonal components represent the strength of quantum interference between different flavors of neutrinos. Neutrino oscillations inside medium is completely different from the flavor evolution in vacuum. We obtain the refractive potentials (see Eqs.(2.46) and (2.97)) caused by neutrino coherent forward scatterings with background electrons and neutrino themselves following the derivation in Refs. [45, 53]. The general form of non-linear potentials in Eq.(2.97) can be applied to various explosive astrophysical sites such as core-collapse supernovae, early universe, neutron star mergers and long gamma-ray bursts.

In Chapter 3, we review the standard scenario of core-collapse supernovae. After the core bounce, the shock heating produces large amounts of three flavor neutrinos and their corresponding antineutrinos at the center. Free streaming neutrinos outside the neutrino sphere experience collective neutrino oscillations caused by the non-linear potential of neutrino self interactions. We employ the bulb model as a neutrino emission model to calculate such non-linear neutrino oscillations. Eqs.(3.30) and (3.31) are equations of motion of the three flavor multiangle simulation which is reliable numerical method of current oscillation studies. Although this multiangle method is required for precise numerical simulations of collective neutrino oscillations, the fundamental properties of collective neutrino oscillations are confirmed in the simpler two flavor single angle calculation which ignores the dependence of neutrino scattering angle and reduces the number of neutrino flavors. We show numerical results of collective neutrino oscillations in the two flavor single angle calculation. In inverted mass hierarchy, the non-linear potential induces collective flavor conversions irrespective of neutrino energy and neutrino species. After that, the spectral swap occurs, which increases fluxes of ν_e and $\bar{\nu}_e$ in high energy region. These features of collective neutrino oscillations are consistent with previous studies and also common in more complex three flavor multiangle simulations. The mechanism of collective neutrino oscillations is still unclear because of the non-linear phenomena, but Refs. [58, 62, 63] suggest that the spectral swap of collective neutrino oscillations can be regarded as adiabatic level crossings like MSW resonances in a co-rotating frame in case of the single energy split as shown in the right panel of Fig.3.8. We confirm numerically that such adiabatic level crossing actually happens in a co-rotating frame.

In Chapter 4, we carry out three flavor multiangle calculations by using simulation data of an electron capture supernova and discuss how collective neutrino oscillations can be clarified in future neutrino obeservatories such as HK, JUNO and DUNE. The progenitor mass of the electron capture supernova is $8.8M_{\odot}$. The benefit of such light mass progenitor is successful shock revival even in 1D geometry without any artificial treatment, which helps precise initial neutrino spectra on the surface of neutrino sphere. Furthermore, the extreme dilute matter envelop of the progenitor is favorable for active collective neutrino oscillations because of the small multiangle matter

effect. The properties of collective neutrino oscillations as shown in Chapter 3 are roughly maintained in more realistic three flavor multiangle simulations but flavor conversions become unclear compared with the case in single angle calculation. The complete spectral swaps in a single angle calculation is smeared out in a multiangle simulation because angular dispersion of matter potential prevents the coherence of collective neutrino oscillations. In inverted mass hierarchy, collective neutrino oscillations take place mainly in $e-y$ sector and subsequent $e-x$ conversions happen. Before 200 ms post bounce, the $e-y$ conversions associated with $\omega_{\rm atm}$ becomes dominant and $e-x$ conversions are negligible. On the other hands, in the later phase of mass accretion >200 ms, three flavor mixing becomes prominent because of the small asymmetry among initial neutrino fluxes: $\Phi^0_{\nu_e} \sim \Phi^0_{\bar{\nu}_e} \sim \Phi^0_{\nu_x}$. In normal mass hierarchy, we find dominant $e-x$ conversions and subsequent $e-y$ mixing. Such significant $e-x$ conversions in normal mass hierarchy are not found in previous studies. Collective neutrino oscillations in normal mass hierarchy are easily suppressed in dense matter profile, so that such non-linear phenomenon in normal mass hierarchy would be peculiar to light mass progenitor such as electron capture supernovae. Neutrino flux on the earth is derived by an assumption of adibatic flavor conversions at MSW resonances. Especially, the H-resonance plays crucial role to soften hard neutrino spectra after collective neutrino oscillations. Finally, we calculate the evolution of hardness ratio $R_{\rm H/L}$ in HK, JUNO and DUNE. In inverted mass hierarchy, spectrum of $\bar{\nu}_e$ becomes soft owing to the contributions of both collective neutrino oscillations and the H-resonance, which results in a small value of hardness ratio. Such decreased hardness ratio is suitable to probe collective neutrino oscillations because the value of hardness ratio continues to increase if we ignore collective neutrino oscillations. HK can distinguish effects of collective neutrino oscillations through the detection of $\bar{\nu}_e$ within the 1σ statistical error if the source distance is less than 15 kpc. In normal mass hierarchy, the spectrum of ν_e becomes soft because of the hierarchy dependence of H-resonance, so that DUNE has the sensitivity to the softened hardness ratio of ν_e. The contribution of collective neutrino oscillations can be distinguished in DUNE if the supernova explosion occurs within 4 kpc. The reduction of hardness ratio of ν_e around 100 ms can be detected if the source distance is less than 10 kpc.

In Chapter 5, we study how collective neutrino oscillations enhance the νp-process nucleosynthesis inside neutrino driven winds. We employ time snapshots of profiles at 0.6 and 1.1 s post bounce in 1D explosion model of $40M_{\odot}$ progenitor. In the early wind model (0.6 s), the reverse shock can affect the production of p-nuclei, so that we employ two types of wind trajectories with and without the reverse shock as shown in Fig.5.14. We apply numerical results of three flavor multiangle simulations to nuclear network calculations inside neutrino driven winds assuming steady state outflows. In the later wind model (1.1 s), collective neutrino oscillations in normal mass hierarchy induce sharp flavor transitions in energetic electron antineutrinos around 280 km, which enhances the reaction rate $\lambda_{\bar{\nu}_e}$ in Eq.(5.16) and the following νp-process. Overproduction factor of p-nuclei Γ_i in normal mass hierarchy is raised up by $10-10^4$ times compared with that in no oscillation case. This implies the necessity of consideration of collective neutrino oscillations for precise network calculation of the νp-process nucleosynthesis inside neutrino driven winds. Conversely, collective neutrino oscillations occur actively in inverted mass hierarchy in the early wind model (0.6 s) irrespective of the reverse shock. Thus the abundances of p-nuclei are enhanced in inverted mass hierarchy regardless of the reverse shock. However, the reverse shock can increase the contribution of early wind model on the averaged overproduction factor of p-nuclei, which results in larger $\langle\Gamma_i\rangle$ in inverted mass hierarchy than those in no oscillation case in the range of $A = 84 - 108$. Therefore, the enhancement of p-nuclei caused by collective neutrino oscillations is found in both neutrino mass hierarchies owing to the contribution of the reverse shock. The values of overproduction factor of ^{92,94}Mo and ^{96,98}Ru are still ~ 10 in normal mass hierarchy even if we consider the same amount of ejected ^{56}Ni mass $\sim 0.07M_{\odot}$ as that of SN1987A. Furthermore, the contribution of Type II supernovae on the solar abundance of ^{56}Fe is comparable with that of Type Ia supernovae [265], which implies collective neutrino oscillations may contribute to solar abundances of ^{92,94}Mo and ^{96,98}Ru.

Bibliography

[1] R. Davis, Jr., D. S. Harmer, and K. C. Hoffman, Phys. Rev. Lett. **20**, 1205 (1968).

[2] SNO, S. N. Ahmed *et al.*, Phys. Rev. Lett. **92**, 181301 (2004).

[3] Super-Kamiokande, S. Fukuda *et al.*, Phys. Rev. Lett. **86**, 5656 (2001).

[4] Super-Kamiokande, K. Abe *et al.*, Phys. Rev. **D94**, 052010 (2016).

[5] BOREXINO, M. Agostini *et al.*, Nature **562**, 505 (2018).

[6] Super-Kamiokande, Y. Fukuda *et al.*, Phys. Rev. Lett. **81**, 1562 (1998).

[7] Super-Kamiokande, K. Abe *et al.*, Phys. Rev. **D97**, 072001 (2018).

[8] IceCube, M. G. Aartsen *et al.*, Phys. Rev. Lett. **120**, 071801 (2018).

[9] T. Araki *et al.*, Nature **436**, 499 (2005).

[10] Borexino, M. Agostini *et al.*, arXiv:1909.02257 .

[11] Kamiokande-II, K. Hirata *et al.*, Phys. Rev. Lett. **58**, 1490 (1987), [,727(1987)].

[12] R. M. Bionta *et al.*, Phys. Rev. Lett. **58**, 1494 (1987).

[13] E. N. Alekseev, L. N. Alekseeva, I. V. Krivosheina, and V. I. Volchenko, Phys. Lett. **B205**, 209 (1988).

[14] IceCube, Fermi-LAT, MAGIC, AGILE, ASAS-SN, HAWC, H.E.S.S., INTEGRAL, Kanata, Kiso, Kapteyn, Liverpool Telescope, Subaru, Swift NuSTAR, VERITAS, VLA/17B-403, M. G. Aartsen *et al.*, Science **361**, eaat1378 (2018).

[15] Double Chooz, Y. Abe *et al.*, Phys. Rev. Lett. **108**, 131801 (2012).

[16] Daya Bay, F. P. An *et al.*, Phys. Rev. Lett. **108**, 171803 (2012).

[17] RENO, J. K. Ahn *et al.*, Phys. Rev. Lett. **108**, 191802 (2012).

[18] T2K, K. Abe *et al.*, Phys. Rev. Lett. **107**, 041801 (2011).

[19] T2K, K. Abe *et al.*, Phys. Rev. Lett. **118**, 151801 (2017).

[20] NOvA, P. Adamson *et al.*, Phys. Rev. Lett. **118**, 231801 (2017).

[21] T. J. Loredo and D. Q. Lamb, Phys. Rev. **D65**, 063002 (2002).

[22] I. Goldman, Y. Aharonov, G. Alexander, and S. Nussinov, Phys. Rev. Lett. **60**, 1789 (1988).

[23] A. B. McDonald, C. Spiering, S. Schonert, E. T. Kearns, and T. Kajita, Rev. Sci. Instrum. **75**, 293 (2004).

[24] R. Diehl *et al.*, Nature **439**, 45 (2006).

[25] H. A. Bethe and J. R. Wilson, Astrophys. J. **295**, 14 (1985).

[26] H. A. Bethe, Rev. Mod. Phys. **62**, 801 (1990).

[27] J. F. Beacom and M. R. Vagins, Phys. Rev. Lett. **93**, 171101 (2004).

[28] Super-Kamiokande, M. Ikeda *et al.*, Astrophys. J. **669**, 519 (2007).

[29] KamLAND, K. Asakura *et al.*, Astrophys. J. **818**, 91 (2016).

[30] L. Cadonati, F. P. Calaprice, and M. C. Chen, Astropart. Phys. **16**, 361 (2002).

[31] LVD, N. Y. Agafonova *et al.*, Astrophys. J. **802**, 47 (2015).

[32] H. Wei, L. Lebanowski, F. Li, Z. Wang, and S. Chen, Astropart. Phys. **75**, 38 (2016).

[33] IceCube, R. Abbasi *et al.*, Astron. Astrophys. **535**, A109 (2011), [Erratum: Astron. Astrophys.563,C1(2014)].

[34] P. Antonioli *et al.*, New J. Phys. **6**, 114 (2004).

[35] K. Scholberg, Astron. Nachr. **329**, 337 (2008).

[36] Hyper-Kamiokande, K. Abe *et al.*, arXiv:1805.04163 .

[37] JUNO, F. An *et al.*, J. Phys. **G43**, 030401 (2016).

[38] K. Scholberg, Ann. Rev. Nucl. Part. Sci. **62**, 81 (2012).

[39] B. Pontecorvo, Sov. Phys. JETP **6**, 429 (1957), [Zh. Eksp. Teor. Fiz.33,549(1957)].

[40] B. Pontecorvo, Sov. Phys. JETP **7**, 172 (1958), [Zh. Eksp. Teor. Fiz.34,247(1957)].

[41] S. P. Mikheyev and A. Yu. Smirnov, Sov. J. Nucl. Phys. **42**, 913 (1985), [,305(1986)].

[42] L. Wolfenstein, Physical Review D **17**, 2369 (1978).

[43] J. T. Pantaleone, Phys. Rev. **D46**, 510 (1992).

[44] J. T. Pantaleone, Phys. Lett. **B287**, 128 (1992).

[45] G. Sigl and G. Raffelt, Nucl. Phys. **B406**, 423 (1993).

[46] B. H. J. McKellar and M. J. Thomson, Phys. Rev. **D49**, 2710 (1994).

[47] S. Yamada, Phys. Rev. **D62**, 093026 (2000).

[48] A. B. Balantekin and Y. Pehlivan, J. Phys. **G34**, 47 (2007).

[49] C. Y. Cardall, Phys. Rev. **D78**, 085017 (2008).

[50] V. Cirigliano, C. Lee, M. J. Ramsey-Musolf, and S. Tulin, Phys. Rev. **D81**, 103503 (2010).

[51] Y. Pehlivan, A. B. Balantekin, T. Kajino, and T. Yoshida, Phys. Rev. **D84**, 065008 (2011).

[52] A. Vlasenko, G. M. Fuller, and V. Cirigliano, Phys. Rev. **D89**, 105004 (2014).

[53] C. Volpe, D. Väänänen, and C. Espinoza, Phys. Rev. **D87**, 113010 (2013).

[54] D. N. Blaschke and V. Cirigliano, Phys. Rev. **D94**, 033009 (2016).

[55] S. Birol, Y. Pehlivan, A. B. Balantekin, and T. Kajino, Phys. Rev. **D98**, 083002 (2018).

[56] T. Yoshida *et al.*, Phys. Rev. Lett. **96**, 091101 (2006).

[57] H. Ko *et al.*, arXiv:1903.02086 .

[58] H. Duan, G. M. Fuller, J. Carlson, and Y.-Z. Qian, Phys. Rev. **D74**, 105014 (2006).

[59] H. Duan, G. M. Fuller, and Y.-Z. Qian, Phys. Rev. **D74**, 123004 (2006).

[60] S. Hannestad, G. G. Raffelt, G. Sigl, and Y. Y. Y. Wong, Phys. Rev. **D74**, 105010 (2006), [Erratum: Phys. Rev.D76,029901(2007)].

[61] G. L. Fogli, E. Lisi, A. Marrone, and A. Mirizzi, JCAP **0712**, 010 (2007).

[62] G. G. Raffelt and A. Yu. Smirnov, Phys. Rev. **D76**, 125008 (2007).

[63] G. G. Raffelt and A. Yu. Smirnov, Phys. Rev. **D76**, 081301 (2007), [Erratum: Phys. Rev.D77,029903(2008)].

[64] A. Esteban-Pretel, S. Pastor, R. Tomas, G. G. Raffelt, and G. Sigl, Phys. Rev. **D76**, 125018 (2007).

[65] A. Esteban-Pretel *et al.*, Phys. Rev. **D78**, 085012 (2008).

[66] B. Dasgupta and A. Dighe, Phys. Rev. **D77**, 113002 (2008).

[67] B. Dasgupta, A. Dighe, G. G. Raffelt, and A. Yu. Smirnov, Phys. Rev. Lett. **103**, 051105 (2009).

[68] J. F. Cherry, G. M. Fuller, J. Carlson, H. Duan, and Y.-Z. Qian, Phys. Rev. **D82**, 085025 (2010).

[69] J. F. Cherry *et al.*, Phys. Rev. **D84**, 105034 (2011).

[70] A. Friedland, Phys. Rev. Lett. **104**, 191102 (2010).

[71] B. Dasgupta, A. Mirizzi, I. Tamborra, and R. Tomas, Phys. Rev. **D81**, 093008 (2010).

[72] A. Mirizzi and R. Tomas, Phys. Rev. **D84**, 033013 (2011).

[73] H. Duan and A. Friedland, Phys. Rev. Lett. **106**, 091101 (2011).

[74] S. Chakraborty, T. Fischer, A. Mirizzi, N. Saviano, and R. Tomas, Phys. Rev. **D84**, 025002 (2011).

[75] J. F. Cherry, J. Carlson, A. Friedland, G. M. Fuller, and A. Vlasenko, Phys. Rev. Lett. **108**, 261104 (2012).

[76] A. de Gouvea and S. Shalgar, JCAP **1210**, 027 (2012).

[77] A. Mirizzi, Phys. Rev. **D88**, 073004 (2013).

[78] S. Chakraborty and A. Mirizzi, Phys. Rev. **D90**, 033004 (2014).

[79] S. Chakraborty, A. Mirizzi, N. Saviano, and D. d. S. Seixas, Phys. Rev. **D89**, 093001 (2014).

[80] M.-R. Wu, Y.-Z. Qian, G. Martinez-Pinedo, T. Fischer, and L. Huther, Phys. Rev. **D91**, 065016 (2015).

[81] J. Y. Tian, A. V. Patwardhan, and G. M. Fuller, Phys. Rev. **D95**, 063004 (2017).

[82] H. Sasaki *et al.*, Phys. Rev. **D96**, 043013 (2017).

[83] M. Zaizen, T. Yoshida, K. Sumiyoshi, and H. Umeda, Phys. Rev. **D98**, 103020 (2018).

[84] H. Sasaki, T. Takiwaki, S. Kawagoe, S. Horiuchi, and K. Ishidoshiro, arXiv:1907.01002 .

[85] S. Shibagaki *et al.*, Astrophys. J. **816**, 79 (2016).

[86] C. Frohlich *et al.*, Phys. Rev. Lett. **96**, 142502 (2006).

[87] J. Pruet, R. D. Hoffman, S. E. Woosley, H. T. Janka, and R. Buras, Astrophys. J. **644**, 1028 (2006).

[88] S. Wanajo, Astrophys. J. **647**, 1323 (2006).

[89] M. Fukugita and T. Yanagida, *Physics of neutrinos and applications to astrophysics* (Berlin, Germany: Springer (2003) 593 p, 2003).

[90] C. Giunti and C. W. Kim, *Fundamentals of Neutrino Physics and Astrophysics* (Oxford, UK: Univ. Pr. (2007) 710 p, 2007).

[91] Planck, P. A. R. Ade *et al.*, Astron. Astrophys. **594**, A13 (2016).

[92] Particle Data Group, M. Tanabashi *et al.*, Phys. Rev. **D98**, 030001 (2018), and 2019 update.

[93] Z. Maki, M. Nakagawa, and S. Sakata, Prog. Theor. Phys. **28**, 870 (1962), [,34(1962)].

[94] S.-B. Kim, Nucl. Part. Phys. Proc. **265-266**, 93 (2015).

[95] ICAL, S. Ahmed *et al.*, Pramana **88**, 79 (2017).

[96] KM3NeT, U. F. Katz, The ORCA Option for KM3NeT, in *Proceedings of the 15th International Workshop on Neutrino Telescopes (Neutel 2013): Venice, March 11-15, 2013*, 2014.

[97] IceCube PINGU, M. G. Aartsen *et al.*, arXiv:1401.2046 .

[98] H. P. Breuer and F. Petruccione, *The theory of open quantum systems* (Oxford, UK: Univ. Pr. (2002) 625 p, 2002).

[99] L. D. Landau, Phys. Zs. Sowjet **2**, 46 (1932).

[100] C. Zener, Proceedings of the Royal Society of London Series A **137**, 696 (1932).

[101] J. R. Rubbmark, M. M. Kash, M. G. Littman, and D. Kleppner, Phys. Rev. A **23**, 3107 (1981).

[102] M. Born and V. Fock, Zeitschrift fur Physik **51**, 165 (1928).

[103] T. Kato, Journal of the Physical Society of Japan **5**, 435 (1950).

[104] Y. Pehlivan, A. L. Subaşı, N. Ghazanfari, S. Birol, and H. Yüksel, Phys. Rev. **D95**, 063022 (2017).

[105] M. Born and H. S. Green, Proc. Roy. Soc. Lond. **A188**, 10 (1946).

[106] J. Yvon, Act. Sci. et Ind. **203** (1935).

[107] J. Yvon, Chem.Phys. **3** (1935).

[108] N. Bogoliubov, Journal of Physics USSR **10** (1946).

[109] A. D. Dolgov *et al.*, Nucl. Phys. **B632**, 363 (2002).

[110] P. F. de Salas and S. Pastor, JCAP **1607**, 051 (2016).

[111] L. Johns, M. Mina, V. Cirigliano, M. W. Paris, and G. M. Fuller, Phys. Rev. **D94**, 083505 (2016).

[112] T. Hasegawa *et al.*, arXiv:1908.10189 .

[113] Y.-L. Zhu, A. Perego, and G. C. McLaughlin, Phys. Rev. **D94**, 105006 (2016).

[114] M. Frensel, M.-R. Wu, C. Volpe, and A. Perego, Phys. Rev. **D95**, 023011 (2017).

[115] A. Chatelain and C. Volpe, Phys. Rev. **D95**, 043005 (2017).

[116] L. Becerra *et al.*, Astrophys. J. **852**, 120 (2018).

[117] N. Langer, Annual Review of Astronomy and Astrophysics **50**, 107 (2012).

[118] K. Nomoto, Astrophys. J. **277**, 791 (1984).

[119] K. Nomoto, Astrophys. J. **322**, 206 (1987).

[120] F. S. Kitaura, H. T. Janka, and W. Hillebrandt, Astron. Astrophys. **450**, 345 (2006).

[121] H.-T. Janka *et al.*, Progress of Theoretical and Experimental Physics **2012**, 01A309 (2012).

[122] C. L. Doherty, P. Gil-Pons, L. Siess, J. C. Lattanzio, and H. H. B. Lau, Monthly Notices of the Royal Astronomical Society **446**, 2599 (2014).

[123] T. J. Moriya and J. J. Eldridge, Monthly Notices of the Royal Astronomical Society **461**, 2155 (2016).

[124] K. Takahashi, T. Yoshida, and H. Umeda, Astrophys. J. **771**, 28 (2013).

[125] M. Turatto *et al.*, Astrophys. J. Letters **498**, L129 (1998).

[126] A. Pastorello *et al.*, Monthly Notices of the Royal Astronomical Society **394**, 2266 (2009).

[127] M. T. Botticella *et al.*, Monthly Notices of the Royal Astronomical Society **398**, 1041 (2009).

[128] K. Nomoto *et al.*, Nature **299**, 803 (1982).

[129] N. Tominaga, S. I. Blinnikov, and K. Nomoto, Astrophys. J. **771**, L12 (2013).

[130] S. Wanajo, H.-T. Janka, and B. Mueller, Astrophys. J. **726**, L15 (2011).

[131] A. Heger, C. L. Fryer, S. E. Woosley, N. Langer, and D. H. Hartmann, Astrophys. J. **591**, 288 (2003).

[132] S. E. Woosley, A. Heger, and T. A. Weaver, Rev. Mod. Phys. **74**, 1015 (2002).

[133] A. Gal-Yam *et al.*, Nature **462**, 624 (2009).

[134] E. O. Ofek *et al.*, Astrophys. J. Letters **659**, L13 (2007).

[135] N. Smith *et al.*, Astrophys. J. **666**, 1116 (2007).

[136] A. Kozyreva, M. Kromer, U. M. Noebauer, and R. Hirschi, Mon. Not. Roy. Astron. Soc. **479**, 3106 (2018).

[137] N. Langer *et al.*, Astron. Astrophys. **475**, L19 (2007).

[138] H. Suzuki, In *Fukugita, M. (ed.), Suzuki, A. (ed.): Physics and astrophysics of neutrinos* 763-847 , 763 (1994).

[139] A. Mezzacappa and S. W. Bruenn, Astrophys. J. **405**, 637 (1993).

[140] K. Sumiyoshi *et al.*, Astrophys. J. **629**, 922 (2005).

[141] K. Sumiyoshi, H. Suzuki, S. Yamada, and H. Toki, Nucl. Phys. **A730**, 227 (2004).

[142] S. A. Colgate, W. H. Grasberger, and R. H. White, Astronomical Journal **70**, 280 (1961).

[143] Y. Z. Qian and S. E. Woosley, Astrophys. J. **471**, 331 (1996).

[144] H. T. Janka, Astron. Astrophys. (2000), [Astron. Astrophys.368,527(2001)].

[145] E. O'Connor *et al.*, J. Phys. **G45**, 104001 (2018).

[146] J. M. Blondin, A. Mezzacappa, and C. DeMarino, Astrophys. J. **584**, 971 (2003).

[147] T. Takiwaki, K. Kotake, and Y. Suwa, Astrophys. J. **749**, 98 (2012).

[148] F. Hanke, B. Müller, A. Wongwathanarat, A. Marek, and H.-T. Janka, Astrophys. J. **770**, 66 (2013).

[149] F. Hanke, A. Marek, B. Müller, and H.-T. Janka, Astrophys. J. **755**, 138 (2012).

[150] T. Takiwaki, K. Kotake, and Y. Suwa, Astrophys. J. **786**, 83 (2014).

[151] T. Takiwaki, K. Kotake, and Y. Suwa, Mon. Not. Roy. Astron. Soc. **461**, L112 (2016).

[152] T. Takiwaki, K. Kotake, and K. Sato, Astrophys. J. **691**, 1360 (2009).

[153] P. Mösta *et al.*, Astrophys. J. **785**, L29 (2014).

[154] K. Langanke *et al.*, Phys. Rev. Lett. **90**, 241102 (2003).

[155] K. Nakazato *et al.*, Astrophys. J. Suppl. **205**, 2 (2013).

[156] T. A. Thompson, A. Burrows, and P. A. Pinto, Astrophys. J. **592**, 434 (2003).

[157] F. Capozzi, B. Dasgupta, A. Mirizzi, M. Sen, and G. Sigl, Phys. Rev. Lett. **122**, 091101 (2019).

[158] T. Stirner, G. Sigl, and G. Raffelt, JCAP **1805**, 016 (2018).

[159] V. Cirigliano, M. Paris, and S. Shalgar, JCAP **1811**, 019 (2018).

[160] S. Shalgar and I. Tamborra, arXiv:1904.07236 .

[161] M. Zaizen *et al.*, arXiv:1908.10594 .

[162] C. J. Stapleford, C. Fröhlich, and J. P. Kneller, arXiv:1910.04172 .

[163] R. F. Sawyer, Phys. Rev. **D79**, 105003 (2009).

[164] G. Raffelt, S. Sarikas, and D. de Sousa Seixas, Phys. Rev. Lett. **111**, 091101 (2013), [Erratum: Phys. Rev. Lett.113,no.23,239903(2014)].

[165] R. F. Sawyer, Phys. Rev. Lett. **116**, 081101 (2016).

[166] B. Dasgupta, A. Mirizzi, and M. Sen, JCAP **1702**, 019 (2017).

[167] F. Capozzi, B. Dasgupta, E. Lisi, A. Marrone, and A. Mirizzi, Phys. Rev. **D96**, 043016 (2017).

[168] I. Izaguirre, G. Raffelt, and I. Tamborra, Phys. Rev. Lett. **118**, 021101 (2017).

[169] S. Chakraborty, R. S. Hansen, I. Izaguirre, and G. Raffelt, JCAP **1603**, 042 (2016).

[170] S. Abbar and H. Duan, Phys. Rev. **D98**, 043014 (2018).

[171] S. Abbar, H. Duan, K. Sumiyoshi, T. Takiwaki, and M. C. Volpe, Phys. Rev. **D100**, 043004 (2019).

[172] T. Morinaga and S. Yamada, Phys. Rev. **D97**, 023024 (2018).

[173] M. Delfan Azari *et al.*, Phys. Rev. **D99**, 103011 (2019).

[174] S. Abbar, H. Duan, K. Sumiyoshi, T. Takiwaki, and M. C. Volpe, arXiv:1911.01983 .

[175] T. Morinaga, H. Nagakura, C. Kato, and S. Yamada, arXiv:1909.13131 .

[176] H. Nagakura, T. Morinaga, C. Kato, and S. Yamada, arXiv:1910.04288 .

[177] M. Delfan Azari *et al.*, arXiv:1910.06176 .

[178] R. Glas *et al.*, arXiv:1912.00274 .

[179] C. J. Stapleford, D. J. Väänänen, J. P. Kneller, G. C. McLaughlin, and B. T. Shapiro, Phys. Rev. **D94**, 093007 (2016).

[180] A. Dighe and M. Sen, Phys. Rev. **D97**, 043011 (2018).

[181] Y. Yang and J. P. Kneller, Phys. Rev. **D97**, 103018 (2018).

[182] C. Lunardini, B. Muller, and H. T. Janka, Phys. Rev. **D78**, 023016 (2008).

[183] R. Tomas *et al.*, JCAP **0409**, 015 (2004).

[184] G. L. Fogli, E. Lisi, A. Mirizzi, and D. Montanino, JCAP **0504**, 002 (2005).

[185] S. Kawagoe *et al.*, Phys. Rev. **D81**, 123014 (2010).

[186] K. Nakamura *et al.*, Mon. Not. Roy. Astron. Soc. **461**, 3296 (2016).

[187] C. Kato *et al.*, Astrophys. J. **848**, 48 (2017).

[188] Super-Kamiokande, C. Simpson *et al.*, Astrophys. J. **885**, 133 (2019).

[189] H. Duan, G. M. Fuller, and Y.-Z. Qian, Ann. Rev. Nucl. Part. Sci. **60**, 569 (2010).

[190] F. Bloch, Phys. Rev. **70**, 460 (1946).

[191] R. P. Feynman, F. L. Vernon, Jr., and R. W. Hellwarth, J. Appl. Phys. **28**, 49 (1957).

[192] N. Vitanov, T. Halfmann, B. Shore, and K. Bergmann, Annual review of physical chemistry **52**, 763 (2001).

[193] K. Kotake, T. Takiwaki, T. Fischer, K. Nakamura, and G. Martínez-Pinedo, Astrophys. J. **853**, 170 (2018).

[194] H. Sotani and T. Takiwaki, Phys. Rev. **D94**, 044043 (2016).

[195] K. Nakamura, T. Takiwaki, T. Kuroda, and K. Kotake, Publ. Astron. Soc. Jap. **67**, 107 (2015).

[196] J. M. Lattimer and F. D. Swesty, Nucl. Phys. **A535**, 331 (1991).

[197] A. Summa *et al.*, Astrophys. J. **825**, 6 (2016).

[198] T. Yoshida, Y. Suwa, H. Umeda, M. Shibata, and K. Takahashi, Mon. Not. Roy. Astron. Soc. **471**, 4275 (2017).

[199] H. T. Janka, B. Mueller, F. S. Kitaura, and R. Buras, Astron. Astrophys. **485**, 199 (2008).

[200] T. Fischer, S. C. Whitehouse, A. Mezzacappa, F. K. Thielemann, and M. Liebendorfer, Astron. Astrophys. **517**, A80 (2010).

[201] C. J. Horowitz, Phys. Rev. **D65**, 043001 (2002).

[202] C. J. Horowitz, O. L. Caballero, Z. Lin, E. O'Connor, and A. Schwenk, Phys. Rev. **C95**, 025801 (2017).

[203] I. Tamborra, G. Raffelt, F. Hanke, H.-T. Janka, and B. Mueller, Phys. Rev. **D90**, 045032 (2014).

[204] I. Tamborra, B. Muller, L. Hudepohl, H.-T. Janka, and G. Raffelt, Phys. Rev. **D86**, 125031 (2012).

[205] M. T. Keil, G. G. Raffelt, and H.-T. Janka, Astrophys. J. **590**, 971 (2003).

[206] A. B. Balantekin and G. M. Fuller, Phys. Lett. **B471**, 195 (1999).

[207] C. Döring, R. S. L. Hansen, and M. Lindner, JCAP **1908**, 003 (2019).

[208] E. Borriello, S. Chakraborty, A. Mirizzi, P. D. Serpico, and I. Tamborra, Phys. Rev. **D86**, 083004 (2012).

[209] P. Vogel and J. F. Beacom, Phys. Rev. **D60**, 053003 (1999).

[210] E. O'Connor and C. D. Ott, Astrophys. J. **762**, 126 (2013).

[211] S. Horiuchi, K. Nakamura, T. Takiwaki, and K. Kotake, J. Phys. **G44**, 114001 (2017).

[212] S. Kawagoe, T. Takiwaki, and K. Kotake, JCAP **0909**, 033 (2009).

[213] KamLAND, A. Gando *et al.*, Astrophys. J. **829**, L34 (2016), [Erratum: Astrophys. J.851,no.1,L22(2017)].

[214] E. Kolbe, K. Langanke, G. Martínez-Pinedo, and P. Vogel, Journal of Physics G Nuclear Physics **29**, 2569 (2003).

[215] A. Ankowski *et al.*, Supernova Physics at DUNE, in *Supernova Physics at DUNE Blacksburg, Virginia, USA, March 11-12, 2016*, 2016.

[216] G. Martinez-Pinedo, B. Ziebarth, T. Fischer, and K. Langanke, Eur. Phys. J. **A47**, 98 (2011).

[217] S. E. Woosley and T. A. Weaver, Astrophys. J. Suppl. **101**, 181 (1995).

[218] K. Nomoto, C. Kobayashi, and N. Tominaga, Ann. Rev. Astron. Astrophys. **51**, 457 (2013).

[219] N. Tominaga, H. Umeda, and K. Nomoto, Astrophys. J. **660**, 516 (2007).

[220] W. D. Arnett, J. N. Bahcall, R. P. Kirshner, and S. E. Woosley, Ann. Rev. Astron. Astrophys. **27**, 629 (1989).

[221] H. Umeda and K. Nomoto, Astrophys. J. **565**, 385 (2002).

[222] K. Nomoto *et al.*, Nuovo Cim. **B121**, 1207 (2006).

[223] E. Pllumbi, I. Tamborra, S. Wanajo, H.-T. Janka, and L. Hüdepohl, Astrophys. J. **808**, 188 (2015).

[224] S. E. Woosley and R. D. Hoffman, Astrophys. J. **395**, 202 (1992).

[225] S. E. Woosley, J. R. Wilson, G. J. Mathews, R. D. Hoffman, and B. S. Meyer, Astrophys. J. **433**, 229 (1994).

[226] K. Otsuki, H. Tagoshi, T. Kajino, and S.-y. Wanajo, Astrophys. J. **533**, 424 (2000).

[227] R. D. Hoffman, S. E. Woosley, and Y. Z. Qian, Astrophys. J. **482**, 951 (1997).

[228] S. Wanajo, Astrophys. J. **770**, L22 (2013).

[229] L. Hudepohl, B. Muller, H. T. Janka, A. Marek, and G. G. Raffelt, Phys. Rev. Lett. **104**, 251101 (2010), [Erratum: Phys. Rev. Lett.105,249901(2010)].

[230] B. Muller, H.-T. Janka, and A. Marek, Astrophys. J. **756**, 84 (2012).

[231] A. Mirizzi *et al.*, Riv. Nuovo Cim. **39**, 1 (2016).

[232] N. Nishimura, T. Takiwaki, and F. K. Thielemann, Astrophys. J. **810**, 109 (2015).

[233] S. Wanajo *et al.*, Astrophys. J. **789**, L39 (2014).

[234] LIGO Scientific, Virgo, B. P. Abbott *et al.*, Phys. Rev. Lett. **119**, 161101 (2017).

[235] S. J. Smartt *et al.*, Nature **551**, 75 (2017).

[236] J-GEM, Y. Utsumi *et al.*, Publ. Astron. Soc. Jap. **69**, 101 (2017).

[237] M. Tanaka, Adv. Astron. **2016**, 6341974 (2016).

[238] M. Tanaka *et al.*, Publ. Astron. Soc. Jap. **69**, Publications of the Astronomical Society of Japan, Volume 69, Issue 6, 1 December 2017, 102, https://doi.org/10.1093/pasj/psx121 (2017).

[239] D. L. Lambert, The Astronomy and Astrophysics Review **3**, 201 (1992).

[240] B. S. Meyer, Ann. Rev. Astron. Astrophys. **32**, 153 (1994).

[241] S. E. Woosley and W. M. Howard, Astrophys. J. Supplement **36**, 285 (1978).

[242] W. M. Howard, B. S. Meyer, and S. E. Woosley, Astrophys. J. Letters **373**, L5 (1991).

[243] N. Prantzos, M. Hashimoto, M. Rayet, and M. Arnould, Astron. Astrophys. **238**, 455 (1990).

[244] M. Rayet, M. Arnould, M. Hashimoto, N. Prantzos, and K. Nomoto, Astron. Astrophys. **298**, 517 (1995).

[245] T. Rauscher, A. Heger, R. D. Hoffman, and S. E. Woosley, Astrophys. J. **576**, 323 (2002).

[246] T. Hayakawa *et al.*, Astrophys. J. **685**, 1089 (2008).

[247] S. Wanajo, H.-T. Janka, and S. Kubono, Astrophys. J. **729**, 46 (2011).

[248] A. Arcones, C. Frohlich, and G. Martinez-Pinedo, Astrophys. J. **750**, 18 (2012).

[249] J. Bliss, A. Arcones, and Y.-Z. Qian, Astrophys. J. **866**, 105 (2018).

[250] N. Nishimura *et al.*, Mon. Not. Roy. Astron. Soc. **489**, 1379 (2019).

[251] A. B. Balantekin and H. Yuksel, New J. Phys. **7**, 51 (2005).

[252] H. Duan, A. Friedland, G. McLaughlin, and R. Surman, J. Phys. **G38**, 035201 (2011).

[253] I. Tamborra, G. G. Raffelt, L. Hudepohl, and H.-T. Janka, JCAP **1201**, 013 (2012).

[254] A. Marek, H. Dimmelmeier, H. T. Janka, E. Muller, and R. Buras, Astron. Astrophys. **445**, 273 (2006).

[255] L. Hudepohl, Ph.D. thesis, Technische Universitat Munchen (2013).

[256] S. Fujibayashi, T. Yoshida, and Y. Sekiguchi, Astrophys. J. **810**, 115 (2015).

[257] M. Terasawa, T. Kajino, K. Langanke, G. J. Mathews, and E. Kolbe, Astrophys. J. **608**, 470 (2004).

[258] T. Yoshida *et al.*, Astrophys. J. **686**, 448 (2008).

[259] E. K. Warburton and B. A. Brown, Phys. Rev. **C46**, 923 (1992).

[260] R. H. Cyburt *et al.*, Astrophys. J. Supplement **189**, 240 (2010).

[261] B. Meyer and D. C. Adams, Meteoritics Planet. Sci. Suppl. **42**, 5215 (2007).

[262] B. S. Meyer, T. D. Krishnan, and D. D. Clayton, Astrophys. J. **498**, 808 (1998).

[263] K. Lodders, Astrophys. J. **591**, 1220 (2003).

[264] A. Burrows, D. Vartanyan, J. C. Dolence, M. A. Skinner, and D. Radice, Space Sci. Rev. **214**, 33 (2018).

[265] M. Kusakabe, N. Iwamoto, and K. Nomoto, Astrophys. J. **726**, 25 (2011).